OBSERVATIONS OF LABORATORY RIP CURRENTS

A Thesis
Presented to
The Academic Faculty

by

Brian K. Sapp

In Partial Fulfillment
of the Requirements for the Degree
Master of Science in Civil Engineering

School of Civil and Environmental Engineering
Georgia Institute of Technology
May 2006

OBSERVATIONS OF LABORATORY RIP CURRENTS

Approved by:

Dr. Kevin Haas, Advisor
School of Civil and Environmental Engineering
Georgia Institute of Technology

Dr. Paul Work
School of Civil and Environmental Engineering
Georgia Institute of Technology

Dr. Hermann Fritz
School of Civil and Environmental Engineering
Georgia Institute of Technology

Dr. Donald Webster
School of Civil and Environmental Engineering
Georgia Institute of Technology

Date Approved: December 21, 2005

ACKNOWLEDGEMENTS

I would like to express my gratitude to all those who gave me the possibility to complete this thesis. This work was sponsored by the National Oceanographic Partnership Program (NOPP) under grant N00014-99-1-1051. NOPP, established by United States Congress in 1997, consists of fifteen agencies to provide leadership and coordination for oceanographic research. Additional funding was provided by the U.S. National Geospatial-Intelligence Agency. I wish to thank Dr. Kevin Haas for this research opportunity and guiding me through. Also, the assistance of Dr. Andrew Kennedy on this research is greatly acknowledged. I would like to thank the committee members: Dr. Paul Work, Dr. Hermann Fritz, and Dr. Donald Webster for their time and comments on this research.

I wish to thank my wife, Gloria, and family, whose love, patience, and support enabled me to complete this work. To the best officemates in the world, Kemâl and Zafer, thanks for bringing laughter into the office to lighten those stressful moments. I wish to thank Dr. Stan Lindsey for the continuous encouragement and the teaching assistantship opportunity. Lastly, I want to thank everyone involved with establishing and operating the Savannah campus of Georgia Tech; it has been a dream come true to be a student here.

TABLE OF CONTENTS

LIST OF TABLES

Page

LIST OF FIGURES

Page

SUMMARY

Laboratory experiments of rip current systems are performed in a wave basin with a bar and rip channel geometry at the Ocean Engineering Laboratory at the University of Delaware. The experiments include both in situ water level and velocity measurements and optical visualization of the flow field under a variety of normal-incident wave conditions. Digital video is used to record surface drifters moving through a rip current system. A method is presented that tracks these digitally-recorded drifters into long Lagrangian sequences. The laboratory measurements capture both an Eulerian and Lagrangian description of the rip current system.

Time-averaged rip current properties are calculated and analyzed using both in situ and video measurements. From the video, Lagrangian velocities are computed with forward differencing of the low-pass filtered drifter tracks. Wave properties are also estimated using the orbital drifter motions and linear (Airy) wave theory. The effects of various wave conditions on the time-averaged rip current systems are investigated to show that wave height is a critical parameter. Measurements of circulation cells are obtained by spatially averaging the drifter track velocity measurements into a polar grid ranging from 0.25 m to 3.25 m from the center of the cell. Circulation cell features, such as the center of circulation and cell width, are calculated to characterize their response to various wave conditions.

Spectral analyses are used to characterize the rip current pulsations in the experimental measurements. Three frequencies are found to be energetic in several of the experiments in the low frequency band: the wave group frequency, a lower frequency,

and the interaction of the wave group and lower frequencies. Some experiments have significant energy at each of the three peaks, where others have only one or none. The lower frequency motions have also been found in the video measurements and attributed to rip meandering. Possible causes for the low-frequency pulsations, including wave basin seiching, circulation cell instabilities, and wave-current interaction, are discussed.

This thesis adds to previous rip current studies by providing a spatially-large and time-varying perspective of rip current systems as a whole. The analysis contributes a better understanding of the effect of various wave conditions on the mean properties of rip current systems along with documenting and characterizing low-frequency pulsations evident in the experimental measurements.

CHAPTER 1

INTRODUCTION

The nearshore ocean attracts many visits from beachgoers along coasts all over the world. The relaxing, enjoyable, and natural environment makes coastal areas a premium and popular destination. The dangers, however, from the wave and currents are sometimes underestimated by waders and swimmers. From a 10-year survey by the United States Lifesaving Association, rip currents rank second to heat as the cause of weather-related fatalities. Many rip current survivors note the rapid development of strong currents; these rip pulsations can catch swimmers off-guard. A better understanding of nearshore rip system dynamics, such as rip current pulsations, is vital to increasing public safety in coastal-related activities.

Since coastal regions are among the most developed areas in the world, shoreline erosion is a critical and well-monitored process. Nearshore currents, including rip currents, are important contributors to sediment transport on beaches. Offshore-directed flows are responsible for the seaward deposition of sediment from the shoreline. Rip current studies can help better understand the movement of sediments in nearshore regions. The strength and offshore direction of a rip current, which have been observed to vary for different incident wave conditions, can affect the rate and location of sediment dispersals. Knowledge of the influence of incident wave conditions on rip current behavior will provide a means for better sediment transport predictions.

A better understanding of rip current behavior and pulsations is necessary for public safety and beach erosion. This study uses laboratory experiments with in situ and

video-based measurement techniques to extend the base of knowledge of rip current dynamics.

1.1 Literature Review

Rip current studies have been documented since the 1930's and cover a breadth of topics using a range of investigative methods. Field observations of rip currents historically provide qualitative descriptions of the flow behavior since accurate measurements of this migrant and unsteady flow system are difficult to achieve. Some field studies, however, have been successful at limited quantitative descriptions of rip current systems. Therefore, comprehensive quantitative analyses typically involve laboratory experiments, where the controlled setting is conducive for extensive measurements. Theoretical studies are imperative for a physical understanding of the observations and measurements. Field observations, laboratory experiments, and theoretical modeling collectively help with the understanding of the physics which can provide a framework for educating the public, lifeguards, and government organizations about rip currents.

1.1.1 Defining Rip Currents

Rip currents first gained recognition in a debate on whether cross-shore flow, namely undertow, existed in the surfzone. The popular belief was that this sub-surface current, undertow, balanced the shoreward-transport of water carried by the waves. Davis (1925a) was skeptical of this belief and called for readers that had observed this undertow to respond. Craig et al. (1925) replied to the discussion giving personal accounts of strong offshore-directed currents. Davis (1925b) responded to the accounts

and noted that the observations were of localized return flow and not necessarily undertow. Shepard (1936) provided some resolve to the discussion by distinguishing narrow, seaward-directed surface flows as being different from the subsurface return – undertow. Recommendations by Shepard explained that the term "rip current" would be more descriptive and fitting for these narrow flows than the previously-used term "rip tide". Shepard also stated that rip currents were the mechanism responsible for balancing the shoreward wave-transport of water, not undertow.

The first comprehensive description of a rip current system was made by Shepard et al. (1941) from their observations along the coast of southern California. They define rip currents as thin, seaward flows of water starting near the shore and extending beyond the breaker zone. Shepard et al. further classified nearshore circulation using three distinct features: the feeder currents, rip neck, and rip head as seen in Figure 1.1. Longshore variability in the wave field creates longshore pressure gradients that drive the feeder currents toward the rip channel from both sides. These feeder currents converge and cause an increase in water level in the rip channel. The water surface slope from this water level increase creates a cross-shore pressure gradient that supplies the flow through the narrow rip neck. Arthur (1962) performed an early theoretical investigation of rip currents by applying the vorticity equation to the flow of a rip current. From his analysis, he noted that the width of the rip current decreases as the depth increases due to vortex stretching. Seaward of the breaker zone, the flow expands in the rip head as a surface current.

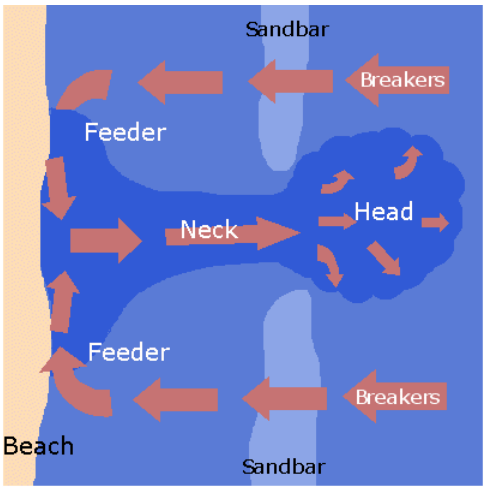

Figure 1.1: Rip current schematic (National Weather Service)

1.1.2 Generation Mechanisms

Several mechanisms for rip current formation have been noted from both field and theoretical studies. Dalrymple (1979) broadly classified rip generation theories into two categories: wave interaction models and structural interaction models. Wave interaction models include incident-edge waves, intersecting wave trains, and wave-current interaction. Structural interaction mechanisms include bottom topography, coastal boundaries, and barred coastlines. Recently a third mechanism category, vorticity generation models, has been introduced.

One of the most common mechanisms for rip current generation was first observed by Shepard et al. (1941) consisting of longshore sandbars with rip channel cuts, as shown in Figure 1.1. This mechanism has been the focus of many rip current studies to date (such as Haller et al. (1997a), Haas and Svendsen (2002), Yu and Slinn (2003), and MacMahan et al. (2004a) to name a few).

Bowen (1969) further hypothesized that longshore variation in wave breaking could cause nearshore circulation cells. A wave-induced nearshore circulation model by

Noda (1974) supported the hypothesis of Bowen that the interaction of incident waves and local bottom topography could produce circulation cells.

The formation of rip currents on a planar beach was investigated using a hydrodynamic instability approach by Hino (1974). He conjectured that rip currents and the channels may form as one unit. The longshore spacing between these rip channels have been theoretically related to eigen-wavenumbers (Iwata 1976, Mizuguchi 1976, Miller and Barcilon 1978). Iwata found that this rip spacing is related to the beach slope. Miller and Barcilon also noted that the spacing was dependent on the rate of wave dissipation and the bottom friction factor. Deiggard (1990) used a stability analysis to investigate the formation of rip channels on a barred beach. He found that the rip spacing was on the same order as the distance from the shoreline to the bars.

Wave interactions have also been shown to produce spatially varying wave heights that induce rip currents (Huntley et al. 1988). Dalrymple (1975) proposed a mechanism for generating periodic longshore variations using intersecting wave trains. A small-amplitude bifurcation analysis also revealed that rip current cells could be formed from wave-current interaction (Dalrymple and Lozano 1978). Theoretical studies by Falqués et al. (1999) found that rip currents on non-barred beaches cannot be explained simply by instabilities originating from wave setup/setdown. They demonstrated that refraction of incident waves by the currents must be included for horizontal circulation to form due to hydrodynamic instabilities.

Rips have also been observed to form from longshore currents being diverted by structural interactions such as bathymetrical protrusions or man-made coastal structures (Shepard et al. 1941, Shepard and Inman 1951, Deguchi and Araki 2004).

Vorticity generation by differential wave breaking has been shown to form large-scale horizontal eddies (Peregrine 1998, Peregrine and Bokhove 1998, Peregrine 1999). Boussinesq modeling by Chen et al. (1999) of a topographically-controlled rip current system predicted vortex shedding on the bar edges. Bühler and Jacobson (2001) performed a detailed numerical study on vortex generation from wave breaking on longshore-uniform topographies. They also proposed a new mechanism that explains current dislocation on barred beaches. The behavior of breaking-wave-generated macrovortices was found to be mainly dependent on geometry (Brocchini et al. 2003). Their model predicted detachment periods of the vortices for detached breakwaters at wave startup and allowed investigation into vortex propagation. Kennedy (2003) analyzed wave-driven rip currents with a circulation-vorticity point of view. His model predicts rip current startup and effects of wave groupiness on the rip current neck.

1.1.3 Rip System Properties

Several scientists have investigated the effect of varying wave conditions on rip behavior. Shepard et al. (1941) was the first to note the strong correlation between wave heights and rip strength. Wave conditions not only affect the rip strength but have been observed to influence the density and spacing of rip currents (McKenzie 1958, Huntley and Short 1992). Furthermore, increased rip current activity has been linked with longer period wave conditions (Shepard and Inman 1950, Cook 1970, Lascody 1998). The angle of incidence also has been noted to be an important factor for rip current occurrences (Shepard and Inman 1950, Dette et al. 1995, Engle et al. 2002). Short and Brander (1999) investigated five different wave environments and concluded that fetch-limited waves with moderate winds produced the most rips. Nielson et al. (2001) related

the power in the rip system to the incoming wave power by describing the system as a wave pump. Collectively it has been found that rip currents are most likely to occur with high, long period, normal-incident waves with light to moderate winds. Using this knowledge, scientists including Chandramohan et al. (1997) have monitored wave conditions to determine locations for probable rip current events.

Other factors have been observed to influence the behavior of rip currents. Several scientists have noted the tidal modulation of rips (Shepard et al. 1941, Lushine 1991, Aagaard et al. 1997, Brander 1999, Engle et al. 2002, Haas et al. 2002). Haas et al. noted from their observations on Moreton Island, Australia that the change in wave breaking location from the ebbing tide caused the rip strengthening. The degree of wave energy dissipation has also been noted to affect rip current activity (Aagaard et al. 1997). Spatially, however, the position of the rip has been related to the point of wave convergence and divergence (Shepard and Inman 1950). The spacing between offshore rips has also been related to the interaction of edge waves and incident waves on flat beaches (Bowen and Inman 1969). Bowman et al. (1988a) observed that the flow velocity and directional asymmetry increased towards the neck and gradually decreased offshore. Fedderson and Guza (2003) noted non-uniform circulations near the shoreline but longshore uniform circulations away from the shore. Geometrical factors also influence rip behavior; Brander (1999a) documented that decreasing the rip channel cross-section dimensions increases the rip flow. Bubble content in a rip has also recently been used to characterize spatial and acoustic attenuation features of the rip current system (Caruthers et al. 1999, Vagle et al. 2001).

Sørensen et al. (1998) used a Boussinesq type model to simulate wave-induced horizontal nearshore circulation. Wave-current interaction has been modeled by Murray and Reydellet (2001) and Yu and Slinn (2003) to note the effect on rip currents.

The three-dimensional structure of rip currents was first modeled by De Vriend and Stive (1987). Their quasi-3D model divided the current into depth-variant and depth-invariant forcings. Haas and Svendsen (2000) found good agreement between their 3D model and laboratory measurements. The currents inside the surfzone were nearly depth uniform which developed into a surface current offshore of the wave breaking. A quasi-3D model, used by Haas et al. (2003), found that the bottom stress affects the stability of the rip and theorized that wave-current interaction could create low-frequency pulsations.

Haller and Özkan-Haller (2002) used a wave action balance equation including wave breaking dissipation to model rip current circulation. They were able to combine several models to simulate the depth-induced and current-induced wave breaking near rip currents. Kennedy and Kirby (2003) used an unsteady wave driver to model the nearshore circulation in response to wave groups. From the simulations, they found that the interaction of the wave groups and longshore uniformities in topography can produce strong edge wave resonance.

Murray (2002) developed a model to represent the hydrodynamic and sediment transport processes inside the surfzone for rip channel development on non-barred beaches. Murray et al. (2003) also develop a theoretical model to test non-bathymetrically driven rip currents. They found that these flash rip currents become less prevalent with steeper beach slopes and increased variations in incident wave heights.

1.1.4 Rip Currents and Sediment Transport

Sediment transport and the morphodynamics has been a key aspect in rip current generation. Vos (1976) first noted observations of the developmental stages of a transient rip current on the Western coast of Australia. Symonds et al. (1997) further characterized the development and decay of a rip with time-exposed video imagery. Short (1985) explained that strengthening and weakening of rip current systems changes the sediment transport rate and direction. He explained that erosion-type rips are strong, unsteady currents that transport large amounts of water and sediment across the breaker zone. Accretion rips are weak and less migrant currents that transport sediments at a slower rate than the general seaward accretion. Short also described an evolution from a strong erosion-type rip into an accretion-type rip during a change from high to low wave activity.

Tidal cycles also produce wave activity modulations that affect sediment transports. Aagaard et al. (1997) studied the sediment transport balance between the rip current moving offshore and incident waves moving shoreward during tidal cycles. The sediment pulses from these erosive rips have been documented to occur in the infragravity band (Allen and Psuty 1987). Cook (1970) noted that the material transported by these rip currents offshore is low density which leaves heavier grains on the beach. Brander (1999b) found that waves dominate currents for the entrainment of sediments, but currents dominate transport. Brander (2000) noted that nearly half of the sediments are transported in the bottom 10% of the flow. Brander also found that sediment transport was inhibited in the feeders but promoted in the rip neck. MacMahan et al. (2005) found an inverse relationship between sediment accretion on the bar and

deposition in the rip channel. Field measurements by Brander and Short (2000) in New Zealand demonstrated that large-scale rips in high-energy surfzones and low energy rips, although different magnitudes, showed similar morphodynamics behavior.

1.1.5 Laboratory Research

Early laboratory experiments of rip currents were with non-barred beaches. Bowen and Inman (1969) generated nearshore circulation cells in a laboratory basin by way of the interaction between edge waves and the incident waves. They noted that the rip currents were spaced at alternate antinodes of the edge waves making the rip spacing equal to the wave length of the edge waves. Another non-barred rip current experiment was done by Sasaki (1985) to measure the velocity profile of nearshore circulation currents. He concluded that rip currents reach maximum offshore velocity slightly offshore of wave breaking. Wind and Vreugdenhil (1986) analyzed a rip current from a longshore current diverted offshore by a sidewall.

Laboratory measurements of a rip current generated from a longshore bar with two rip channels were obtained by Haller et al. (1997a) and Haller and Dalrymple (1999). The flow velocity, wave height, and water levels were measured over a large area. Haller and Dalrymple (1999) noted both primary and secondary circulation systems. The primary circulation consisted of flow in the longshore feeder current turning offshore through the rip channel and eventually returning over the bar to the feeder. The secondary system, however, was shoreward of the bars and had an opposite rotation than the primary. Haller and Dalrymple also found that the mean circulation is driven by pressure gradients due to the variations in the water level. Haller et al. (1997a, 2002) noted the effect of wave-current interaction in the vicinity of the rip.

Drønen et al. (1999, 2002) also performed laboratory experiments of a rip current using a wave tank with a half channel. The current and surface elevation measurements were primarily focused in the rip channel and supplemented with flow visualization techniques. Drønen et al. (1999) noted a stagnation area revealed by the Lagrangian trajectories in the rip channel where the long-time-averaged current "separated" from the bed. Drønen et al. (2002) also investigated the vertical structure of rip currents and found that the flow in the rip channel was fairly uniform. Flow direction, however, was found to be highly depth-variant near the bar crest. The wave breaking location relative to the bar crest was also reported to greatly affect the flow into the rip channel.

Haas and Svendsen (2000, 2002) conducted a more extensive investigation into the vertical variation of rip currents. Using three velocity gauges at different depths, they found strong depth variations offshore of the breakers but nearly depth uniform velocities inside the channel. The flow offshore of the channel was measured to have a strong surface current with a weak and sometimes shoreward velocity near the bottom. They found that the depth variations are highly dependent on the total volume flux in the rip.

Recent laboratory experiments by Kennedy and Thomas (2003) made use of Lagrangian drifters to investigate rip current circulation. They found that circulation is very unsteady, changing at various length and time scales. The generation of circulation was estimated to be much larger than the mean circulation.

1.1.6 Rip Current Pulsations

The pulsating nature of rip currents on the wave group timescale was first noted by Shepard et al. (1941) but has since been observed by many (Shepard and Inman 1950, Sonu 1972, Aagaard et al. 1997, Brander and Short 2001). The forcing mechanism for

these pulsations within the infragravity frequency band has yet to be conclusively found. Shepard and Inman (1950) proposed that these pulsations were related to the groupiness of the incoming waves. They theorized that during the larger waves, more water is transported within the surfzone creating an excess storage of water shoreward of wave breaking. The water eventually exits through hydraulically more efficient rip channels creating wave group timescale pulsations. Sonu (1972) used nearshore drifters and aerial photography at Seagrove Beach, Florida to characterize the meandering and pulsating behavior of rip currents. Sonu gave another hypothesis, concluding that the pulsations were due to infragravity standing waves within the surfzone. Field observations from MacMahan et al. (2004a) support the theory of Sonu (1972) that infragravity rip pulsations are linked to standing infragravity motions.

Pulsations of much lower frequency than the wave groups have also been observed (Smith and Largier 1995, Brander and Short 2001, MacMahan et al. 2004a, Callaghan et al. 2004). Smith and Largier (1995) and Brander and Short (2001) stated that shear instabilities may be the cause of these low frequency pulsations. These low frequency pulsations have also been observed in a laboratory setting (Haller 1998). An instability analysis of a rip current jet was performed by Haller and Dalrymple (2001) using laboratory experiments to calibrate the Bickley jet model. They found that the observed unsteady motions evident in the laboratory measurements could be predicted with an instability model. Another implication is that surfzone eddies could produce these low frequency pulsations (MacMahan et al. 2004b, Reniers et al. 2002). There have been several observations of detached eddies in the rip head that relate to rip current pulsations (Smith and Largier 1995, Johnson and Pattiaratchi 2004, MacMahan et al.

2004b). Field measurements by MacMahan et al. (2004b) have suggested that the observed surfzone eddies are not from rip current jet instabilities. They produced a model that can explain the low frequency energy in the surf zone with rip circulation cell oscillation. Reniers et al. (2004) also used a model to show that incident wave groups can produce low-frequency vortices. Callaghan et al. (2004) suggested another possible mechanism for these low frequency pulsations. Their observations suggested that pulsations can be driven by fluctuating mass transport over the bars. This supports the previous model of Aagaard et al. (1997) that relates rip flow to the mass transport in the waves and in the rollers.

Field observations note important characteristics of infragravity and sub-harmonic pulsations. Allen and Psuty (1987) observed infragravity excitation in the cross-shore rip channel velocity but sub-harmonic energy at the bars. A series of field studies performed on Herzilyya Beach, Israel under low energy conditions observed long period oscillations in the rip system. Both the rip neck and longshore feeders were observed to have significant energy in the sub-harmonic and infragravity bands (Bowman et al. 1988a, 1988b, 1992). Brander and Short (2001) also observed pulsations at infragravity frequencies in both the feeder and rip currents at Palm Beach, Australia. Johnson and Pattiaratchi (2004) observed dominant infragravity energy during their field study in Perth, Australia but claimed that a significant variable velocity component was not related to infragravity motions.

1.1.7 Particle-Tracking Velocimetry

Flow velocities in laboratory experiments can be measured from the displacement of particles contained in the flow over short time intervals. The optical recording of this

particle-displacement for use in flow velocity determinations is known as particle-image velocimetry. The density of particles within an image is critical for determining the most efficient velocity calculation technique. High-density situations are common for typical particle-image velocimetry methods, involving the displacement measurement of a small group of particles as one unit. For low-density situations, it is often more efficient to measure displacements by tracking individual particles. This low-density technique is known as particle-tracking velocimetry (PTV) (Adrian 1991).

Particle-tracking velocimetry originates from classical flow-visualization techniques. These classical methods have been used to provide qualitative descriptions of flow situations for many decades. Reviews and examples of classical flow-visualization techniques can be found in Merzkirch (1974), Lauterborn and Vogel (1984), and Van Dyke (1982). Early quantitative measurements of these flow-visualization descriptions involved manual quantification, such as by Fage and Townend (1932). More recent flow-visualization techniques utilize digital imagery making quantitative analyses much more precise. A review of flow-visualization using digital imaging can be found in Hesselink (1988).

Particle-tracking velocimetry can be divided intro single-frame and multiframe techniques. Single-frame methods involve particle locations at multiple times on an image, such as streaked photography or pulsed exposures. A multiframe technique allows each sample of the particle-contained flow field to be viewed on a separate image. Willert and Gharib (1991) were one of the first to use a digital video camera to record particle-image sequences. Reviews of both single-frame and multiframe techniques can be found in Adrian (1991).

Hesselink (1988) outlined image processing techniques that scientists have used to distinguish particles or streaks from the background in an image. He first mentions a threshold analysis, where the quantized irradiance of a pixel is compared with a predetermined scalar. Pixel intensities that are larger than the threshold are retained and considered part of the particle image. He notes that the choice of threshold may influence the size of the detected region. Hesselink also notes a convolution technique to extract the edges of the particle area.

Several methods have been developed to track identified particles from one frame to the next. Frieden and Zoltani (1989) illustrate a nearest neighbor approach for relating particles between frames. Another tracking method involves cross correlation of consecutive image-groups to determine individual particle pairing (Perkins and Hunt 1989, Uemura et al. 1989, Cowen and Monismith 1997). Others have used a model to predict the location of the same particle in the next frame (Adamczyk and Rimai 1988, Etoh and Takehara 1992).

Methods for particle tracking beneath water waves have been developed by Hering et al. (1997a). Their experiments involve tracking particles over several wave periods (longer than typical PTV tracks). The Lagrangian description obtained from the particle trajectories are shown to be much more useful than Eulerian measurements for easily and accurately calculating the mean flow properties (Hering et al. 1997b). Thomas (2003) performed Lagrangian tracking of drifters in laboratory rip currents using digital video from his experiments at the Ocean Engineering Laboratory at the University of Delaware.

Lagrangian tracking on the field-scale has been conducted by Davis (1985) and Schmidt et al. (2003). Davis (1985) used 164 current-following drifters to observe energetic mesoscale features in the near-surface coastal currents off the coast of Northern California. The drifters were located by radio transmission using triangulation of onshore receiving stations. Schmidt et al. (2003) measured surfzone circulation using GPS-tracked drifters. The drifters were deployed in a fully-developed rip current and recorded eddy-like trajectories.

1.2 Outline of Present Work

The focus of the present research is to develop a better understanding of rip current system dynamics under a controlled laboratory setting. Both in situ measurements and video-based techniques allow a quantification of the laboratory rip current system. General rip current behavior and pulsations are analyzed for various incident wave conditions.

Correlations between wave conditions and rip current strength, density, and spacing have been documented by previous scientists (Shepard et al. 1941, McKenzie 1958, Huntley and Short 1992, Shepard and Inman 1950, Cook 1970, and Lascody 1998). However, the responses of the individual components of a rip current system (longshore pressure gradients, feeder currents, and cross-shore pressure gradients) under various wave conditions have not been studied extensively. This research investigates the mean behavior of rip current systems for a variety of normally-incident wave conditions in a controlled environment.

Both infragravity and lower-frequency pulsations have been observed in rip current measurements (Shepard and Inman 1950, Sonu 1972, Smith and Largier 1995,

Aagaard et al. 1997, Brander and Short 2001, MacMahan et al. 2004a, Callaghan et al. 2004). There are several theories on the forcing mechanisms of these rip current pulsations including wave groupiness, standing waves, instabilities, and mass-flux variations. This research investigates the pulsation behavior in a rip current system using much more extensive measurements.

In Chapter 2, the experimental methods are presented for obtaining data from the laboratory tests. Explanations of the techniques for both the in situ and optical measuring of the flow field are given. A description of the data mining process for the video is also included.

In Chapter 3, the methodology for computing the rip system properties is discussed along with an error analysis for the technique. The mean properties of rip current systems for various incident wave conditions are also discussed.

In Chapter 4, the pulsations observed in the laboratory measurements are characterized. The timing of the pressure gradients, feeder currents, and rip currents are related and discussed in this chapter.

The final chapter summarizes the research presented within this thesis and gives conclusions that can be reached from the study as well as suggestions for future studies.

CHAPTER 2

EXPERIMENTAL METHODS

The unpredictable nature and spatial meandering of rip currents make detailed measurements of rip current systems difficult in the field. With instrumentation possible at only a few discrete points, it is often difficult to characterize the dynamics of the entire system. In a laboratory setting, a wave basin with fixed topography eliminates the elusiveness of the rip current such that the location of the feeder currents and rip currents are always known.

The experiments presented in this thesis investigate the horizontal spatial and temporal nature of rip currents under various wave conditions. Two different methods are used to characterize the rip current system: in situ instrumentation and optical measurements of surface drifters. These experiments are among the most extensive spatially and temporally rip current measurements to date.

The first section of this chapter presents the experimental description for both the in situ and optical-based experiments. A description of how the particles are tracked from the digital video is given in the second section along with an error analysis of those techniques.

2.1 Experimental Description

Many different rip current experiments have been conducted in the directional wave basin in the Ocean Engineering Laboratory at the University of Delaware for several years. Haller et al. (1997b, 1998, 2002) used in situ measurements in the wave

basin to describe the mean rip characteristics for six different monochromatic wave conditions. Haller and Dalrymple (2001) used these measurements of the mean rip velocity profile for an investigation into rip-jet instabilities. The vertical structure of rip currents was investigated by Haas and Svendsen (2002) by measuring water velocities at three different depths at different points along the rip channel. Kennedy and Thomas (2003) used Lagrangian drifters and instrumentation to characterize rip current circulation for deep water conditions in a small region of the wave basin. The present experiments add to these laboratory measurements of rip currents by providing a spatially-large and time-varying perspective of the rip current system as a whole.

The geometrical dimensions of the wave basin (model geometry scale 1:10) are shown in Figure 2.1. A multi-paddle wave maker creates waves that propagate across a short 1:5-sloped offshore section to a longer and milder 1:30-sloped nearshore. Centered at 11.8 m from the offshore wall is a longshore bar with two channels. Details of the design and construction of the wave basin and bars are found in Haller et al. (2000).

The multi-paddle wavemaker is programmed to generate experimental wave conditions using the Designer Waves theory by Dalrymple (1989). Only shore-normal wave conditions are used for these experiments and, therefore, the sidewall wave reflection is neglected. Both monochromatic and bi-chromatic wave conditions are generated with various wave amplitudes and incident periods. For the bi-chromatic conditions, the group period and ratio between the amplitudes of the two wave components (a_1/a_2) are also varied.

The Froude number is the most important dimensionless parameter in scaling the experimental wave conditions. To obtain Froude similarity with a geometrical length

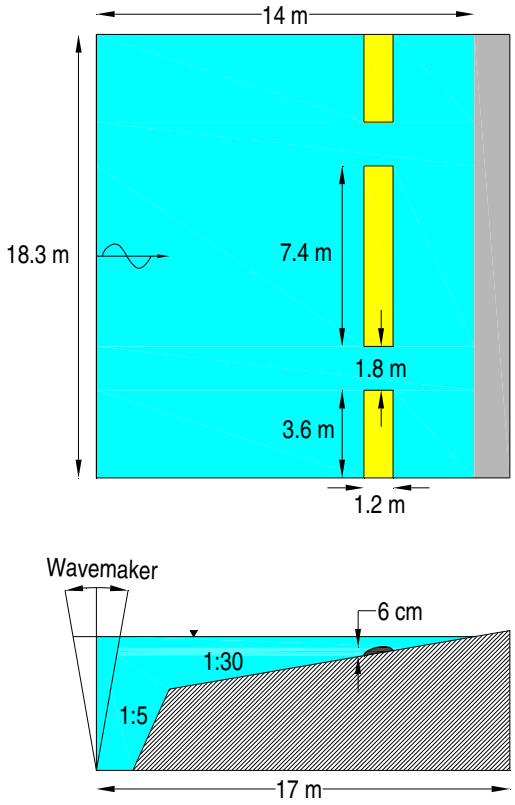

Figure 2.1: Basin geometry with plan view (top) and profile (bottom)

scale of 1:10, the wave celerity for the experimental waves should be $\sqrt{10}$ times larger than the prototype. Therefore, all length scales are scaled 1:10 while the time scale is $1:\sqrt{10}$.

Both in situ instruments and optical-based methods are used to measure the horizontal spatial variation of rip current circulation patterns for each wave condition. The in situ measurements include both water level and velocity measurements at key locations in the flow domain. For the optical-based measurements, Lagrangian drifters circulating throughout the wave basin are captured with digital video.

The laboratory measurements are performed in two different experimental sets. The first set, conducted in 2002 by Kevin Haas and Andrew Kennedy, contains 24 in situ

and 25 video experiments with different wave conditions for an offshore water depth of 70.36 cm. For the second set of experiments, modifications are made to the instrument layout for the in situ measurements and the lighting for the optical-based method. This 2004 set, conducted by Kevin Haas, Brian Sapp, and Andrew Kennedy, contains 14 in situ and 9 video experiments with different wave conditions at the same offshore water depth of 70.36 cm.

2.1.1 Experiments with In Situ Sensors

Two types of instruments are used for measuring the flow conditions in the wave basin: Acoustic Doppler Velocimeters (ADV's) for velocities and capacitance wave gauges for the water level measurements. One wave gauge is mounted on an offshore tripod to monitor the offshore conditions while the remaining instruments are mounted on a movable bridge spanning the longshore dimension of the basin. Both the horizontal coordinates and depth under the water surface for each instrument are determined with a measuring tape using marks on the bottom of the basin from a previous survey.

For the 2002 experiment set (F), nine ADV's and ten wave gauges are used for instrumentation. The arrangement of instruments is shown in Figure 2.2. The instruments are placed to resolve the left feeder and the rip in the channel. The left feeder is chosen since it was the dominant feeder current in previous experiments by Haller and Dalrymple (1999). Based on the 2002 experiments, it is discovered that the left feeder is not the dominant feeder current in all cases. The 2004 experiments (H), therefore, are setup to resolve both feeder currents. Eight ADV's and ten wave gauges are positioned to measure the feeders, rip channel, and offshore water level as shown in Figure 2.3.

The capacitance gauges are wired to a computer in a control room and data from them are stored at 10 Hz. The ADV's are connected to 2 computers near the wave basin and sampled at 20 Hz. The data collection is synchronized with an electrical pulse sent from the wave gauge computer to both ADV computers. In order to eliminate start-up effects, the wave maker is started and run for approximately five minutes before data acquisition begins. Each test runs for 27.3 min to obtain 16,384 wave gauge points and 32,768 ADV points. The target wave conditions for both the F and H in situ series are given in Tables 2.1 and 2.2, respectively.

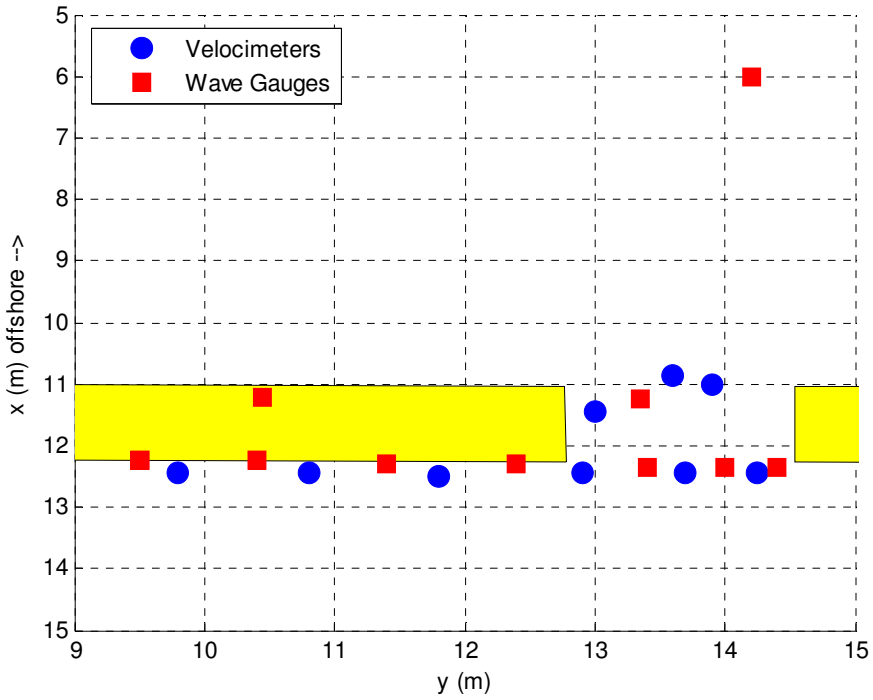

Figure 2.2: Instrument layout for the F series experiments

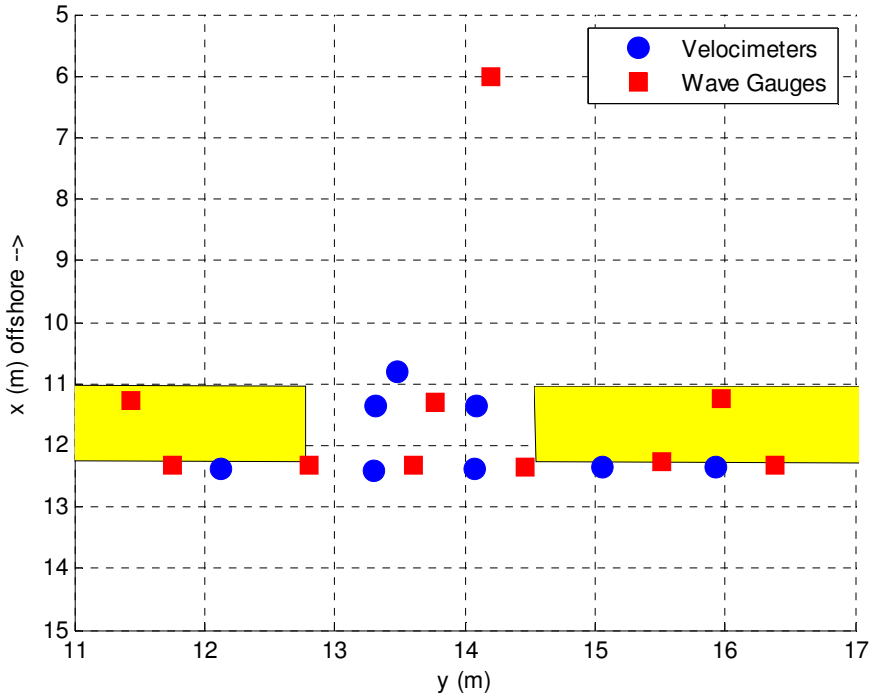

Figure 2.3: Instrument layout for the H series experiments

2.1.2 Optical Experiments

The optical-based experiment involves capturing digital video of Lagrangian surface drifters floating through the flow field. The surface drifters are weakly buoyant flat disks shown in Figure 2.4 with a radius of 5.65 cm. Approximately 100 drifters are available for tossing into the wave basin during an experiment. Drifters that move offshore near the paddles or on the beach are collected and tossed back into the flow field to ensure consistent coverage of the flow field. At any given time during the experiment, 30-50 drifters are visible in the camera view. Each wave condition test is recorded for approximately 20 min.

The digital camera equipment used for capturing video data includes a Sony TRV-900 with three 1-mega pixel CCD chips equipped with a Raynox 0.66x wide-angle

Table 2.1: Table of wave conditions for in situ experiments in 2002 (F series)

Test	Period (s)	Amplitude (cm)	Group Period (s)	a_1/a_2
F1	1	3	--	--
F2	1	4	--	--
F3	1	5	--	--
F4	1.33	3	--	--
F5	1.33	4	--	--
F6	1.33	5	--	--
F7	1.5	3	--	--
F8	1.5	4	--	--
F9	2	3	--	--
F10	1	3	16	2
F11	1	3	32	2
F12	1	3	64	2
F13	1.33	3	16	2
F14	1.33	3	32	2
F15	1.33	3	64	2
F16	1.5	3	16	2
F17	1.5	3	32	2
F18	1.5	3	64	2
F19	2	2.5	16	2
F20	2	2.5	32	2
F21	2	2.5	64	2
F22	1	3	32	1
F23	1.33	3	32	1
F24	1.33	3	64	1

lens. The digital camera is connected to a PC by FireWire for real-time video capturing at 30 Hz. The video imagery resolution is 720 x 480 pixels.

The camera placement for the 2002 experiments provides a side view from atop an extension tripod at 7.01 m from the water surface. Adjustments are made to the setup of the 2004 experiments to minimize the lighting reflection on the water surface. These reflections cause great difficulties in tracking the drifters in certain parts of the basin. To overcome these difficulties, indirect lighting is used instead of the previously-used overhead fluorescent lights and the camera is placed on the beach of the wave basin

Table 2.2: Table of wave conditions for in situ experiments in 2004 (H series)

Test	Period (s)	Amplitude (cm)	Group Period (s)	a_1/a_2
H1	1.33	3	--	--
H2	1.33	3	32	2
H3	1.33	3	64	2
H4	2	2.5	--	--
H5	2	2.5	32	2
H6	2	2.5	64	2
H7	1.33	4	--	--
H8	1.33	2.5	--	--
H9	1.33	2.5	32	2
H10	1.33	2.5	64	2
H11	1.33	3	32	1
H12	1.33	3	64	1
H13	2	2.5	32	1
H14	2	2.5	64	1

Figure 2.4: A photograph of one of the surface drifters

instead of the side at a height of 6.85 m. The target wave conditions for both the G and I video series are given in Tables 2.3 and 2.4, respectively.

2.2 Data Mining from Video Imagery

This section describes the process of obtaining Lagrangian drifter tracks from the captured video. The purpose of the mining is to obtain quantitative and analyzable

Table 2.3: Table of wave conditions for optical experiments in 2002 (G series)

Test	Period (s)	Amplitude (cm)	Group Period (s)	a_1/a_2
G2	1.33	3	--	--
G3	1.33	4	--	--
G4	1.33	5	--	--
G5	1.33	3	32	2
G6	1.33	3	64	2
G7	1.33	3	32	1
G8	1.33	3	64	1
G9	2	3	--	--
G10	2	2.5	32	2
G11	2	2.5	64	2
G12	2	2.5	--	--
G13	1	3	--	--
G14	1	4	--	--
G15	1	3	32	2
G16	1	3	64	2
G17	1	3	32	1
G18	1.33	3	--	--
G19	1.33	4	--	--
G20	2	3	--	--
G21	1.33	4	--	--
G22	1.33	3	32	2
G23	1.33	3	32	1
G24	1.33	3	64	2
G25	2	2.5	32	2
G26	2	2.5	64	2

Table 2.4: Table of wave conditions for optical experiments in 2004 (I series)

Test	Period (s)	Amplitude (cm)	Group Period (s)	a_1/a_2
I1	2	2.5	--	--
I2	1.33	2.5	--	--
I3	1.33	4	--	--
I4	1.33	2.5	32	2
I5	1.33	2.5	64	2
I6	2	2.5	32	1
I7	2	2.5	64	1
I8	1.5	3	--	--
I9	1.5	3	32	2

information from the video data. This is obtained using three main steps: individual particle identification, rectification from pixel to real-world coordinates using direct linear transformation, and frame-to-frame association to link individual particles into tracks. Each of these steps is described in detail below with an analysis of the errors introduced by the tracking and rectification schemes.

2.2.1 Particle Identification

The particle identification process identifies and records the positions of every lone drifter in a video segment using a MATLAB program code designed specifically for the video sets contained in this thesis. The two video experiment series, G and I, are processed with the same basic procedure but contain a few case-specific modifications.

The first step is to transform the digital video into 15 Hz TIF-sequences. Adobe Premiere Pro is used to down-sample the AVI video segments into separate color TIF frames, which enables the loading and processing of each frame separately to reduce the amount of data in the workspace.

The first objective of the identification algorithm is to separate the non-moving static features of the video imagery from the moving dynamic features. To distinguish the static features, an average image is computed using every 50^{th} frame of the entire 20 minute TIF sequence. It is important to note that the 3.33-second interval corresponding to every 50^{th} frame is not a multiple of any of the experimental wave periods. The average computation using every 50^{th} frame in the sequence gives a good representation of the static features with 2% of the processing time required to use every image. The static averaged image for experiment I6 is shown in Figure 2.5.

Figure 2.5: Static averaged image from video experiment I6

Shown in Figures 2.6 and 2.7 are examples of raw frames from experiments G2 and I6, respectively. By subtracting the static image from these raw video frames, the dynamic features become numerically more intense than the background, as seen by the white regions in Figures 2.8 and 2.9. Typical dynamic features include the drifters, wave crests, lighting reflections, and subtle changes in the water surface due to incoming waves. The light reflections from the 2002 experiment set is greatly reduced with the lighting and camera placement modifications for the 2004 set as seen by comparing Figures 2.6 and 2.7.

The next step in the process is to separate the drifters from the other dynamic features by applying an intensity threshold to the mean-subtracted image. Drifters have a higher contrast with the background than most other dynamic features and, therefore, are more intense after image subtraction. The intention of the intensity threshold is to generate a logical array where each pixel corresponding to a drifter portion is represented by a 1 with a background of 0's. Since preliminary investigations with both video sets

Figure 2.6: TIF snapshot from video experiment G2

Figure 2.7: TIF snapshot from video experiment I6

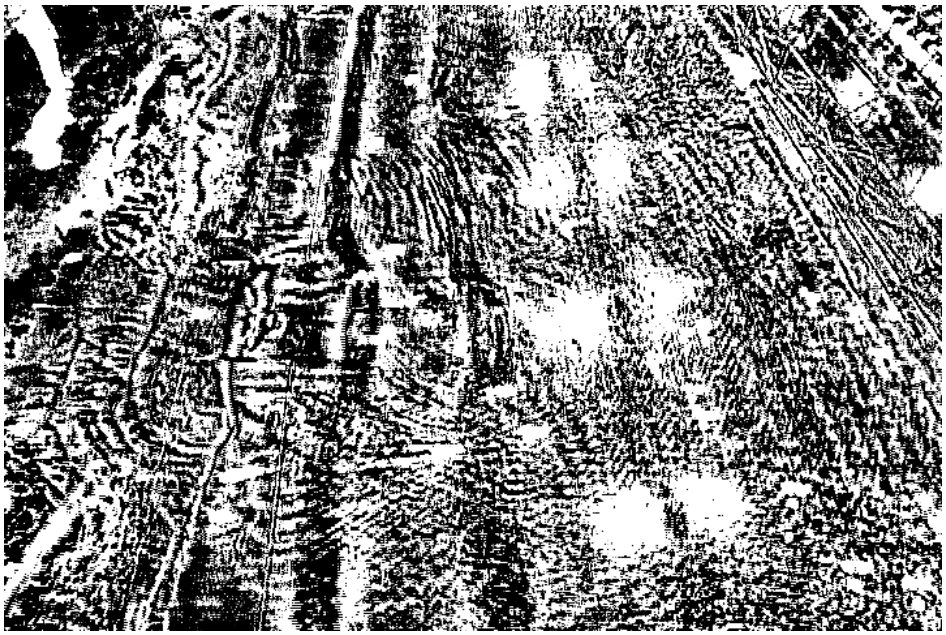

Figure 2.8: Mean-subtracted image for a frame in experiment G2 (Figure 2.6) showing moving dynamical features as more intense (white)

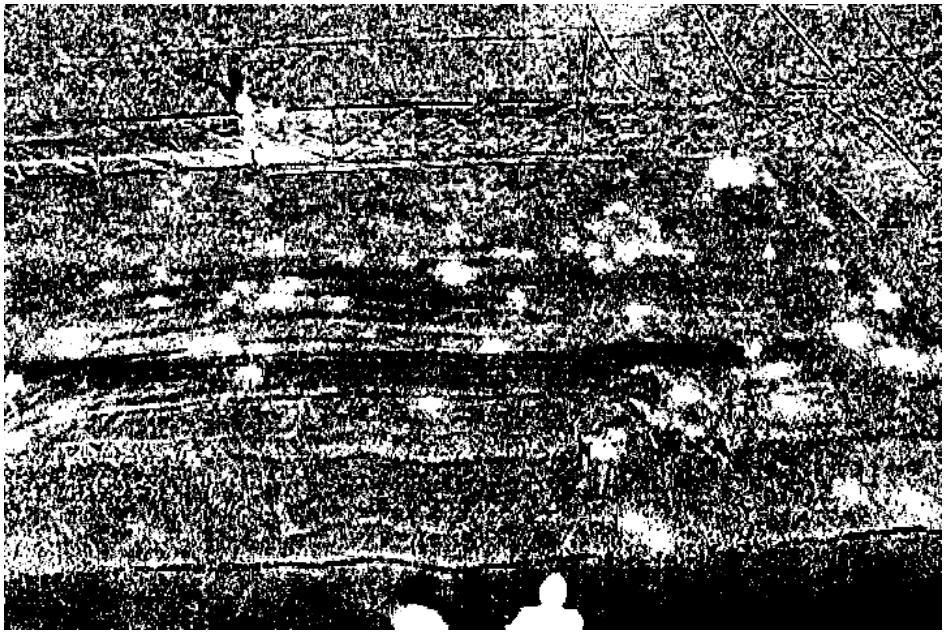

Figure 2.9: Mean-subtracted image for a frame in experiment I6 (Figure 2.7) showing moving dynamical features as more intense (white)

indicate that the highest color contrast between a drifter and the background exists in the green component of the RGB images, the intensity domain for thresholding is based solely on the green component.

The threshold for separating the drifters is found to be highly dependent on lighting and distance from the camera. The empirically-determined thresholding scheme is defined as

$$L(u,v)=\begin{cases}1 & , I_{dy}(u,v) > \kappa\cdot\left[\frac{0.25}{479}(v-1)+0.75)\right]I_{st}(u,v)\\ 0 & , I_{dy}(u,v) \le \kappa\cdot\left[\frac{0.25}{479}(v-1)+0.75)\right]I_{st}(u,v)\end{cases}, \qquad (2\text{-}1)$$

where (u,v) are the horizontal and vertical pixel locations (origin at top left of image), L is the resulting logical image that defines drifters with 1's, I_{dy} is the dynamically intense mean-subtracted image, I_{st} is the static average image, and κ is a empirical set-specific constant. The bracketed expression in Equation 2-1 allows pixels at the top of the image that are further from the camera to have a lower threshold than bottom pixels. This is necessary to ensure the drifter edges far from the camera are included as part of the drifter. Also, due to uneven basin lighting, dim areas of the basin have a lower contrast with the drifter and need a lower threshold to include the entire drifter. By using the static image intensity as a parameter in the thresholding scheme, dimmer areas are given a lower threshold. The set-specific constant accounts for the lighting differences in the two experimental sets; series I is darker and requires a lower threshold than the G series. The constants were determined empirically to be $\kappa = 1/3$ for series G and $\kappa = 1/4$ for series I.

Some restrictions are applied to ensure that features in non-trackable regions are excluded from consideration. A limiter that is utilized in both video sets is a perimeter boundary; areas of the video that are outside the basin are masked. A user-defined image is created for each video set to define the boundary around the basin. The red tint in Figure 2.10 represents pixel locations that are defined to be outside of the basin perimeter by the boundary image. To avoid partial particles along the perimeter, a buffer zone (blue) is similarly defined between the open basin and outer boundary. Image portions within the buffer region are not masked, but particle centers falling in this region are not considered for tracking.

Figure 2.10: Removed boundary (red) and buffer (blue) regions for experiment series I

The 2002 set also employs a reflection-reduction feature that is not necessary for the 2004 set. The reflections from the overhead lights produce dark features at their edges with intensities similar to drifters. In attempt to alleviate false drifters in the glares, areas near a reflection are not considered for tracking. However, since the reflections

move along the water surface, masked areas are frame-dependent. The application of the reflection-reduction feature first involves identifying the reflections in a frame. A logical array is created to locate reflections by finding pixels brighter (lower intensity) than the 20^{th} percentile. Every pixel that is identified as a reflection is padded with a one pixel boundary in attempt to capture the dark edges (high intensity) around a bright reflection (low intensity). After the padding, all the identified pixel locations, demonstrated by the green-tinted areas in Figure 2.11, are given a value of 0.

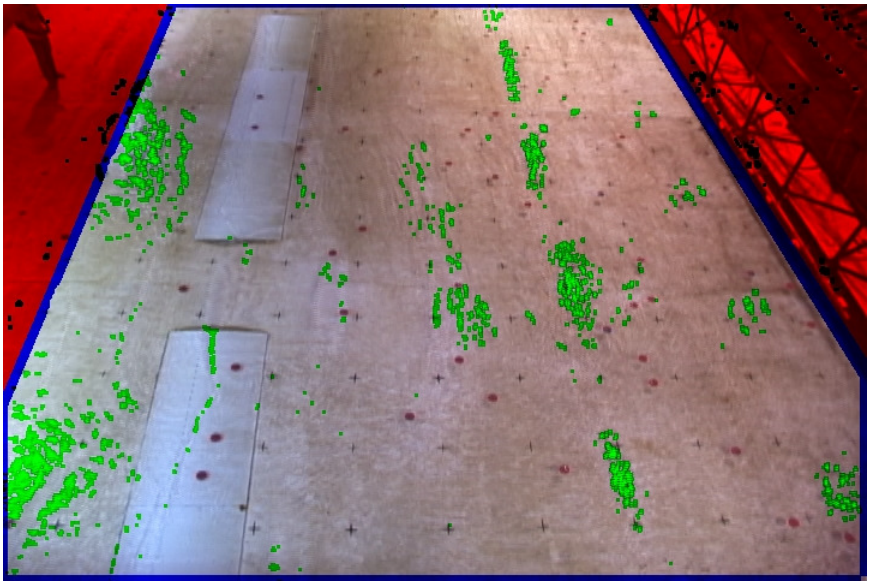

Figure 2.11: Removed reflection (green), removed boundary (red), and buffer (blue) regions for experiment series G

The result of intensity thresholding and region refinement produces a logical image where 1's (white) are the intense dynamic features in a trackable area and the 0's (black) are the background. Figures 2.12 and 2.13 show the binary images resulting from intensity thresholding and refinement of the two frames shown in Figures 2.6 and 2.7, respectively.

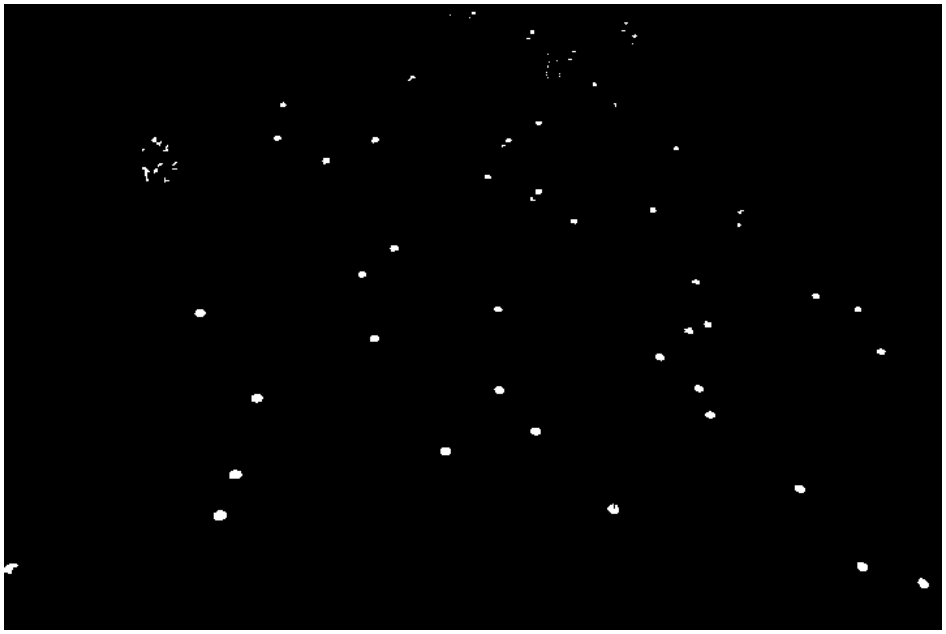

Figure 2.12: Logical image after region refinement for experiment G2

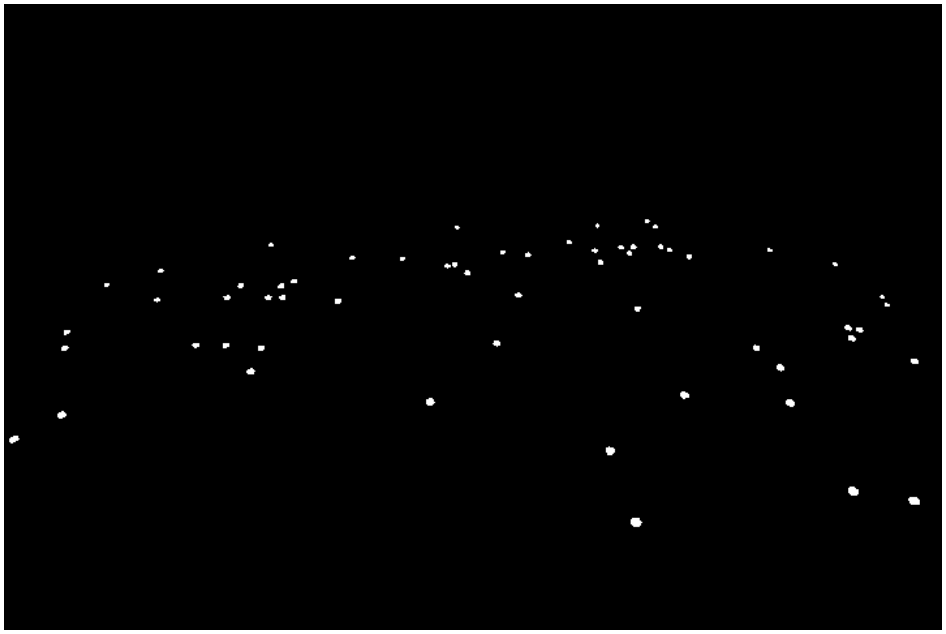

Figure 2.13: Logical image after region refinement for experiment I6

MATLAB contains several functions in the Image Processing Toolbox that are helpful in analyzing logical arrays. Instead of individually treating the pixels, the processing at this stage turns to analyze each grouping of 1's. The intrinsic function *bwlabel.m* is used to label each group of connected components with a unique numeric label. Pixels are considered connected if bounded by at least one of the four primary sides; corner-bounding is not considered connected.

Another function in the toolbox, *regionprops.m*, is used to compute properties for each identified image region. Area, centroid, and the bounding box are three of the many properties that can be computed for every connected region. Area is the number of pixels contained in each region; the centroid is the center of the region in pixel coordinates; and the bounding box provides the coordinates of the smallest rectangle capable of containing the image region. The centroid property computed with the Image Processing function produces a center based on the bi-chromatic image (i.e. binary center). Each pixel of a region receives the same weight in computing the center.

Since the area and centroid can be computed for each region, these properties are used to identify regions that demonstrate properties similar to a drifter. The relationship between drifter size and location is determined by manually identifying real drifters and false drifter regions for numerous video frames and plotting them as shown in Figures 2.14 and 2.15. Equations for bounds on the real drifters are chosen to include most of the drifters while eliminating most of the erroneous regions. For the G series experiments, the bounds are chosen to be

$$v_c \leq 80\sqrt{A} - 20 \tag{2-2}$$

$$v_c \geq 30(A)^{2/3} - 175 \tag{2-3}$$

for the upper and lower boundaries, where A is the pixel area of the particles and v_c is the vertical pixel location of the particle centers. The I series experiments bounds are chosen as

$$v_c \leq 55\sqrt{A} + 100 \tag{2-4}$$

$$v_c \geq 35(A)^{9/16} \tag{2-5}$$

for upper and lower boundaries.

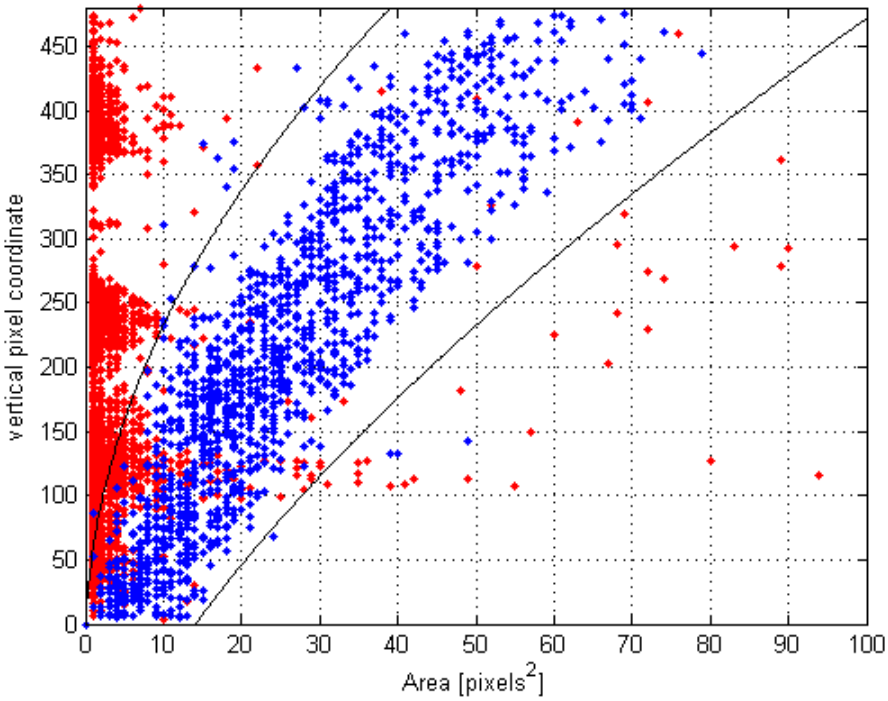

Figure 2.14: Bounds given by Equations 2-2 & 2-3 chosen as size conditions for accepting an intense region as a drifter based on manual sampling of regions (blue: drifters; red: erroneous regions) for experiment G2

These restrictions attempt to omit three unwanted features: noise, merged drifters, and people. Merged drifters occur when two drifters are close together appearing to be connected as one larger region. Excluding a real drifter or accepting an

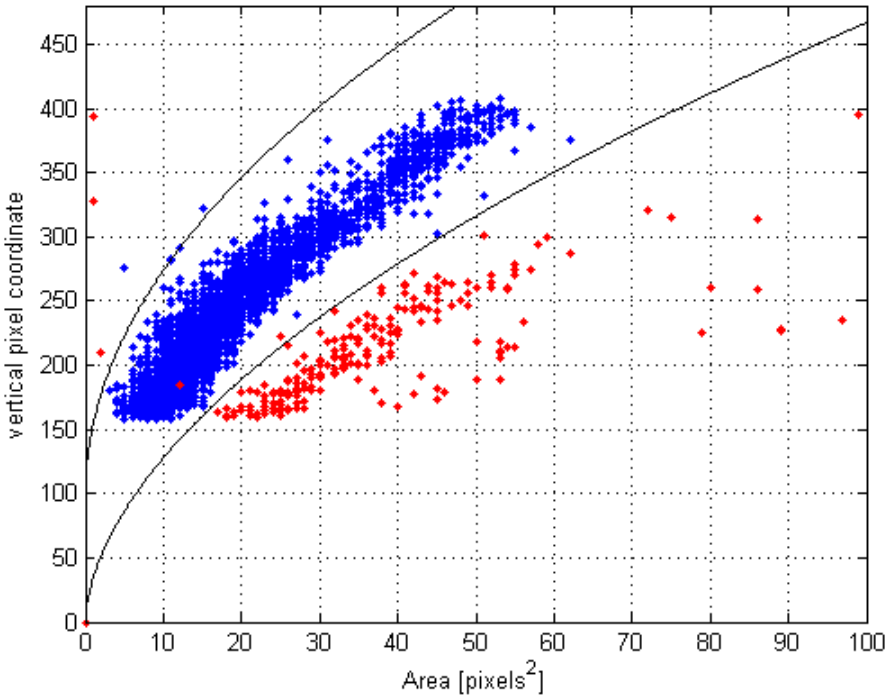

Figure 2.15: Bounds given by Equations 2-4 & 2-5 chosen as size conditions for accepting an intense region as a drifter based on manual sampling of regions (blue: drifters; red: erroneous regions) for experiment I6

erroneous region is not totally detrimental if it occurs intermittently; features in the frame-to-frame association accounts for both of these occurrences.

A centroid is then calculated for each region that fits the typical drifter profile. Because the centers of the drifters tend to be more intense, an intensity-influenced center of mass is calculated. Each pixel in the connected region is replaced with its green intensity value from the mean-subtracted image. This produces a drifter region with intense pixels having larger values than pixels that barely exceeded the threshold. To force intensity to be even more influential in the centroid calculation, the intensity values are cubed to strengthen the contrast.

For video test I6, the distance between centroid coordinates from the two methods (bi-chromatic and intensity-influenced) is minimal in most cases. The mean distance

between the 2 sets of centroid coordinates is 5.2 mm with a standard deviation of 3.1 mm. The situations where the method differences are large are visually investigated. Figure 2.16 shows a drifter where the difference in centroids between bi-chromatic and intensity-influenced is found to be the greatest. The non-white pixels seen in the drifter image indicate the pixels that passed the intensity threshold. For the bi-chromatic centroid method, each of the passed pixels has equal weight in determining the center shown by the green x-mark. The intensity-influenced center, shown by the red cross-mark, is shifted vertically since the bottom of the drifter is weaker in intensity than the top. Visual investigations like the one shown in Figure 2.16 revealed that the intensity-influenced center appears to be more accurate in cases where one of the drifter edges vanish.

All calculated centroid values are stored in an array by frame number. To avoid tracking when most of the drifters are initially being tossed into the basin, the particle identification is forced to start on frame 500. The coordinates are in a pixel coordinate system with sub-pixel precision. The centroid locations do not contain any linked tracking information at this stage; each coordinate is independent of every other point in the centroid array.

2.2.2 Transformation of Coordinates to Real-World System

The identified drifters are located in an image domain where the coordinates are in pixels. To transform these coordinates into the real-world system in the basin, a Direct Linear Transformation (DLT) method by Holland et al. (1997) is used. This method uses a camera model that is calibrated to transform the image domain into a real-world

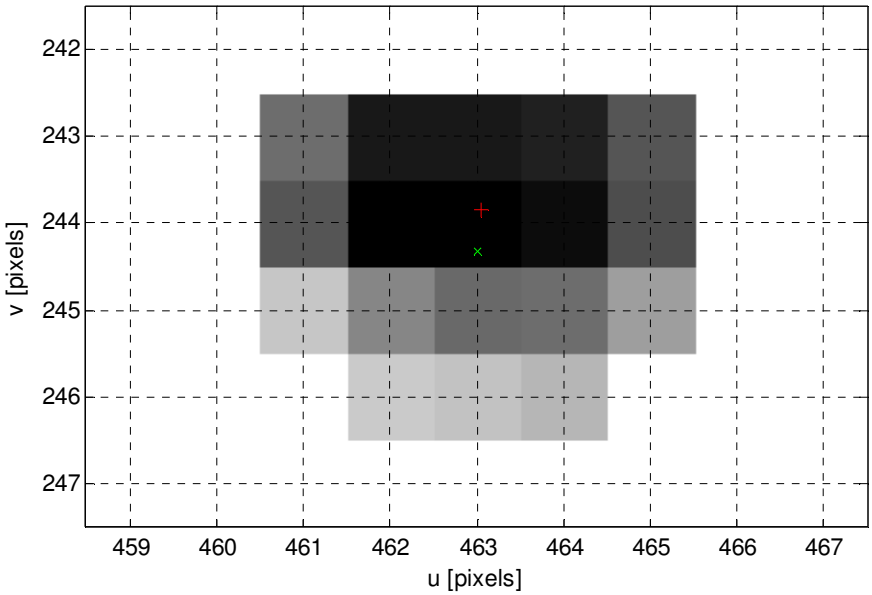

Figure 2.16: Drifter after intensity threshold showing the bi-chromatic centroid (x) and intensity-influenced centroid (+)

coordinate system. The model calibration involves two types: intrinsic camera properties and geometrical properties of the measurement setup. The intrinsic calibration quantitatively determines lens distortion, scaling factors, and the image center. Geometrical calibration involves the determination of the camera coordinates, focal length, and rotation angles. Since the transformation from a 2-D image coordinate system into a 3-D world domain is an underdetermined problem, Holland et al. presents two solution methods. The first method involves imposing an additional spatial constraint to the world coordinate system. Their second option uses two synchronized cameras in stereo to produce an over-determined system for the overlapping viewing area. For the present experiments, all of the drifter coordinates are constrained so that the elevation of each drifter is at the still water level. Details of the camera model, calibration, and rectification processes are explained in this section.

The model used to transform image coordinates into a rectilinear world coordinate system assumes that the camera is distortion-free. This assumption results in a collinear relationship between each image coordinate in the focal plane, the camera center, and its corresponding world coordinate. Figure 2.17 illustrates the camera setup with all of the parameters used to describe this collinear transformation.

The linear relationship between the image (u, v) and real-world coordinates (x, y, z) is given as

$$u - u_0 = -C_u \left[\frac{m_{11}(x - x_c) + m_{12}(y - y_c) + m_{13}(z - z_c)}{m_{31}(x - x_c) + m_{32}(y - y_c) + m_{33}(z - z_c)} \right] \tag{2-6}$$

$$v - v_0 = -C_v \left[\frac{m_{21}(x - x_c) + m_{22}(y - y_c) + m_{23}(z - z_c)}{m_{31}(x - x_c) + m_{32}(y - y_c) + m_{33}(z - z_c)} \right], \tag{2-7}$$

where the m_{ij} terms in the collinear relationship are known as the direction cosines given by the equations

$$m_{11} = \cos\phi\cos\sigma + \sin\phi\cos\tau\sin\sigma \tag{2-8}$$

$$m_{12} = -\sin\phi\cos\sigma + \cos\phi\cos\tau\sin\sigma \tag{2-9}$$

$$m_{13} = \sin\tau\sin\sigma \tag{2-10}$$

$$m_{21} = -\cos\phi\sin\sigma + \sin\phi\cos\tau\cos\sigma \tag{2-11}$$

$$m_{22} = -\sin\phi\sin\sigma + \cos\phi\cos\tau\cos\sigma \tag{2-12}$$

$$m_{23} = \sin\tau\cos\sigma \tag{2-13}$$

$$m_{31} = \sin\phi\sin\tau \tag{2-14}$$

$$m_{32} = \cos\phi\sin\tau \tag{2-15}$$

$$m_{33} = -\cos\tau, \tag{2-16}$$

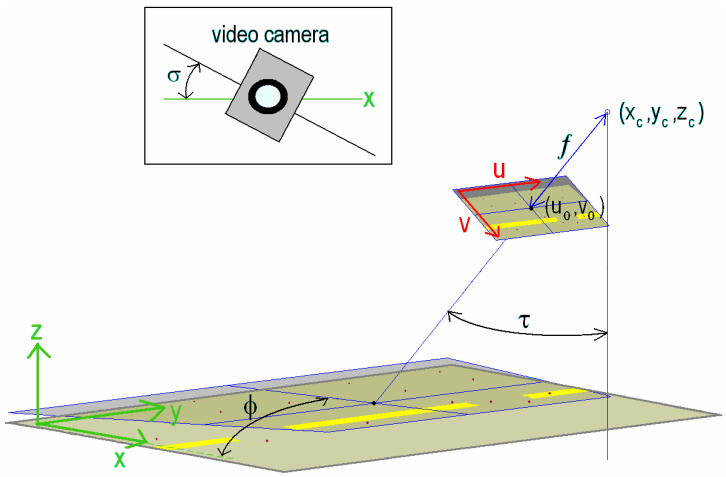

Figure 2.17: Schematic of the linear relationship between the image plane, real-world plane, and the video camera showing all rotation angles and focal length

where the angles ϕ (azimuth), τ (tilt), and σ (roll) are shown in Figure 2.17. Also in Equations 2-6 and 2-7 , C_u and C_v are calibration coefficients of the ratio of the focal length (f) to the horizontal and vertical scale factors (λ_u, λ_v) respectively.

Abdel-Aziz and Karara (1974) linearized the collinear relationship combining the eleven physical parameters into linear coefficients. These Direct Linear Transformation (DLT) coefficients define the image-to-world coordinate transformation linearly, but each coefficient does not have a physical meaning. The advantage to using the DLT equation is that an explicit solution can be obtained for each of the calibration coefficients as given by

$$L_1 x + L_2 y + L_3 z + L_4 - uL_9 x - uL_{10} y - uL_{11} z = u \qquad (2\text{-}17)$$

$$L_5 x + L_6 y + L_7 z + L_8 - vL_9 x - vL_{10} y - vL_{11} z = v\,, \qquad (2\text{-}18)$$

where (u, v) are the image coordinates, (x, y, z) are the real-world coordinates, and L_n are the DLT coefficients given as

$$L_1 = \frac{(u_0 m_{31} + f m_{11})}{\lambda_u L} \tag{2-19}$$

$$L_2 = \frac{(u_0 m_{32} + f m_{12})}{\lambda_u L} \tag{2-20}$$

$$L_3 = \frac{(u_0 m_{33} + f m_{13})}{\lambda_u L} \tag{2-21}$$

$$L_4 = -(L_1 x_c + L_2 y_c + L_3 z_c) \tag{2-22}$$

$$L_5 = \frac{m_{31}}{L} \tag{2-23}$$

$$L_6 = \frac{m_{32}}{L} \tag{2-24}$$

$$L_7 = \frac{m_{33}}{L} \tag{2-25}$$

$$L_8 = \frac{(v_0 m_{31} + f m_{21})}{\lambda_v L} \tag{2-26}$$

$$L_9 = \frac{(v_0 m_{32} + f m_{22})}{\lambda_v L} \tag{2-27}$$

$$L_{10} = \frac{(v_0 m_{33} + f m_{23})}{\lambda_v L} \tag{2-28}$$

$$L_{11} = -(L_8 x_c + L_9 y_c + L_{10} z_c), \tag{2-29}$$

where L is defined as

$$L = -(x_c m_{31} + y_c m_{32} + z_c m_{33}), \tag{2-30}$$

and (x_c, y_c, z_c) is the real-world camera coordinate and (u_0, v_0) is the center of the image domain.

Calibrating the transformation involves using corresponding sets of image coordinates and known world coordinates to explicitly calculate the DLT coefficients. Since there are eleven unknown DLT coefficients, calibration is achieved with six coordinate control sets (two equations for each set). The control coordinate sets needed to calculate the DLT coefficients are obtained from video imagery captured prior to wave generation. The wave basin has cross-hairs painted on its floor at 1-meter increments defining the world coordinate system as shown in Figure 2.18. Corresponding image coordinates of the cross-hairs are obtained using an intrinsic MALAB function *getpts.m*. This function allows the image coordinates of a mouse click to be stored. Each visible cross-hair in the still-water image is selected so that the image coordinates are obtained.

The calculation of the DLT coefficients is further simplified by translating the elevation of each coordinate to the still water level using refraction theory. Each cross-

Figure 2.18: Still water image showing the cross-hair marks on the basin floor used for control points in the DLT calibration

hair world coordinate on the basin floor (*x, y*) is translated to its apparent location (x_0, y_0) on the still water surface with the equations given by

$$x_0 = x - (x - x_c)\frac{h \tan \theta_r}{\sqrt{(x - x_c)^2 + (y - y_c)^2}} \tag{2-31}$$

$$y_0 = y - (y - y_c)\frac{h \tan \theta_r}{\sqrt{(x - x_c)^2 + (y - y_c)^2}}, \tag{2-32}$$

where (x_c, y_c) is the horizontal coordinates of the camera, h is the water depth, and θ_r is the refraction angle computed as

$$\theta_r = \sin^{-1}\left(\frac{\sin \theta_i}{N}\right), \tag{2-33}$$

where θ_i is the incident angle and N is the refractive index of water (1.33). All parameters for the translation are shown schematically in Figure 2.19.

This translation of the control points to the still water level ($z = 0$) eliminates three DLT coefficients (L_3, L_7 and L_{11}). This makes the calibration simpler but constrains the elevation of the drifter coordinates to the still water level. With this simplification, Equations 2-17 and 2-18 then become

$$L_1 x + L_2 y + L_4 - uL_9 x - uL_{10} y = u \tag{2-34}$$

$$L_5 x + L_6 y + L_8 - vL_9 x - vL_{10} y = v, \tag{2-35}$$

which can be combined into one matrix equation determinant with at least four coordinate sets given by

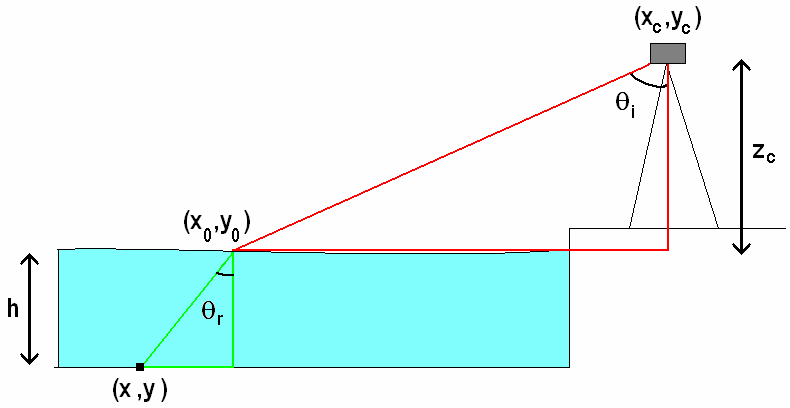

Figure 2.19: Schematic diagram of the translation of coordinates on the basin floor to the still water level

$$\begin{bmatrix} x_1 & y_1 & 1 & -u_1x_1 & -u_1y_1 & 0 & 0 & 0 \\ x_2 & y_2 & 1 & -u_2x_2 & -u_2y_2 & 0 & 0 & 0 \\ . & . & . & . & . & . & . & . \\ x_n & y_n & 1 & -u_nx_n & -u_ny_n & 0 & 0 & 0 \\ 0 & 0 & 0 & -v_1x_1 & -v_1y_1 & x1 & y1 & 1 \\ 0 & 0 & 0 & -v_2x_2 & -v_2y_2 & x2 & y2 & 1 \\ . & . & . & . & . & . & . & . \\ 0 & 0 & 0 & -v_nx_n & -v_nx_n & x_n & y_n & 1 \end{bmatrix} \begin{bmatrix} L_1 \\ L_2 \\ L_4 \\ L_9 \\ L_{10} \\ L_5 \\ L_6 \\ L_8 \end{bmatrix} = \begin{bmatrix} u_1 \\ u_2 \\ . \\ u_n \\ v_1 \\ v_2 \\ . \\ v_n \end{bmatrix}. \qquad (2\text{-}36)$$

The calibration of the DLT coefficients, however, utilizes a linear least-squares solution since more than four coordinate sets can be obtained for each test.

Another assumption of the camera model is that the camera is distortion-free with collinear relationships between the camera, an image coordinate in the focal plane, and the corresponding world coordinate. Lens distortion of the camera skews this collinear relationship. The intrinsic camera calibration corrects for lens distortion to improve the co-linearity.

The lens distortion calibration procedure involves creating a poster grid of evenly-spaced white circles on a black background. The poster grid is mounted perpendicular to

the video camera shooting line at a distance to include most of the circles on the poster in the viewing window. A short video segment is then captured of the grid. Adobe Premiere Pro is then used to extract a TIF snapshot from the short video segment. This image, shown in Figure 2.20, shows how the camera distorts a rectilinear grid. Notice that the line of circles around the edge of the video image appears curved from the lens distortion.

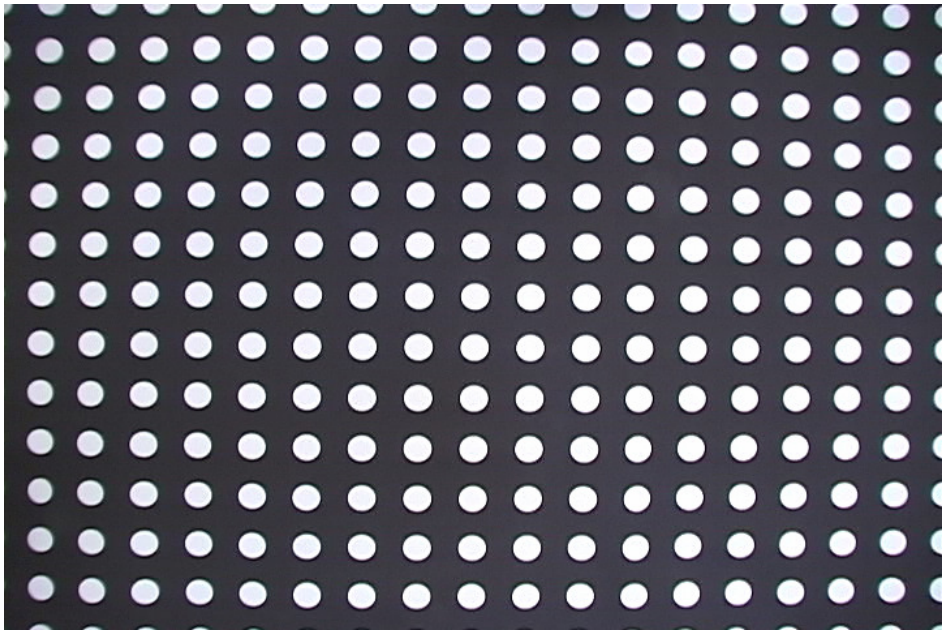

Figure 2.20: Distorted video image from a rectilinear grid showing effect of lens distortion

To obtain quantitative information from the image, centroid calculations similar to the method employed in the particle identification is used to find the center of each complete circle in the image. This creates a pixel coordinate for every visible circle on the poster grid. Holland et al. (1997) describes radial distortion, distortion along radial

lines from the image-center, to be the main source of camera lens distortion errors. The radial distortion (Δr) is modeled by a two-coefficient odd-order polynomial given as

$$\Delta r = k_1 r^3 + k_2 r, \tag{2-37}$$

where r is the pixel radius and k_1 and k_2 are model-fit parameters. Figure 2.21 shows the calibrated model-fit for the experimental video camera. Radial distortion of the camera is corrected by displacing each pixel according to the distortion model as shown in Figure 2.22.

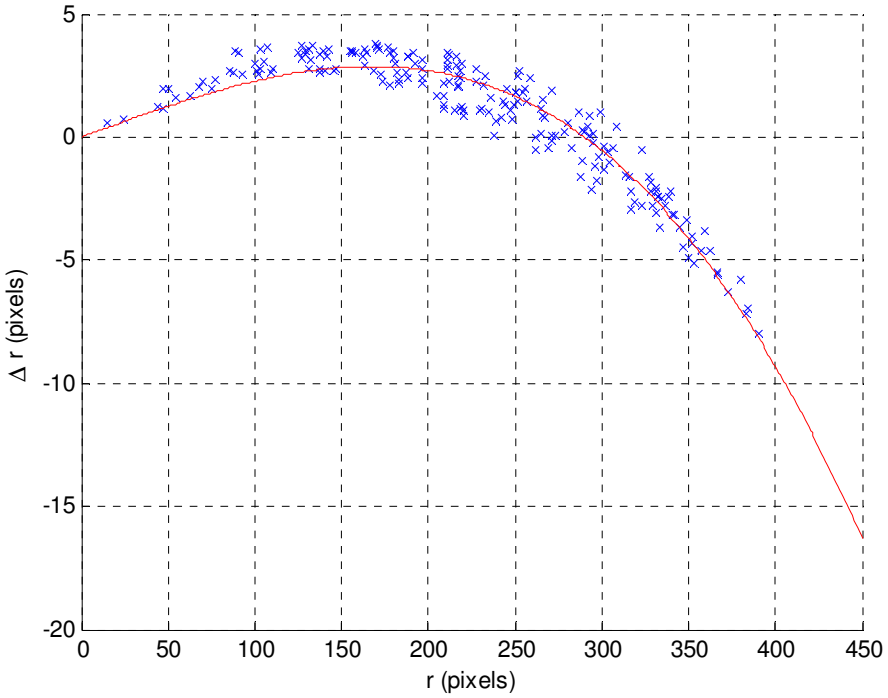

Figure 2.21: Radial distortion model-fit (blue x-marks: distortion measurements, red line: model-fit)

2.2.3 Frame-to-Frame Association

The frame-to-frame association procedure creates tracks of individual particles from the independent real-world drifter coordinates. The primary basis for the

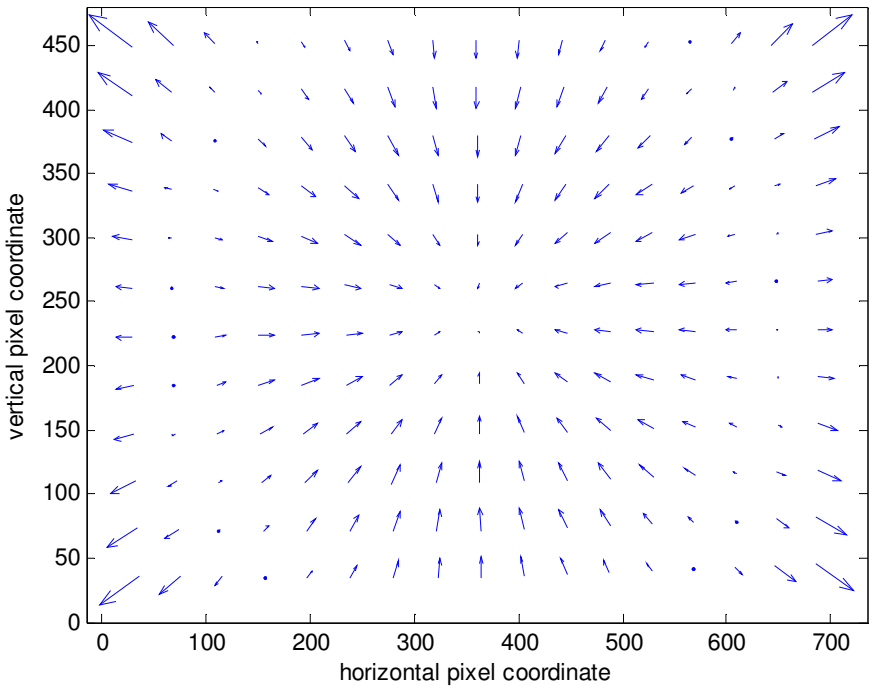

Figure 2.22: Radial distortion adjustments

association method is that the distance moved by each particle between consecutive frames is less than the radius of a drifter. The flow velocity has to exceed 85 cm/s to move a drifter more than its radius between consecutive frames; the laboratory-scale velocities in these experiments approach a maximum speed of 60 cm/s.

The drifter tracks are initiated by making each identified coordinate in the first frame the start of a track. In the subsequent frames, each coordinate is then compared with the tracks ending in the previous frame to find a match. This association method defines a possible match if the two coordinates are less than 5.65 cm apart (drifter radius).

There are four basic situations that can occur for the linking of the coordinates to tracks, which are displayed in Figure 2.23: 1) only one feasible match between a coordinate and track (one-to-one), 2) multiple coordinate options for continuing the track

(one-to-multiple), 3) a single coordinate that is feasible in multiple tracks (multiple-to-one), and 4) no coordinates are feasible for the track (one-to-zero). Under the first situation of a one-to-one match, which is almost always the situation, the coordinate is added to the track. For the infrequently-occurring one-to-multiple, multiple-to-one, and one-to-zero scenarios, the tracks are not continued with any coordinate.

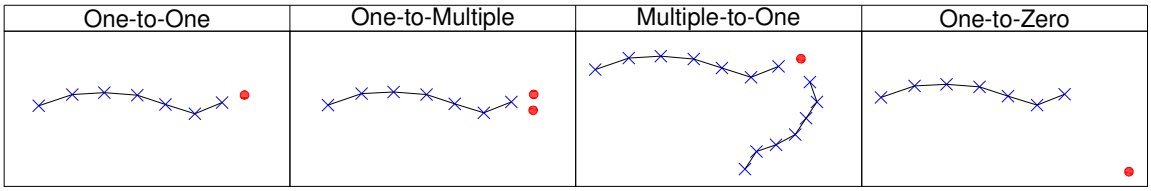

Figure 2.23: Four scenarios for the linking coordinates (red circles) into tracks (line with blue x-marks)

After all the one-to-one coordinate pairs are linked, the remaining unmatched coordinates are investigated for possible connections to tracks that have ended in the previous five frames. This allows a drifter track with a few missing coordinates to still be connected. If the last coordinate of any recently ending tracks are near an unmatched coordinate, the coordinate is added to the track. In associating a coordinate into a track ending prior to the previous frame, the same one-to-one association is used but with the allowable distance being a function of the number of frames between the two coordinates. Values between the end of the track and the coordinate-additions are linearly interpolated. All tracks that have lengths less than 150 frames (10 seconds) are deleted because of filter length restrictions. The 50 longest Lagrangian tracks of the 731 total tracks from video set I6 are shown in a rectified image in Figure 2.24.

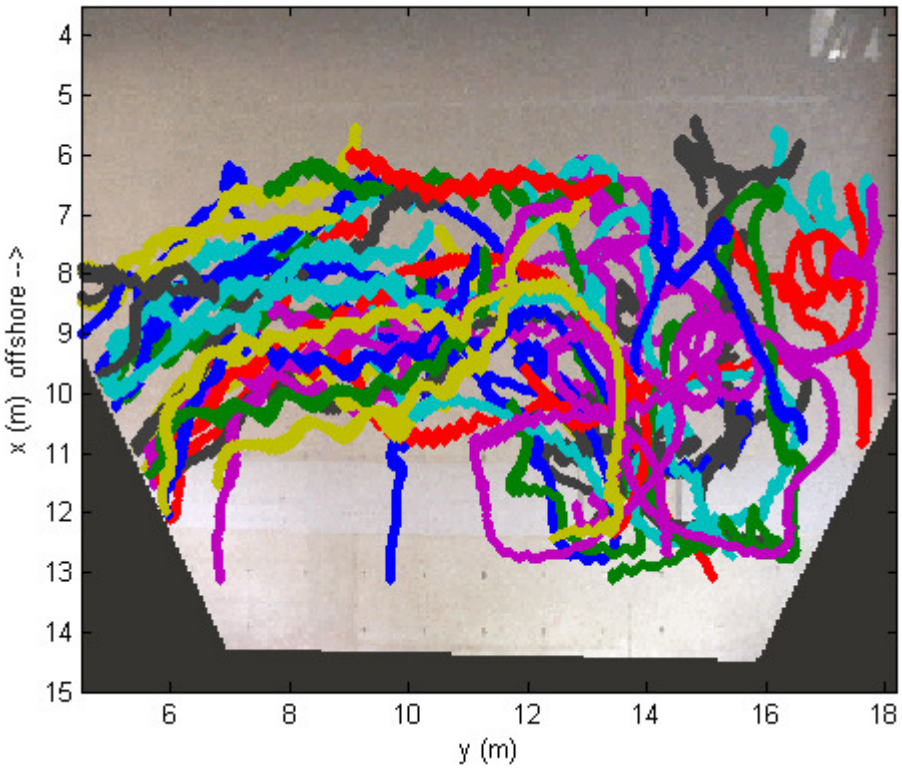

Figure 2.24: The 50 longest Lagrangian drifter tracks from experiment I6

2.2.4 Accuracy of Drifter Tracking

There are four primary sources of errors in the drifter tracking procedure: the image representation of a drifter, image noise, inaccuracies in the coordinate system transformation, and interpolation of missing drifter coordinates. These error sources are described in this subsection along with methods for alleviating the errors and estimates for the error magnitudes.

The drifters are cylindrical but are represented by regions of square pixels in the video image. Misrepresentations of the drifter could skew the calculated centroid coordinate. This effect is investigated by creating a square pixel bi-chromatic image of a circle. Pixels whose centers fall inside a given radius are issued a value of 1 with outside pixels of 0. Figure 2.25 plots the ideal circle in yellow with the pixel representation

shown with the white color and lines for pixel boundaries. The true center is shown with the blue mark and the calculated bi-chromatic center from the *regionprops.m* function in MATLAB is shown in red. As the center of the circle is moved away from the center of the square pixel, the representation becomes more asymmetric and the calculated center is less accurate. This analysis is performed for circles varying from radii of 1 to 5 pixels, which is the approximate range of drifters in a video, and different locations of the circle center inside the square pixel in the middle. The maximum error found for all radii and locations is 0.49 pixels, which occurs for the 1 pixel radius circle. The errors decrease with the circle size; the circle of an average drifter size (3-pixel radius), a maximum error of 0.27 pixels is found. Since the centroid calculations of the drifters are not bi-chromatic centers but intensity-influenced, it is expected that the more intense drifter centers will help to compensate and move the coordinate closer to the true center.

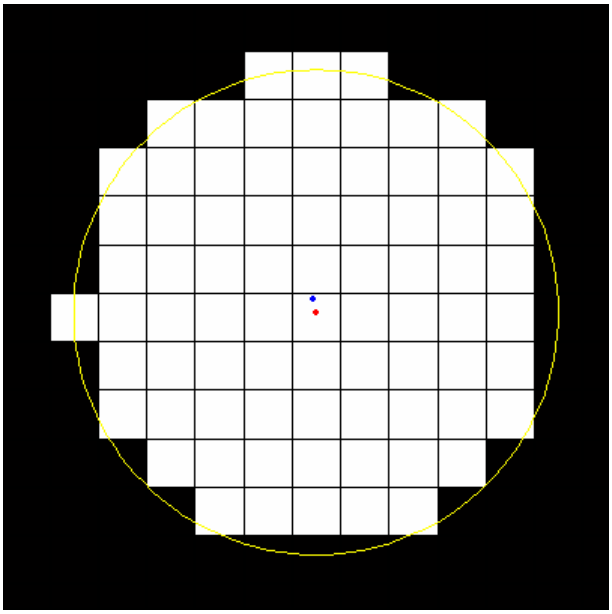

Figure 2.25: Square pixel representation of a circle with 0.27-pixel error for a 5-pixel radius drifter (yellow circle is true circle, blue mark is the true center, red mark is the calculated center)

Another source of error in the centroid calculation is image noise. The image noise, if more intense than the intensity threshold, can influence the center of mass of a drifter. The effect of noise is investigated by adding an area of noise as a circle outside the drifter to determine the shift of the centroid. Figure 2.26 shows the error model with the blue circle representing a drifter with added noise shown by the red circle. Using this model to analyze the error, the centroid shift (Δx) is calculated theoretically to be

$$\Delta x = \frac{R_d N^2 (1+N)}{1+N^2}, \tag{2-38}$$

where R_d is the radius of the circular drifter and N is the ratio of the noise radius to the drifter radius. For a circle with a radius of 1 pixel and the addition of 1 pixel of noise ($N = 0.5$), a shift of 0.3 pixels of the center is produced. For the average drifter size (3-pixel radius) with 1 pixel of noise ($N = 0.16$), a pixel shift of 0.09 pixels is calculated. The larger 5-pixel radius circle with the same noise area of 1 pixel ($N = 0.1$) produces a 0.05-pixel shift. The amount of image noise will increase with the size of the drifter. It is expected that 1 pixel of noise on a 1-pixel radius drifter is the maximum noise present in the experiments for the smaller drifters. The larger drifters, however, are more susceptible to image noise. With the addition of image noise to a drifter, it is also more uniformly distributed and hardly ever added to one side. For the effect of the centroid for a large 5-pixel drifter with 3 pixels of noise on one side ($N = 0.2$), the shift is 0.23 pixels. It is expected that the noise would be weaker in color intensity and therefore the intensity-influenced center would reduce the image noise errors.

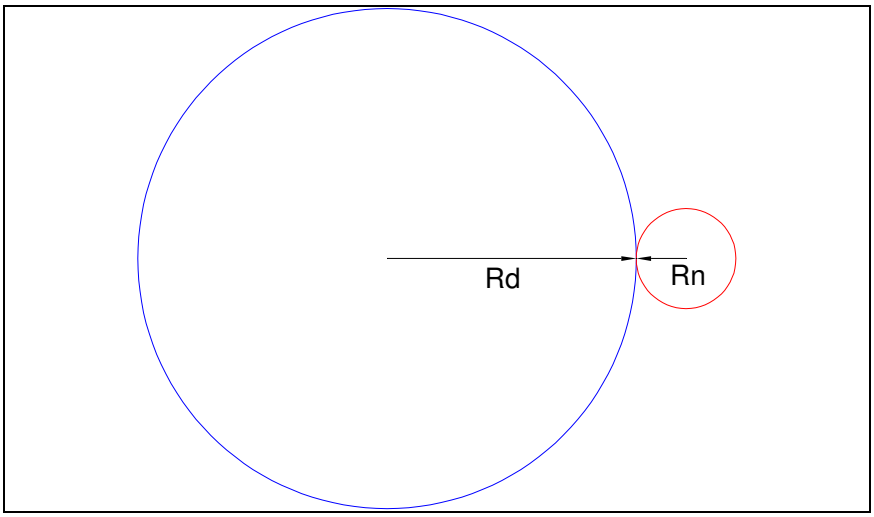

Figure 2.26: Error model for centroid calculation of a drifter (blue circle) with added noise (red circle) to one side

Pixels errors scale to different real-world errors based on the location of the drifter in the basin. Figures 2.27 and 2.28 show the real-world dimension in centimeters associated with a 1 pixel horizontal length in the image domain coordinate for sets I and G, respectively. The real world size of a horizontal pixel length ranges from 1.2 cm close to the camera to 2.8 cm further away. The orientations of the contour lines are different due to the difference in camera placement between the two data sets. Also, note that a horizontal pixel length in the image is primarily in the cross-shore direction for set G and in the longshore direction for set I. Figures 2.29 and 2.30 show the real-world dimensions in centimeters for a 1-pixel vertical length in the image for sets I and G, respectively. Notice that the real-world dimensions of the vertical pixel length are much larger than the horizontal. For both sets, the 1-pixel vertical length produces dimensions ranging from 1.5 – 6 cm and increasing with distance from the camera.

The coordinate system transformation model assumptions are also a source of error for the drifter coordinates. The DLT model assumes that the camera center, the

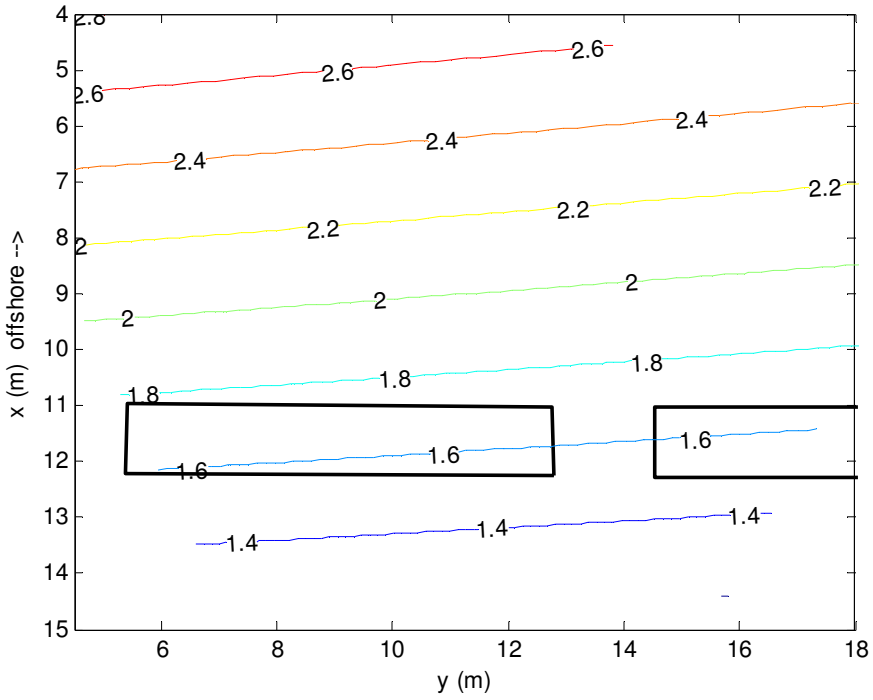

Figure 2.27: Real-world dimensions (cm) of a 1 pixel horizontal length in the image coordinate for experimental set I with camera location $(x_c, y_c, z_c) = (18.2, 11.6, 6.85)$ m

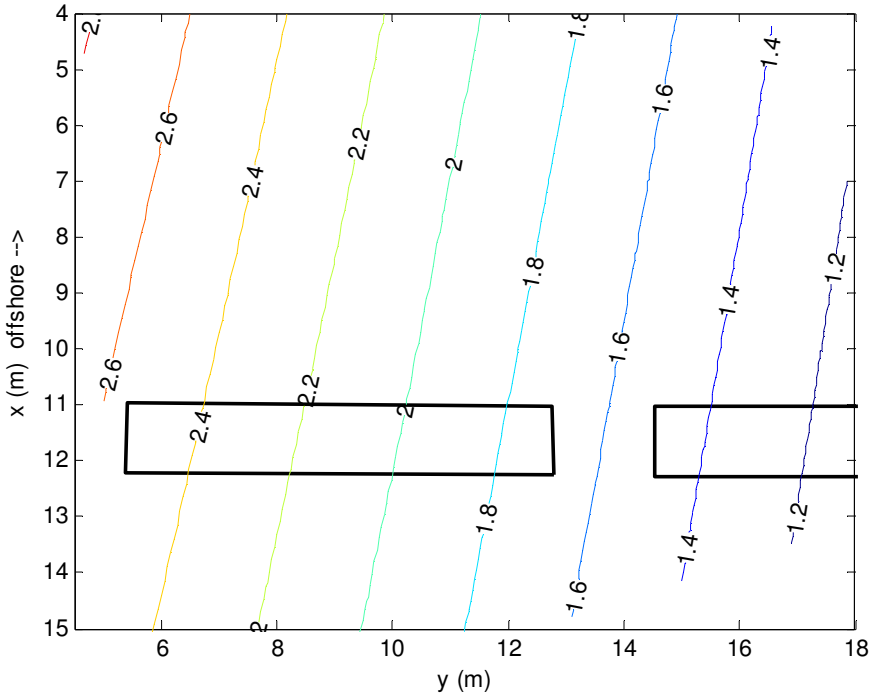

Figure 2.28: Real-world dimensions (cm) of a 1 pixel horizontal length in the image coordinate for experimental set G with camera location $(x_c, y_c, z_c) = (9.35, 19.65, 7.01)$ m

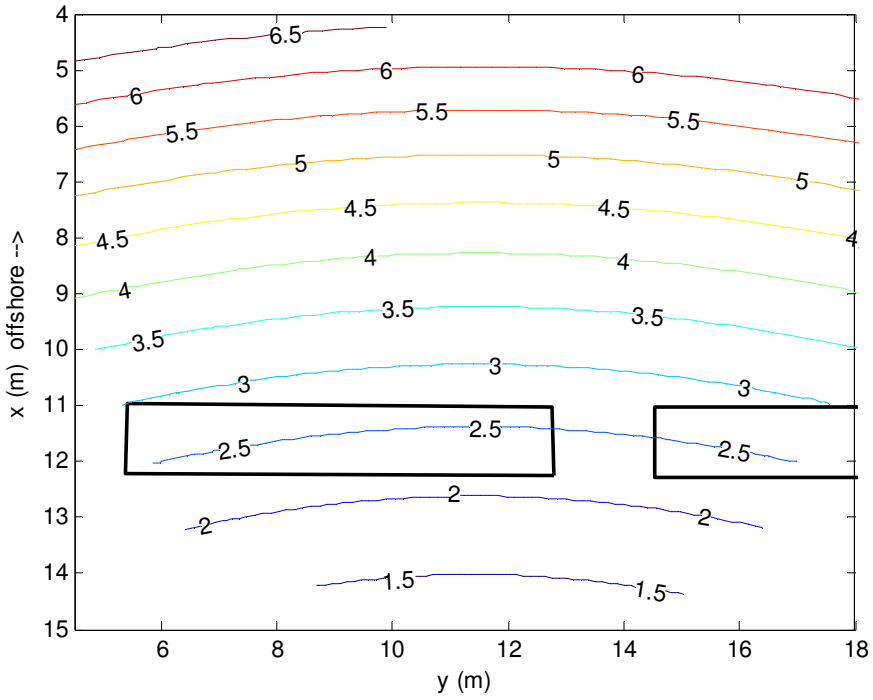

Figure 2.29: Real-world dimensions (cm) of a 1 pixel vertical length in the image coordinate for experimental set I with camera location $(x_c, y_c, z_c) = (18.2, 11.6, 6.85)$ m

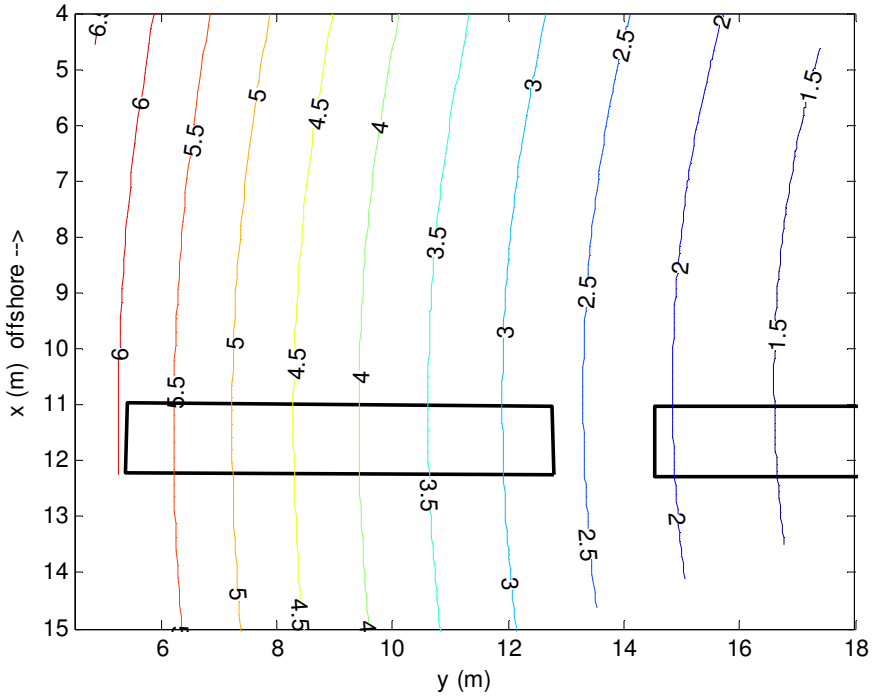

Figure 2.30: Real-world dimensions (cm) of a 1 pixel vertical length in the image coordinate for experimental set G with camera location $(x_c, y_c, z_c) = (9.35, 19.65, 7.01)$ m

image coordinate in the focal plane, and the real-world coordinate are collinear as discussed previously in this section. This assumption is reasonable but can introduce some errors in the drifter tracks. The error magnitude associated with the coordinate transformation methods are estimated from the 122 control points used in the model-fit for set G and the 69 points for set I. The root mean squared error for set G was 2.53 pixels corresponding to a 5.76 cm real-world error. For set I, the root mean squared error was 2.50 pixels and 4.52 cm. A major source of error is the lens distortion introduced by the camera; this reduces the validity of the collinear assumption of the model. To account for this error, the radial distortion model proposed in Holland et al. (1997) is used to un-distort the coordinates as discussed previously. With the correction added to the transformation, the error for set G is reduced to a 0.96 pixels and 2.48 cm error and error for set I is improved to 1.03 pixels and 2.35 cm.

Another source of error is the spatial constraint added to make the model solution determinant. It is assumed that the drifters are at the still water elevation throughout the experiment, but it is known that the drifters move vertically on the water surface with the passing waves. This vertical shift of the drifter is translated into an apparent horizontal shift as shown in Figure 2.31. The apparent horizontal shift (δ) varies depending on the line-of-sight angle (θ) and the free surface elevation (η) and can be described with the equation given by

$$\delta = \eta \cot \theta . \tag{2-39}$$

Since the line-of-sight angle depends on the drifter location in the basin and the free surface elevation, a contour map that shows the horizontal shift per free surface elevation (δ/η) throughout the basin is shown for both set I and G in Figures 2.32 and 2.33. The

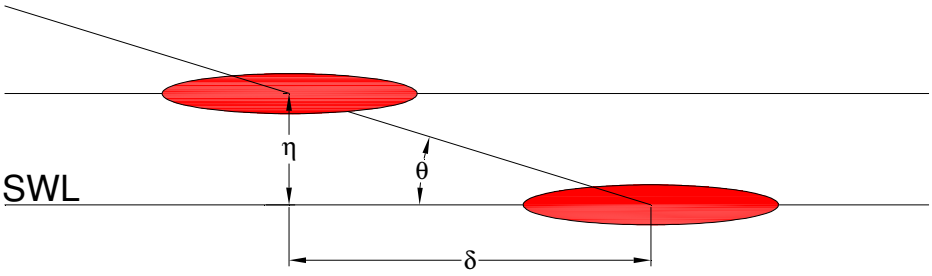

Figure 2.31: Elevation view of an apparent horizontal shift in the drifter location from a vertical shift in the elevation

ratio varies similarly in both sets from 0.25 – 2.25. For surface elevation amplitudes of 2 cm from the SWL, a range of errors in the horizontal drifter coordinate is calculated to be between 0.5 – 4.5 cm.

Another source of error is the linear interpolation between the gaps of a drifter track. The tracking method allows a maximum gap of four frames between drifter coordinates that are associated with the same track. The missing coordinates of the tracks are linearly interpolated to provide a continuous particle path. This interpolation of drifter position may introduce some errors to the drifter tracks. To investigate the scale of this problem, the number of frames for each interpolation and the physical length between the boundary coordinates are measured for video set I6. The average gap in I6 is 2.46 frames with the average distance between the coordinates being 2.68 cm. Although it is expected that the interpolation errors are minimal, there is no way to quantify the position errors since the actual path is unknown.

Filtering is used when calculating properties from these drifter tracks, which eliminates several of the errors mentioned in this section. Shown in Figure 2.34 is a segment of a raw drifter track prior to filtering. The noise is clearly seen in this track by

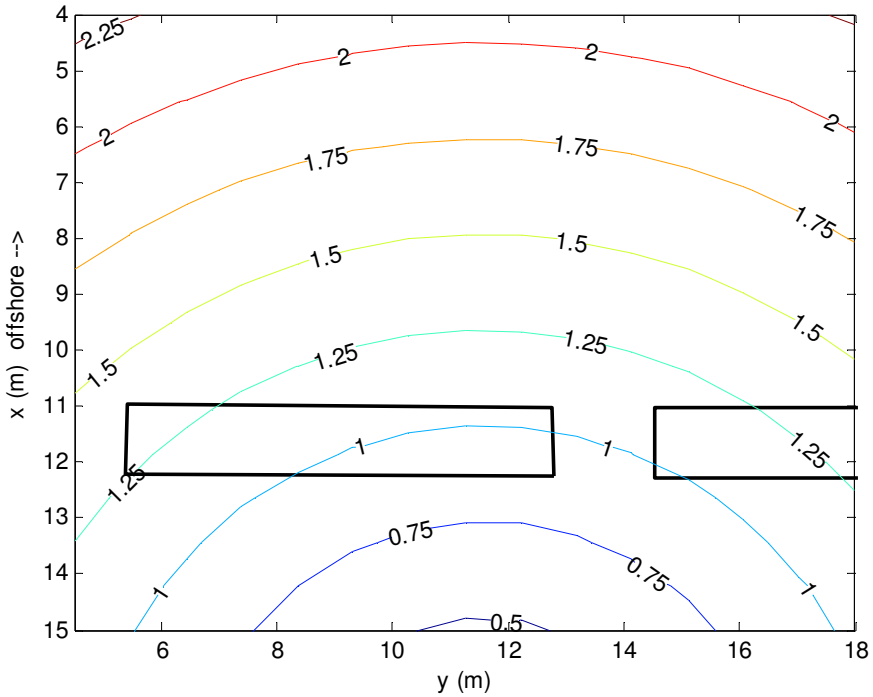

Figure 2.32: Ratio of horizontal shift to free surface elevation around the basin for set I

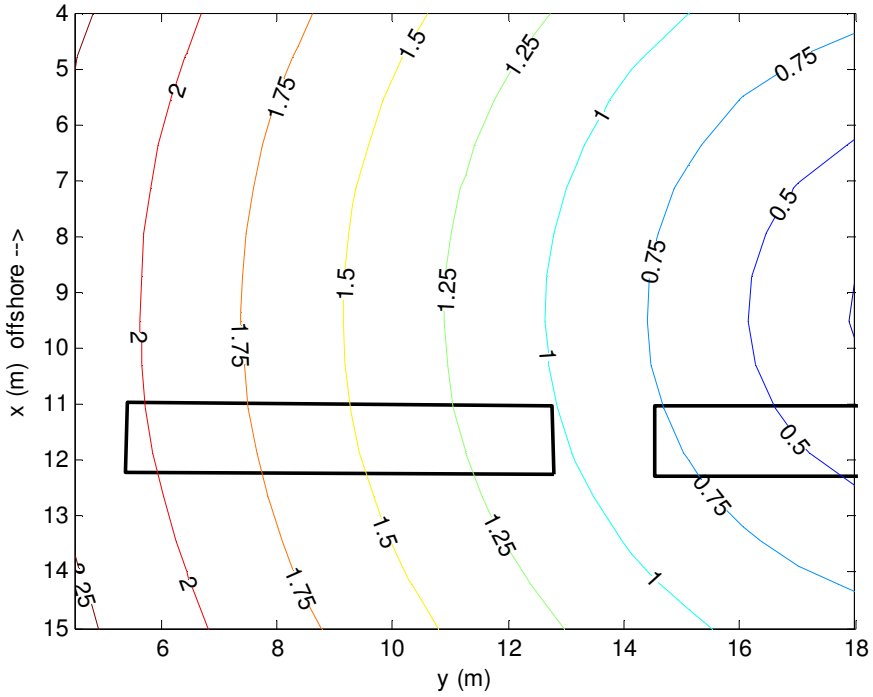

Figure 2.33: Ratio of horizontal shift to free surface elevation around the basin for set G

the sharp turns in the particle path. If velocity is computed directly from the raw track using forward differencing, the noise in the position data creates an even noisier velocity time-series. Figure 2.35 shows the cross-shore velocity time series computed from the raw track segment shown in Figure 2.34. Notice also that the wave motion is apparent in the drifter velocity time-series by the peaks every 2 s.

With low-pass filtering (cut-off frequency 0.05 Hz) of the drifter tracks but keeping the incident wave frequency, the high-frequencies typical of the mentioned errors are eliminated and the Lagrangian velocity from the track is less noisy and more useful for this analysis. The filtered track is shown in Figure 2.36 with the cross-shore velocity time-series computed from the track shown in Figure 2.37. By comparing the velocity time-series for the raw and filtered cases, it is clear that the noise associated with the drifter track is eliminated. Since the low-pass filter includes the incident wave frequency, the wave motion is clearly seen in the filtered track and velocity.

By moving the cut-off frequency lower than the incident wave frequency (cut-off frequency 0.33 Hz), the noise and wave motions are both eliminated during filtering leaving only the motions associated with the current. This low-pass filter of the drifter track is shown in Figure 2.38 with the corresponding velocity time-series in Figure 2.39. Notice that this low-pass filter produces a clean track and velocity signal. Low-pass filters are used in calculating the Lagrangian velocity of the drifters, as will be discussed in Chapter 3.

It is evident that the errors introduced by the tracking and rectification are greatly reduced by low-pass filtering. The discussed errors mostly occur on very short time-scales which can be eliminated with filtering. The raw drifter tracks are never used in

measuring the rip current system directly; filtering is always used. For computing the drifter track velocity, frequencies at or higher than the incident wave frequency are eliminated. It is clear from Figure 2.38, the low-pass filtered drifter track is very clean and the high-frequency tracking errors do not affect the velocity calculation. In Chapter 3, a technique is presented to compute wave heights from the drifter tracks. For this wave height calculation, the cut-off for frequency passing is higher than the low-pass frequency cut-off and, therefore, is more susceptible to the errors introduced by the vertical motions of the drifter. However, this is accounted for with a correction factor and will be discussed in Chapter 3.

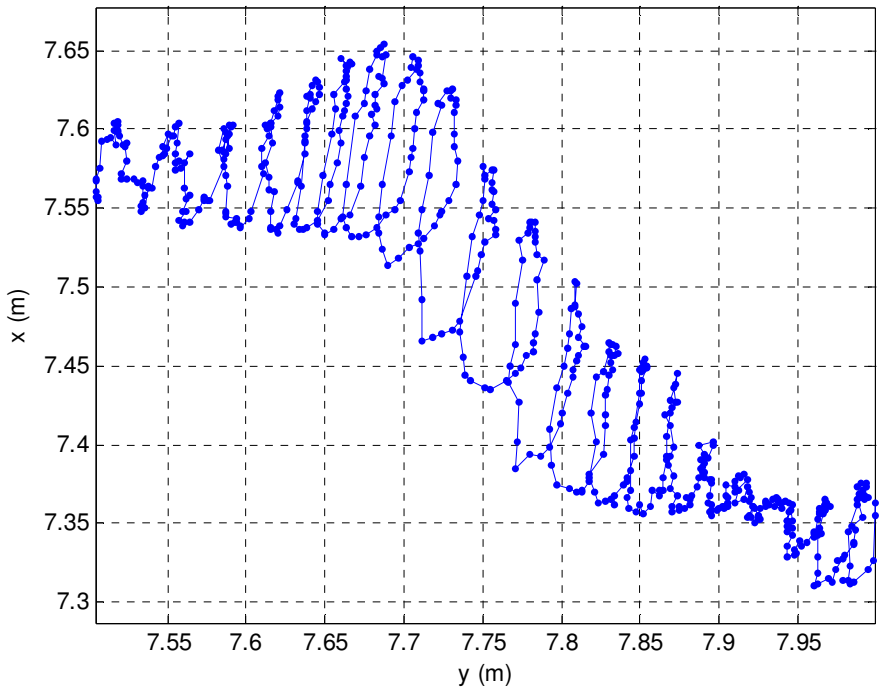

Figure 2.34: Raw drifter track segment from experiment I6

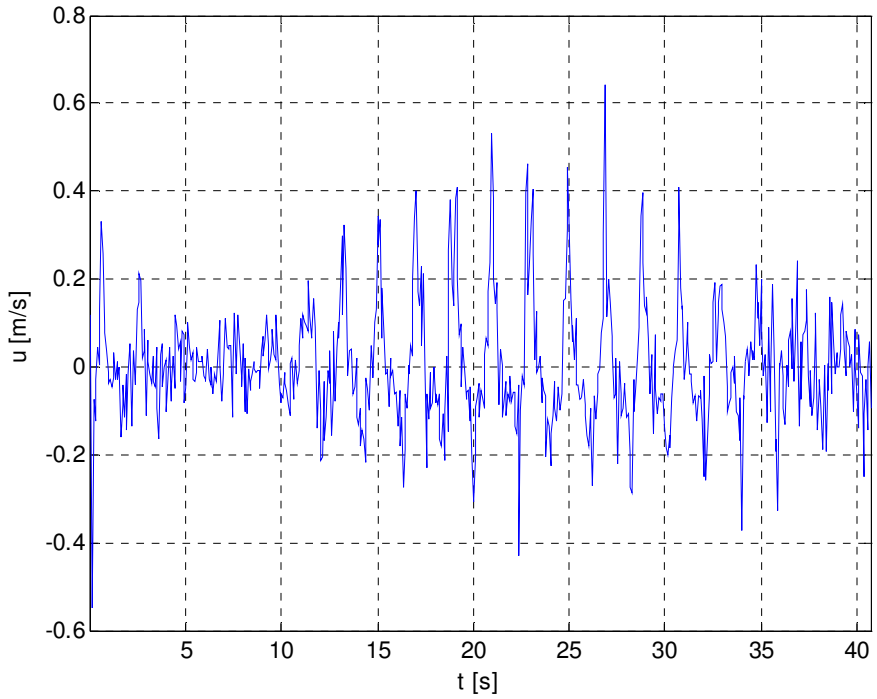

Figure 2.35: Cross-shore drifter velocity computed from the raw track segment from experiment I6

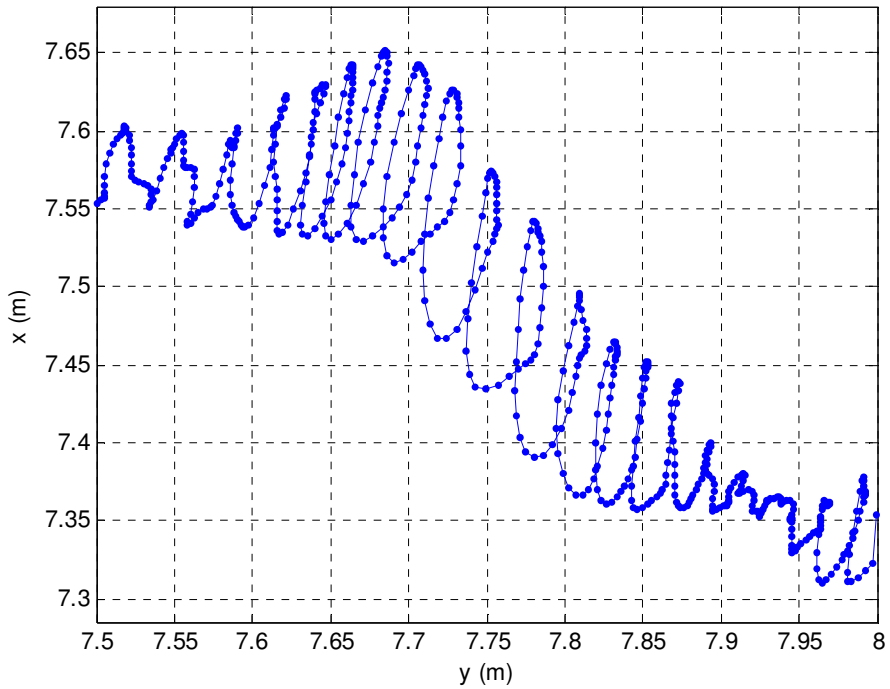

Figure 2.36: Low-pass filtered drifter track segment with a cut-off frequency of 0.05 Hz from I6 showing noise reduction

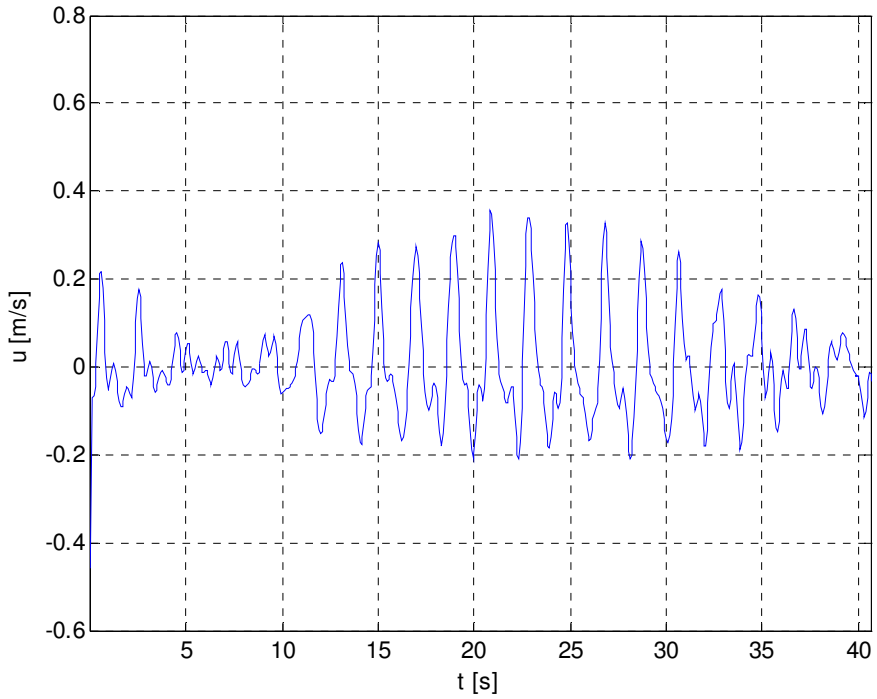

Figure 2.37: Cross-shore drifter velocity computed from the low-pass filtered track segment from experiment I6 showing noise reduction

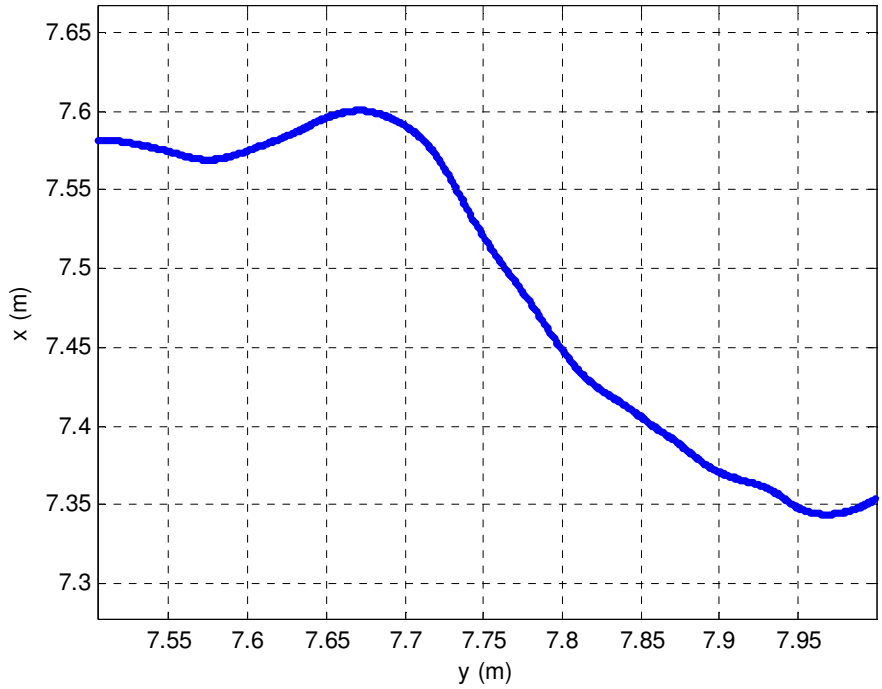

Figure 2.38: Low-pass filtered drifter track segment with cutoff frequency of 0.33 Hz from experiment I6 showing low-frequency motion

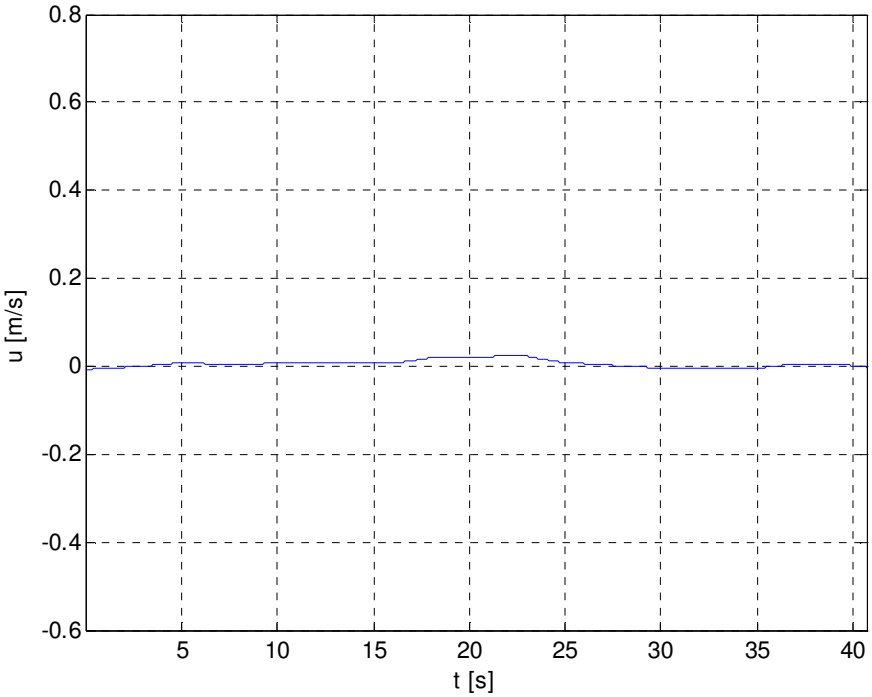

Figure 2.39: Cross-shore drifter velocity computed from the low-pass filtered low-frequency track segment from experiment I6

CHAPTER 3

MEAN PROPERTIES OF RIP CURRENT SYSTEMS

Although rip currents are highly variable in both time and space, a description of the mean system is useful in understanding the important characteristics. The process for determining these mean rip properties from video-interpreted drifter tracks is given with a discussion of the accuracy of these methods. It is observed that varying the incident wave conditions produces a range of mean rip current circulation features, which are described in this chapter. The rip features are characterized and quantified using a circulation cell model which facilitates the description of the rip current systems.

3.1 Qualitative Video Observations

Although the video experiments are intended for quantitative analyses, qualitative descriptions of the flow features are useful in characterizing the observed flow features. Video observations indicate that there are three basic rip current patterns: left dominant, right dominant, and meandering systems. This section describes the distinct features observed for each of the three rip system patterns.

3.1.1 Left Dominant Rip Current Systems

A left dominant rip system is characterized by drifters that turn left during most of the video segment after reaching the rip head. Left dominant rip systems are the least common pattern seen throughout this video set. It is noticed in these left dominant systems that the drifters flow through the channel at a sharp angle and form a tight circulation cell over the corner of the left bar. The drifters rarely extend far offshore after

exiting the channel but turn sharply to the left and travel parallel to the shore. Some of these drifters are transported over the bars and re-circulate, while others exit the field-of-view without entering the system again. This pattern fits the observations described of test B in Haller et al. (2002) for the rip current experiments in deeper water.

3.1.2 Right Dominant Rip Current Systems

Right dominant systems occur more frequently in this video set than the left dominant. In these rip systems, drifters exit the channel faster and in a more offshore direction than drifters in the left dominant rips. As the drifter travels far offshore, it eventually slows and turns right. After reaching far offshore, some drifters travel along the side-wall back to shore to be re-circulated in feeder currents. Most drifters, however, are transported past the bridge and out-of-circulation. In general, the right dominant rip systems are the strongest of the three rip current system patterns.

3.1.3 Meandering Rip Current Systems

These rip current systems are classified by rips flopping back and forth between sides. At some instances it seems that the rip is dominant to one side but then it changes directions and is dominant on the other side. The rip may change directions several times throughout a video segment. The drifters in these experiments usually do not extend far offshore; several are eventually transported across the bars and re-circulate through the rip channel.

This type of rip current system is more unsteady than the other patterns. Frequently, pairs of drifters are captured in an eddy and observed to spin around each other. These tight circulations originate around the bar corners, detach, and continue

spinning offshore. It is also noticed that these detached eddies sometimes accompany a change in the dominant circulation direction.

3.2 Methods for Computing Properties from Tracks

The drifter tracks provide some unique measurement capabilities that are difficult to obtain with in situ techniques, such as time-varying spatial descriptions of the large-scale flow patterns. In this section, the methods for computing velocities and wave heights from the drifter tracks are presented. Additional tools such as spatial bin-averaging are also described along with an evaluation of the accuracies of these techniques.

3.2.1 Lagrangian Velocity

The Lagrangian drifter velocity is assumed to consist of three components described by

$$\vec{v} = \vec{v}_c + \vec{v}_w + \vec{v}' \tag{3-1}$$

where $\vec{v}$ is the measured drifter velocity, $\vec{v}_c$ is the current velocity, $\vec{v}_w$ is the velocity due to waves, and v' is the turbulence and noise. The three components of this Lagrangian velocity are assumed to be a function of different time scales. The wave-induced velocity is a function of the frequencies around the incident wave frequency, currents typically vary at a much lower frequency, and the turbulence and noise are assumed to be characterized by higher frequencies.

To isolate the motion due to currents, a low-pass filter is used on the drifter positions to eliminate the wave motion and high frequency turbulence and noise of the drifters. This produces drifter motions associated only with the rip current system. An

ADV velocity time series of waves without currents is used to select the filter cut-off frequency for each experimental wave period. Figure 3.1 shows an energy spectrum of an ADV velocity measured for a 2-second incident period with the frequencies selected for the passed range shaded in cyan. The cut-off frequency is selected to pass all frequencies lower than the incident wave frequency. Table 3.1 gives the selected cut-off frequencies for the low-pass filter for all experimental wave periods. The result of the low-pass filtering can be seen in the track segment shown in Figure 3.2 with the orbital motions removed. The high-frequency motions of the track shown in Figure 3.2 are orbital motions of the drifter and the longer-period isolations are related to the wave group. Lagrangian velocities are obtained using forward differencing of these low-pass filtered drifter tracks.

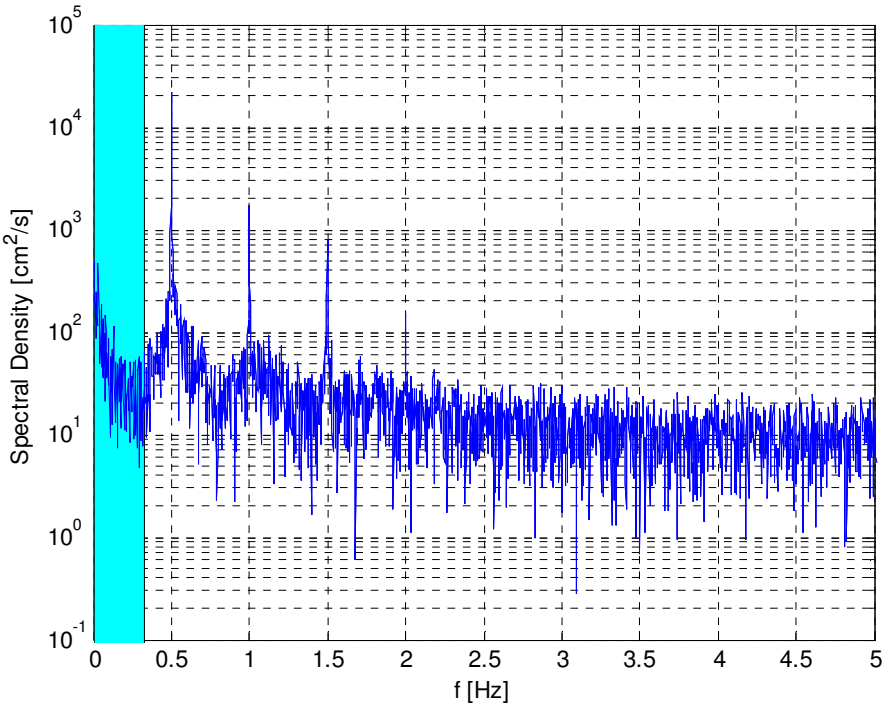

Figure 3.1: Energy spectrum of wave-induced velocity for a 2-second wave showing low-pass filter cut-off of f < 0.33 Hz by the shaded region

Table 3.1: Cut-off frequencies for low-pass filtering of drifter tracks for velocity computation for each experimental wave period

Wave Period (s)	Frequency Cut-off (Hz)
1	0.33
1.33	0.4
1.5	0.4
2	0.33

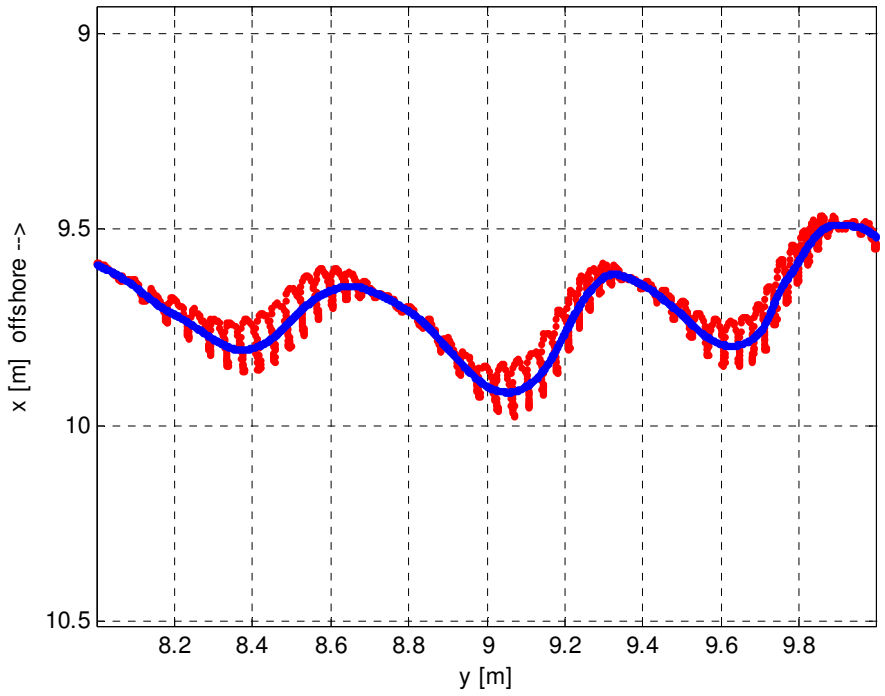

Figure 3.2: Segment of drifter track showing results from low-pass filter (red: raw; blue: low-pass filtered)

3.2.2 Wave Height Estimation

Wave heights are estimated from Linear (Airy) Wave Theory using the orbital motion of the drifter tracks. The orbital motion is the movement associated with the trajectory of a particle induced by a passing wave. As a wave passes, the particle will be displaced forward on the wave crest and backward on the trough along the wave

direction. The amplitude of this back and forth motion can be related to the wave height using any wave theory. Using linear theory, the relationship is described by

$$(x_o, y_o) = \frac{H}{2}\left[\frac{gk}{\sigma^2}\sin(-\sigma t + \delta)(\cos\alpha, \sin\alpha)\right], \tag{3-2}$$

where (x_o, y_o) are the orbital positions, H is the wave height, g is the gravitational acceleration, k is the wavenumber, σ is the intrinsic frequency, t is time, δ is the phase shift, and α is the wave angle.

The orbital position of the drifter tracks are obtained by applying a band-pass filter on the drifter tracks. The purpose of the filtering is to isolate the motion around the incident wave frequency. An ADV velocity time series of waves without current is used to select the filter cut-off frequencies for each experimental wave period. Figure 3.3 shows an energy spectrum of an ADV velocity measured for a 2-second incident period with cyan shading for the frequency range of the band-pass. The low frequency cut-off for the band-pass is the same frequency used as the low-pass filter cut-off in the filtering of drifter tracks for mean current computation. The upper limit is selected to include major harmonics of the incident frequency. Table 3.2 gives the selected upper and lower cut-off frequencies for the band-pass filter for all experimental wave periods. The result of the band-pass filtering for the track segment shown in Figure 3.2 can be seen in Figure 3.4. Notice that the back and forth motions of the drifter orbits are isolated with the band-pass filter.

A complication arises from the vertical motion of a particle on a passing wave. This comes from the fact that the drifter coordinates, during transformation into a real-world coordinate system, are rectified to the planar still water level ($z = 0$). The vertical motions of a drifter, shown in red in Figure 3.5, are translated into apparent horizontal

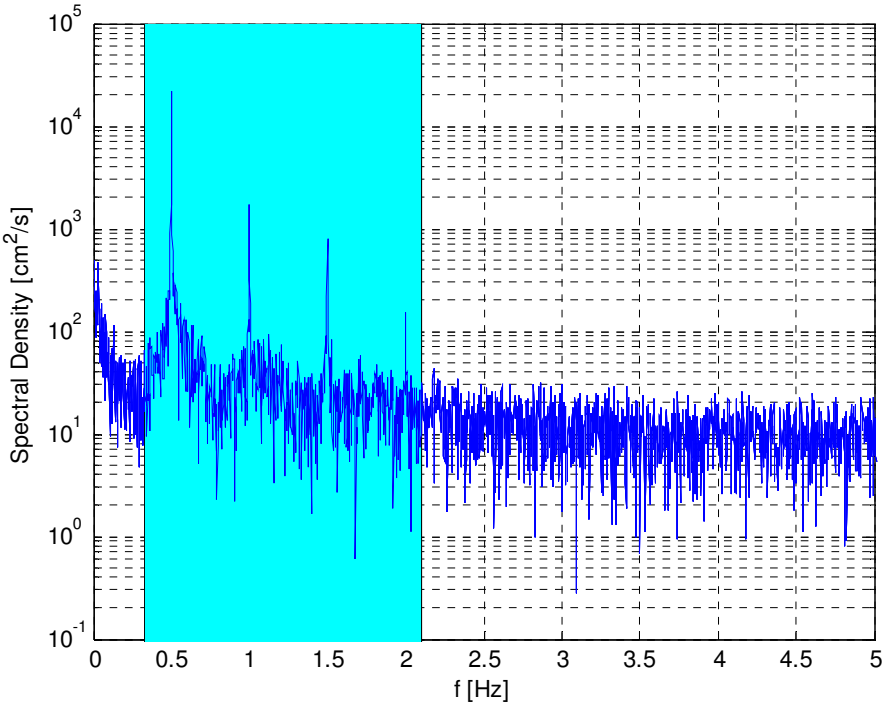

Figure 3.3: Energy spectrum of wave-induced velocity for a 2-second wave showing band-pass filter range of 0.33 Hz < f < 2.1 Hz by the shaded region

Table 3.2: Lower and upper frequency limits for band-pass filtering of drifter tracks for orbital positions for each experimental wave period

Period (s)	Lower Frequency Limit (Hz)	Upper Frequency Limit (Hz)
1	0.33	2.5
1.33	0.4	3.3
1.5	0.4	3.3
2	0.33	2.1

movements, shown in green, when viewed from the video camera. The directions of these apparent motions are in the direction of the camera line of sight as shown in Figure 3.5.

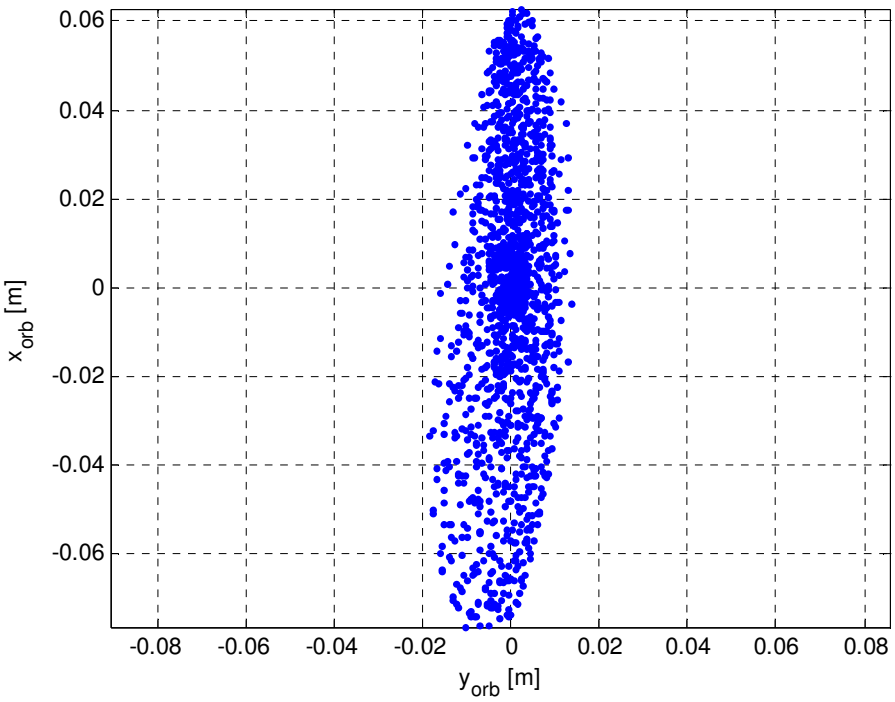

Figure 3.4: Orbital positions of the drifter section shown in Figure 3.2 obtained from band-pass filtering the track

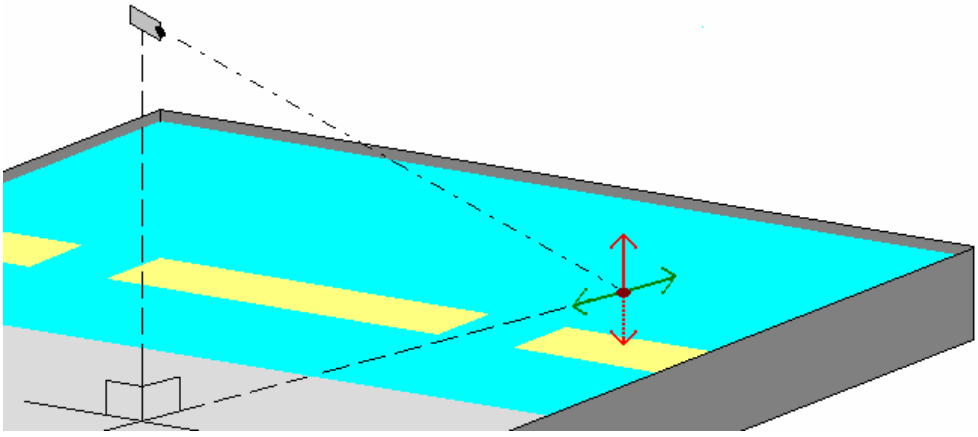

Figure 3.5: Apparent horizontal motion (green) induced along the camera line-of-sight from the vertical motion (red) of a drifter

The apparent positions of a drifter, (x_{app}, y_{app}), can be described at the local free surface elevation, η, using the geometry of the camera line of sight with the drifter by

$$(x_{app}, y_{app}) = (x_0, y_0) - \eta \frac{(x_c - x_0, y_c - y_0)}{z_c}, \tag{3-3}$$

with plan drifter locations, (x_0, y_0), and camera coordinates, (x_c, y_c, z_c).

Combining Equations 3-2 and 3-3 produces a relationship between wave height and the apparent orbital positions of the drifters, (x_{app}, y_{app}). This relationship is given by

$$(x_{app}, y_{app}) = \frac{H}{2}\left[\frac{gk}{\sigma^2}\sin(-\sigma t + \delta)(\cos\alpha, \sin\alpha) - \cos(-\sigma t + \delta)\frac{(x_c - x_0, y_c - y_0)}{z_c}\right]. \tag{3-4}$$

The results from the band-pass filtering provide the apparent orbital positions of the drifters used in Equation 3-4.

The parameters necessary to estimate the wave height are determined on a wave-by-wave basis. A zero up-crossing of the band-pass filtered positions is used to separate the drifter tracks into individual waves. The low-pass filtered drifter positions are averaged over each zero up-crossing to determine a single coordinate for each wave. Because these are Lagrangian tracks, the intrinsic frequency for each wave is determined directly from the zero up-crossing time series. Using the known water depth, *h*, at the wave position and the intrinsic frequency, the wavenumber is calculated using the linear dispersion relationship from theory given by

$$\sigma^2 = gk \tanh kh\,. \tag{3-5}$$

From the orbital positions, $\overline{x_{app}{}^2}$ and $\overline{x_{app} \cdot y_{app}}$ are computed for each wave, where the over-bar denotes a time average over a zero up-crossing wave period. Equation 3-4 is then written as

$$\overline{x_{app}{}^2} = \frac{1}{2}\left(\frac{H}{2}\right)^2\left[\left(\frac{gk\cos\alpha}{\sigma^2}\right)^2 + \left(\frac{x_c - x_0}{z_c}\right)^2\right] \tag{3-6}$$

$$\overline{x_{app} \cdot y_{app}} = \frac{1}{2}\left(\frac{H}{2}\right)^2\left[\left(\frac{gk}{\sigma^2}\right)^2 \cos\alpha \sin\alpha + \frac{(x_c - x_0)\cdot(y_c - y_0)}{z_c{}^2}\right], \tag{3-7}$$

which can be solved simultaneously for the wave height and direction.

3.2.3 Bin-Averaging

To determine spatial variations in the time-averaged rip properties, bin-averaging is used. The process involves averaging the measurements obtained from the drifters that pass a selected area over a given time. Circular bins are the shape predominately used for bin-averaging analyses unless otherwise noted. At any moment the bin may be empty or may contain multiple particles. Each time step that at least one drifter is in the bin is given equal weight in the time and spatial averaging. The bin-averaged property is attributed to the center of the bin area.

3.3 Accuracy of Properties Computed from Drifter Tracks

The accuracy of the wave properties obtained from the drifter tracks is evaluated by comparing mean properties from in situ measurements and the tracks. There are two types of comparisons performed for these experiments: 1) flume experiments with simultaneous drifters and ADV measurements; and 2) wave basin experiments with

comparisons between different tests of the same incident wave conditions, one with in situ instruments only and the other with drifter tracking only.

3.3.1 Accuracy Assessment of Flume Tests

The flume experiments, performed by Kevin Haas, consist of six tests in a flume: two with mean currents without waves and four with waves only. Four ADV's are arranged as shown by the red squares in Figure 3.6. Drifters are placed into the flume and digitally captured with the same video setup as the basin experiments. The drifter tracking and coordinate transformation into a real-world system are the same as the basin experiments but on a smaller scale.

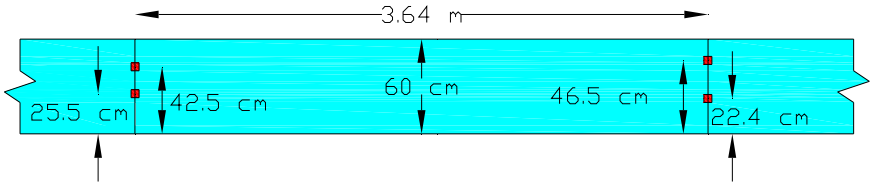

Figure 3.6: Flume set-up for experiment of flow fidelity with positions of ADV's (red squares)

For the experiments without waves, the ability of the drifter to follow a mean current is tested. The low-pass filtered mean velocity from the ADV's is compared with the mean velocity obtained from the low-pass filtered drifter tracks with cut-off frequency of 0.05 Hz. Table 3.3 lists the errors from the experiments.

The errors in mean velocity from the drifter tracks do not exceed 1 cm/s and over-predict the ADV mean in both cases. Standard deviations of velocity are also significantly higher for the drifter measurement, indicating a lower precision for the

drifter measurement technique. Overall, the average percent error in the drifter tracking technique for mean velocity measurement is 2.0%. Sources of errors in the velocity measurements using drifter tracks are discussed in Section 3.3.3.

Table 3.3: Mean velocity comparisons between drifter and ADV from flume experiments with mean currents (low-pass filtered with frequency cut-off of 0.05 Hz)

Test	Flow	Measurement	Mean Velocity (cm/s)	Error Magnitude (cm/s)	Percent Error	Standard Deviation (cm/s)
J1	Strong	ADV	38.25	0.35	0.9%	0.67
		Drifter	38.61			1.99
J2	Weak	ADV	14.87	0.36	2.4%	0.46
		Drifter	15.23			1.09

The tests of waves without current evaluate the ability of a drifter to follow an orbital trajectory used to compute the wave height. Wave heights are computed from ADV's from the orbital velocities using a Linear (Airy) Wave Theory relationship given by

$$\overline{u^2} = \frac{H^2}{4}\sigma^2\left[\frac{\cosh k(h+z)}{\sinh kh}\right]^2, \tag{3-8}$$

where u is the time-averaged measured horizontal velocity component, H is the wave height, σ is the intrinsic frequency, k is the wavenumber, h is the local water depth, z is the vertical coordinate. The mean wave height obtained from drifters is computed using the Lagrangian orbital positions and Equations 3-6 and 3-7 given previously. Table 3.4 lists the errors from these experiments.

The mean wave height measurements from the drifter tracks indicate errors ranging from 3.0 – 17.3%. The 1 and 1.33-second waves produce much less error than

the 1.5 and 2-second waves. The wave height also appears to be important for the measurement accuracy drifters; for similar periods of 1.33 and 1.5 seconds the larger wave height produced less error. Except in test J6, with a wave period of 2 seconds, the drifter technique over-predicts the wave height reported from the ADV. A discussion of the sources of errors in the wave height estimation using drifter tracks is given in Section 3.3.3.

Table 3.4: Mean wave height comparisons between drifter and ADV from flume experiments with monochromatic waves

Test	Period (s)	Measurement	Wave Height (cm)	Error Magnitude (cm)	Percent Error
J3	1	ADV	2.39	0.09	3.9%
		Drifter	2.29		
J4	1.33	ADV	7.82	0.23	3.0%
		Drifter	7.58		
J5	1.5	ADV	4.52	0.78	17.3%
		Drifter	3.74		
J6	2	ADV	1.77	0.26	14.9%
		Drifter	2.04		

3.3.2 Accuracy Assessment of Basin Tests

All optical experiments in the wave basin have at least one corresponding in situ experiment with the same incident wave condition. For these tests, comparisons are made for mean velocity and wave height calculations using bin-averages at the instrument locations.

Stokes drift corrections are applied to the instrument mean current measurements so that velocity comparisons can be made between the two methods. The stokes drift

velocity correction, (u_s, v_s), is computed using wave properties from the band-pass filtered orbital velocities of the ADV's, (u_{orb}, v_{orb}), with the equation given by

$$(u_s, v_s) = \frac{gH^2k^2}{\sigma \tanh(2kh)} \cdot (\cos\alpha, \sin\alpha), \tag{3-9}$$

with the wave angle computed as

$$\alpha = \tfrac{1}{2} \tan^{-1}\left(\frac{2\overline{u_{orb} \cdot v_{orb}}}{\overline{u_{orb}^2} - \overline{v_{orb}^2}} \right), \tag{3-10}$$

where g is gravitational acceleration, H is wave height computed with Equation 3-8, σ is the intrinsic frequency, k is the wavenumber, h is the local water depth, and the over-bar indicates a time-average over the entire experiment.

The mean velocity comparisons are done in groups according to location. For regions in the channel where the feeder currents converge and turn offshore, the longshore and cross-shore velocity components are both significant and therefore comparisons are made using the mean velocity magnitude. The longshore velocity component alone is considered for instruments in the trough behind the bars in the feeders since the cross-shore velocity is insignificant.

Bin-averaging of sporadic drifter track measurements in a time-varying flow field creates accuracy issues not seen in the flume comparisons. For regions of the basin with spatially-variant flows, such as the converging point of the feeder currents, large bin sizes create critical errors by including flow features that are non-typical of the bin center into the average. Also, regions with minimal drifter coverage are susceptible to errors in mean measurements. If only a few drifters pass through a particular bin during an experiment, the drifter mean measurement may not be representative of the actual mean.

To address the spatial-variation and coverage issues for mean track measurements, variable bin sizes are used. The bin radius for the bin-averaging varies based on the amount of flow variation and drifter coverage for each region. Shown in Figure 3.7, is the spatial variation of the drifter coverage by percentage of time. Notice that the trough is the least covered area throughout the basin. The selection of bin radii is determined by testing several sizes to determine the size of optimum error. The turn of the feeders offshore in the rip is a highly variant area, both temporally and spatially; small bins of 20 cm radius are determined to be optimum in this convergent area. Since the rip is usually directed offshore, the spatial variability is slightly less critical than the converging feeder currents. The optimization results in a radius of 30 cm giving the lowest errors in the rip vicinity. A large 60 cm radius bin is found to be optimal for areas in the trough behind the bars since there is low drifter coverage and much less spatial variability in these areas. The bin sizes are illustrated in Figure 3.8 at the instrument locations for set H.

Figure 3.9 shows the rip speed comparisons between the video and the instruments for each ADV in the channel. It is evident that there is much variability, but the video over-predicts the mean current measurements from the instrument in most cases. This over-prediction for the mean track measurements is explained by the non-randomness at which the drifters flow through certain bins. Drifters thrown into the feeders or rip will typically follow the side of dominant circulation when exiting the rip. Although the tossing of the drifters is intended to be fairly uniformly distributed, more drifters may pass through a particular bin when the circulation is dominant on the side of that bin. This non-randomness gives a biased mean since measurements during weak periods are

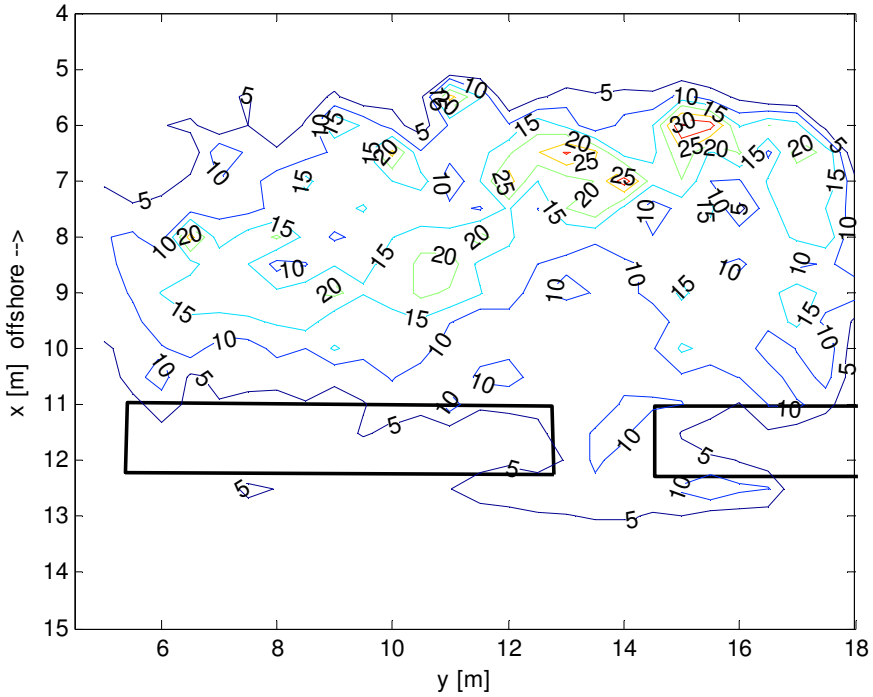

Figure 3.7: Spatial variation of the percentage of time a drifter is in a circular bin of 0.25 radius (I6)

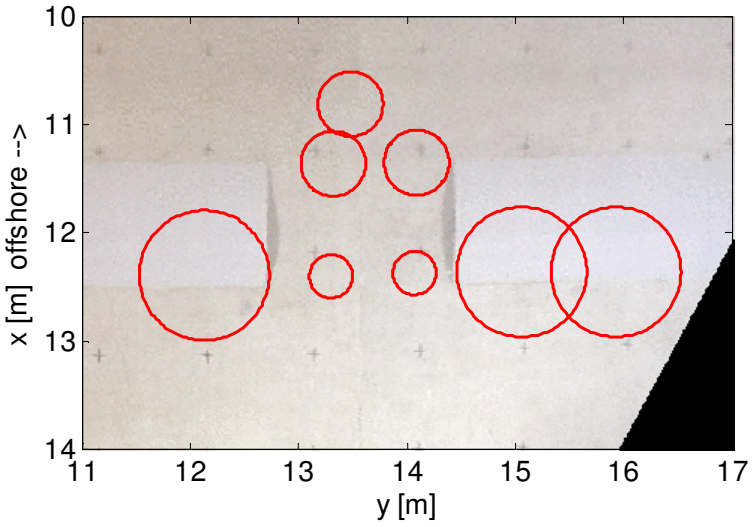

Figure 3.8: Various bin sizes for different regions (large bins in trough – 60 cm radius, medium bins for rip – 30 cm, small bins at turn of feeders offshore – 20 cm)

much less frequent. For instance, drifters tossed in feeders will pass through the channel primarily when the rip current is strong, thus periods of weak flow in the channel are not measured.

Shown in Figure 3.10 is the comparison between the video and instrument measurements of the turning currents. There is much less scatter in the turning current comparison than in the rip comparisons. In this case, however, the video measurements appear to under-predict the instrument measurements.

The feeder current comparisons are shown in Figure 3.11 for each ADV in the trough. It is apparent that the video measurements agree quite well with the instrument measurements.

The wave height calculations have weaker spatial variations in the flow and therefore all regions are weighted equally; a bin radius of 40 cm is used for all regions. Comparisons of wave height are made with both ADV and wave gauge instruments. Wave heights from the ADV's are computed in the same way as in the flume experiments. For the wave gauges, individual waves are determined using a zero up-crossing method on the band-pass filtered water level time series. The band-pass filter is the same as is used when determining the orbital positions from the video. Wave heights are calculated by computing the difference between the max and min water levels for each wave and then averaged for a mean wave height. Figure 3.12 shows the wave height comparisons for all experiments.

The average and percent error over all the cases for the rip, feeder, and turning currents along with the wave heights are given in Table 3.5. The video measurements of the turning currents and wave heights are the most accurate of the rip system properties.

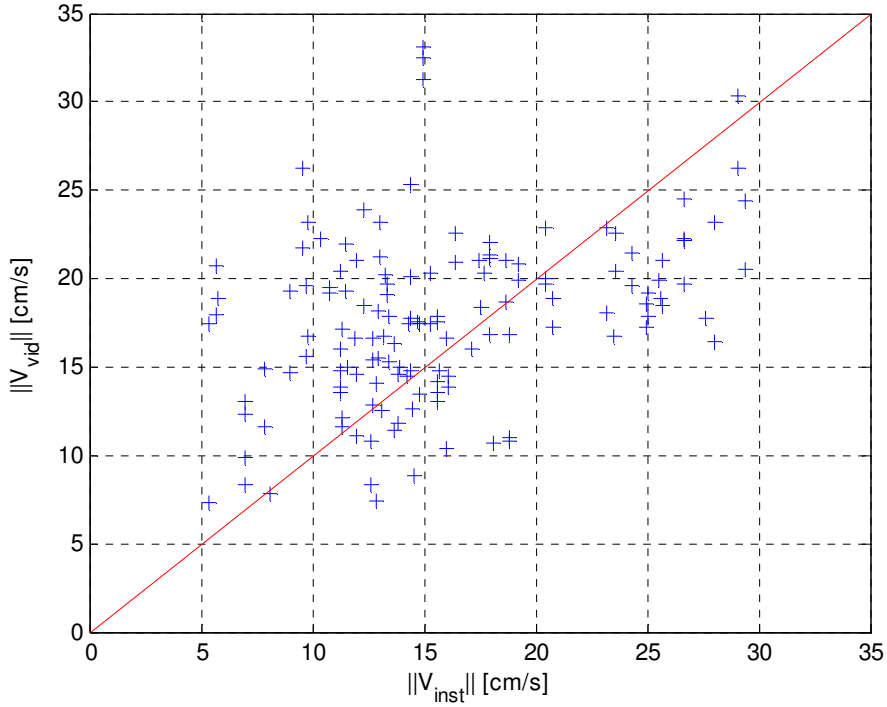

Figure 3.9: Rip mean velocity comparison showing measurements from video on y-axis and instruments on x-axis with line of perfect agreement

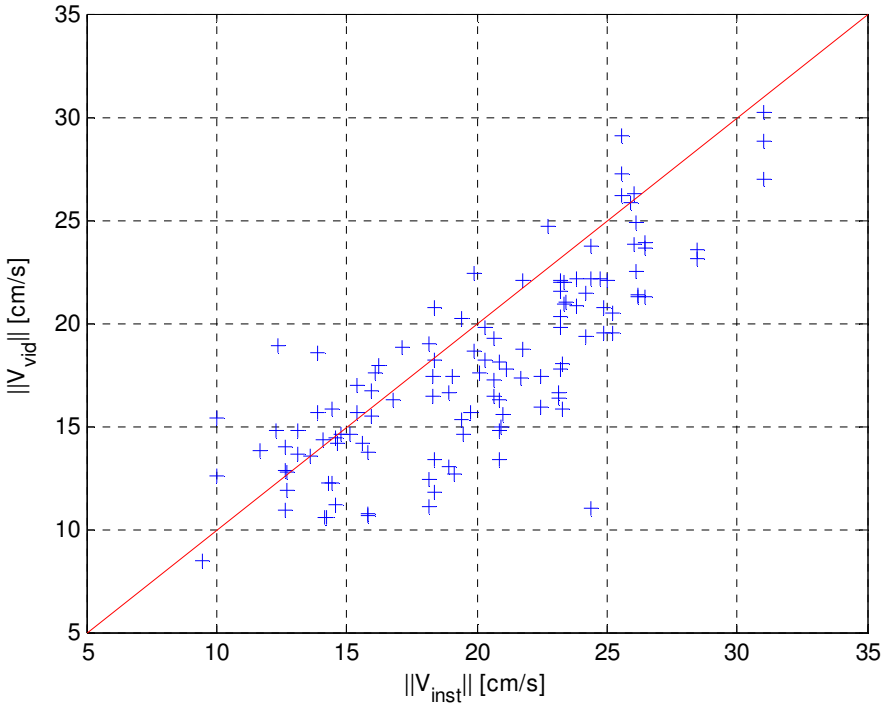

Figure 3.10: Turning current comparison showing measurements from video on y-axis and instruments on x-axis with line of perfect agreement

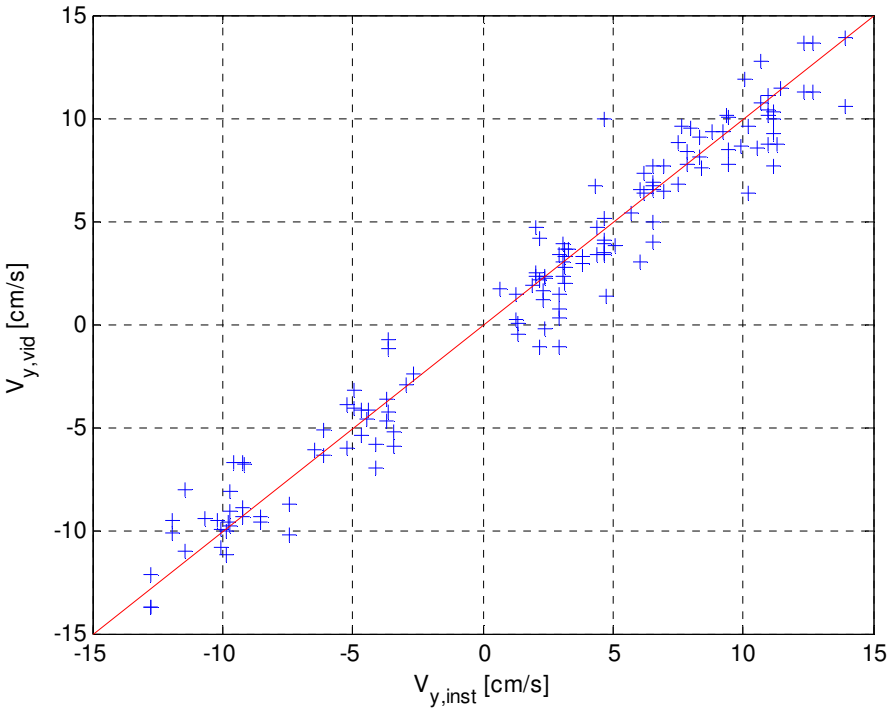

Figure 3.11: Feeder velocity comparison showing measurements from video on y-axis and instruments on x-axis with line of perfect agreement

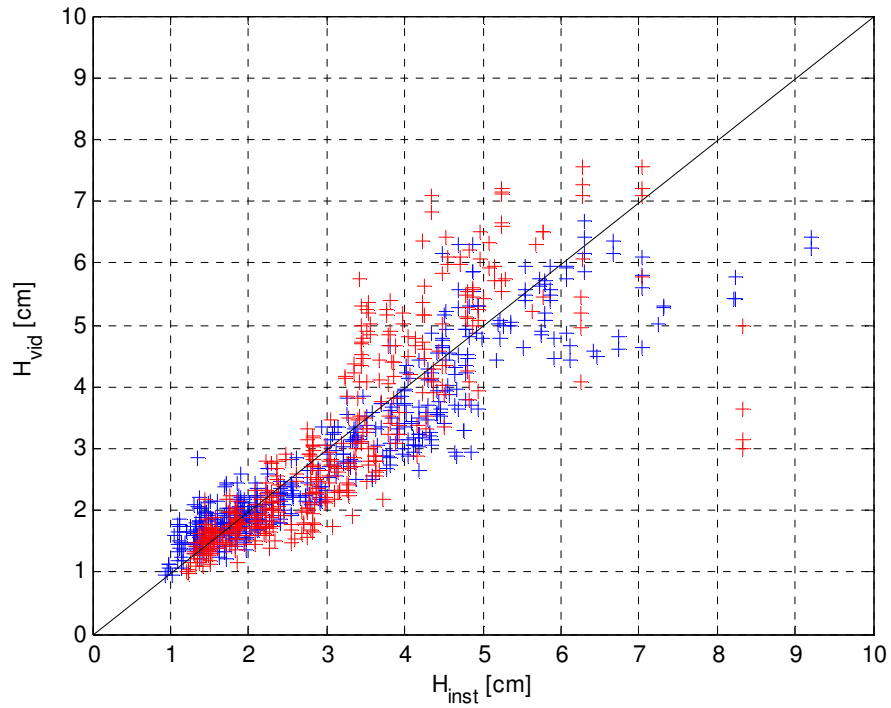

Figure 3.12: Wave height comparison showing measurements from video on y-axis and instruments on x-axis with line of perfect agreement (red – ADV, blue – wave gauges)

Measurements of the rip current, however, appear to produce the largest errors of any video measurement. The errors in the rip current are most likely due to the spatial variability of the rip current whereas the errors in the feeder currents are more likely caused from drifter coverage issues.

Table 3.5: Average errors for velocity comparisons over every experimental run

	Turning Currents	**Rip Currents**	**Feeder Currents**	**Wave Heights**
Bin Radius	20 cm	30 cm	60 cm	40 cm
MSE	3.52 cm/s	5.70 cm/s	1.36 cm/s	0.82 cm
% Error	15.38%	39.36%	25.04%	15.85%

3.3.3 Sources of Measurement Errors

Aside from the errors associated with bin-averaging, sources of measurement errors using the drifter tracks include depth variations, flow fidelity of the drifters, surfing, and reflection. Each of the error sources has unique effects on the velocity and wave height measurements obtained using the drifter tracks.

Depth variations in the flume are associated with boundary-layer effects, while rip current systems in a basin are known to have a vertical structure offshore (Haas and Svendsen 2002). Depth variations in the current would be evident as an over-prediction of the drifter measurements relative to the ADV, since the surface drifters are 1 – 2 cm below the water surface and the ADV measurements are deeper (8 – 10 cm in flume, 5 – 6 cm in basin). In the flume velocity comparisons, an over-prediction from the drifter measurements is noticed and can be explained by a boundary layer effect. In the basin velocity comparisons, an over-prediction from the drifter tracks is evident in the rip

current but not in the feeder or turning currents. Since the rip current has more depth variation than the trough, the general over-prediction in the rip current comparisons can be explained by the difference in measurement depths between the drifters and ADV's. Since the trough is fairly depth-uniform, the feeder and turning currents are less influenced by the difference in measurement depths.

The drifter size, although larger than typical optical measurement drifters, is relatively small compared to the measured flow features. For velocity measurements, a typical circulation cell can range from 1 – 3 m in radius, approximately 20 – 50 times larger than the radius of a drifter. In estimating the wave heights, the size of the waves compared with the drifter is important. For shallow basin regions with a depth of 10 cm and a wave period of 1 s, the wavelength is 8.2 times the diameter of a drifter. For larger depths of 40 cm and a wave period of 2 s, the wavelength can exceed 30 times the size of the drifter, which indicates that several drifters can exist in a single wavelength. The amplitudes of the drifter orbits are used to estimate the wave height using linear wave theory. For a 1-s wave at a shallow depth of 10 cm, the amplitude of an orbit is 1.7 times the wave amplitude. For a larger depth of 40 cm and a wave period of 2 s, the wave-orbital amplitude can exceed 4.2 times the wave amplitude. Therefore, for small wave heights in shallow depths, a drifter radius (5.65 cm) may be slightly larger than the amplitude of the orbital motion. For most test conditions, the wave-orbital amplitude is on the same order as the length of a drifter radius or less. It is expected that the drifters follow the large-scale flow features better than the smaller-scaled wave heights.

Another error not evident in the flume comparisons is surfing effects. It is visually observed in the video experiments that drifters can surf on breaking waves.

When surfing, a drifter will travel at the wave celerity speed, much faster than the current. Therefore, wave breaking regions are more susceptible to errors in the mean optical measurements from drifter surfing and, due to the difficulty of quantifying the surfing, no corrections are applied.

Wave reflection is also a source of error in the video measurements of wave height. The procedure for estimating the wave heights assume no reflected waves, which is largely true in the wave basin. Estimates of the maximum possible error in wave height estimates are calculated theoretically for a directly overhead view with normal incident waves at the partial nodes and partial antinodes to be 10% (5% RMS error) for a reflection coefficient of 0.05.

3.4 Circulation Cells

Characterizing and quantifying the mean rip current circulation cells provides a way to analyze rip systems driven by different wave conditions. This section presents observations from the mean rip current circulation cells and generalizes a model fit for the cells.

3.4.1 Characteristics of Circulation Cells

The general characteristics of circulation cells are determined from the drifter track mean velocity field. The circulation patterns in some tests show that the left and right cells were nearly equal in strength while others have a clear dominant circulation cell. To categorize these circulation cells, a model is developed to describe the general behavior. As qualitatively described at the beginning of the chapter, Figure 3.13 shows that the left currents turn sharply and do not reach far offshore. It is also apparent from

Figure 3.14 that the right-biased rip current extends far offshore with a much larger circulation cell. From the qualitative descriptions of the video, the meandering rip currents are characterized as unsteady systems with eddy shedding. Even with the unsteadiness and meandering, Figure 3.15 appears to indicate that both sides are even in the mean velocity field.

The center of circulation is needed to find the circumferential velocities in a cell. The process for finding the centers includes searching for a location that has a minimum mean velocity and which produces a circumferential velocity magnitude that radially increases in all directions. A MATLAB code is used to locate a point from an initial guess that best matches these requirements. The determined center of circulation is used to calculate the circumferential velocity field of a circulation cell. Cartesian velocities around a circulation cell (blue) with the corresponding circumferential velocities (red) calculated using the determined center of circulation are shown in Figure 3.16.

The radial dependence of the circumferential velocity is found by averaging around the circulation cell for varying distances from the center. The left plot of Figure 3.17 shows velocity profiles non-dimensionalized by the maximum velocity for all circulation cells on both sides throughout all experimental runs. The right plot shows the general trend of all the circulation cells. This trend line is calculated by averaging the data for each radius and then smoothing the averaged profile using a quadratic 5-point moving average. It is evident that the velocity radially increases to a point and then decreases. Generally, there is one dominant peak in velocity but a few profiles show multiple velocity peaks near the same magnitude. The two-peak profiles may be

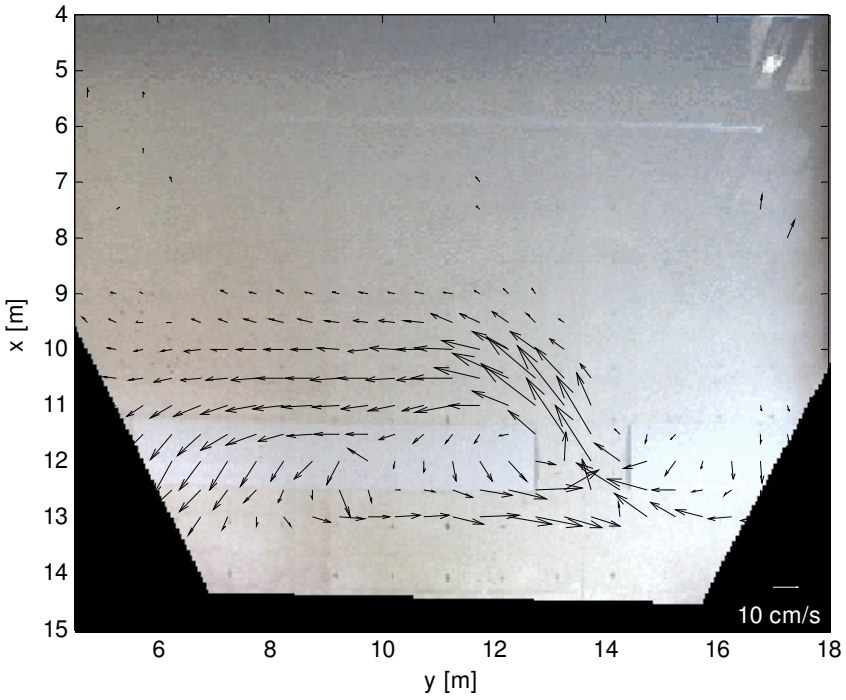

Figure 3.13: Mean vector field for a left-dominant circulation system – I1 (T = 2 s, a = 2.5 cm, monochromatic) using 0.5-m radius bins

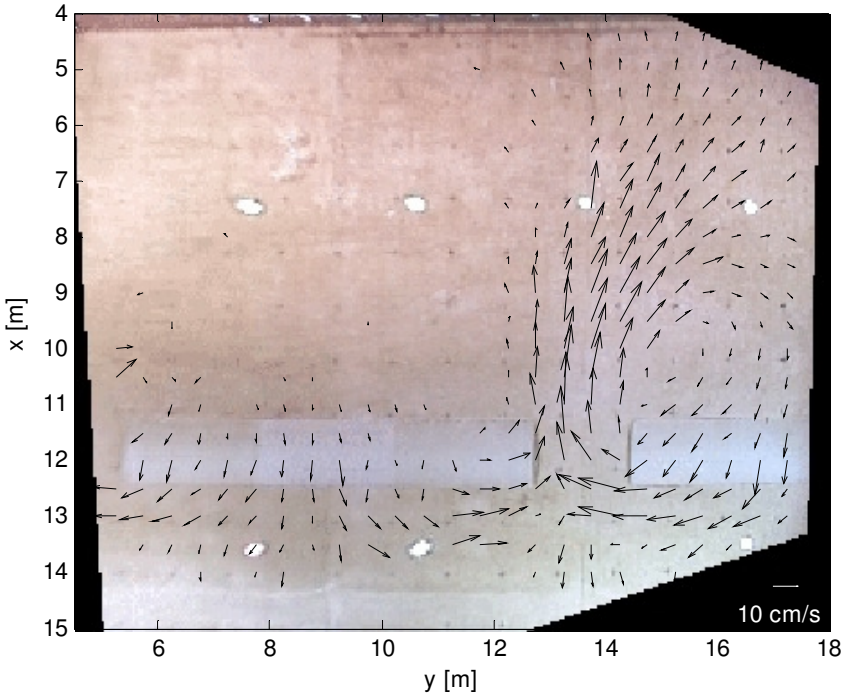

Figure 3.14: Mean vector field for a right-dominant circulation system – G8 (T = 1.33 s, a = 3 cm, T_G = 64 s) using 0.5-m radius bins

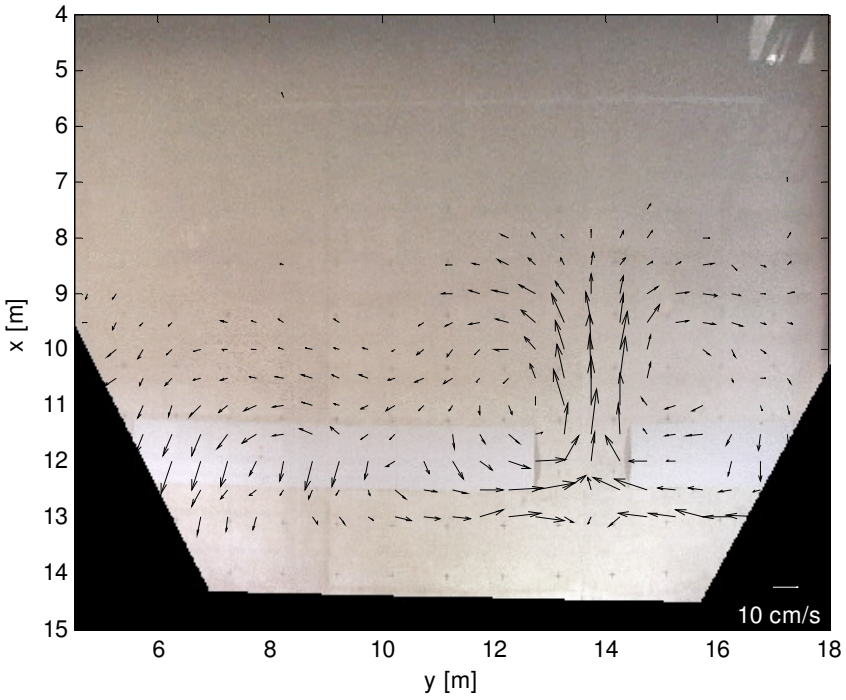

Figure 3.15: Mean vector field for a symmetric circulation system – I6 (T = 2 s, a = 2.5 cm, T_G = 32 s) using 0.5-m radius bins

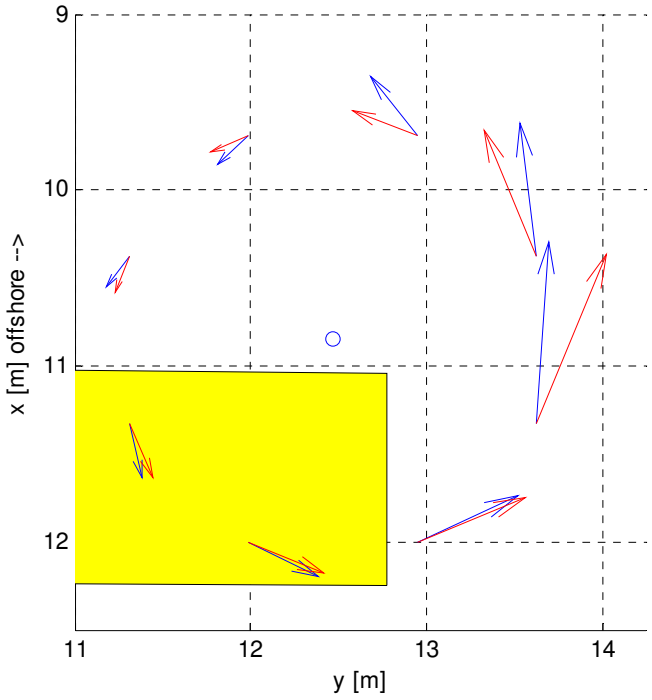

Figure 3.16: Cartesian velocity vectors (blue) around a circulation cell with corresponding circumferential velocity vectors (red)

explained by a circulation cell inside a more dominant cell. For modeling purposes, the focus is on the dominant single peak velocity trend. The decrease from the velocity peak outward behaves similar to an exponential decay. The increase in the inner core of the circulation is more difficult to determine; it does not appear to be linear in all cases.

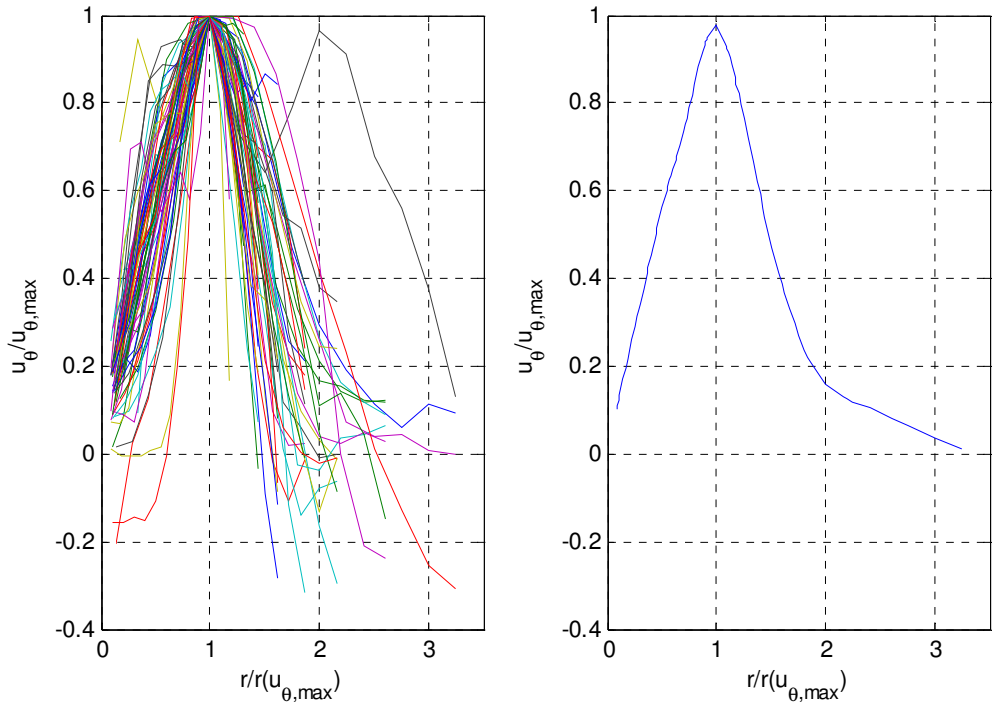

Figure 3.17: Non-dimensional average circumferential velocity profiles showing the radial dependence of circulation cells for all tests (left) and smoothed average (right)

The model derived to describe the radial dependence of the circumferential velocity, U_θ, in a circulation cell is given by

$$U_\theta = \begin{cases} -a(\theta)\cdot\left[(1-R)^{p\cdot a_{\max}/a(\theta)} - 1\right], R \le 1 \\ a(\theta)\cdot\exp\left[-(R-1)^n / w(\theta)\right], R > 1 \end{cases}, \qquad (3\text{-}11)$$

where R is the radius non-dimensionalized by the radius of peak velocity, $a(\theta)$ is the velocity magnitude for a given angle, $a_{\max}$ is the absolute maximum velocity magnitude around the cell, p is a power factor that controls the shape of the inner core profile, n is a power factor that controls the descent rate of the outer core, and $w(\theta)$ is a width factor that is related to the circumferential width variations around the cell. The model is derived such that $\frac{\partial U_\theta}{\partial R}$ is zero at the transition for n and p greater than two and the slope is continuous through the center of the cell.

Circumferential variations around the circulation cell are analyzed by bin-averaging along the radius of peak velocity. The left plot of Figure 3.18 shows the circumferential variations in circumferential velocity for the peak radius in every experiment case. The average velocity around the radius is subtracted from each circumferential velocity and then normalized by the velocity range. The location of the maximum velocity is also shifted such that it occurs at zero. By averaging the non-dimensional measurements of the circumferential dependence and then smoothing the profile using a 5-point moving average, it is observed that the variation of velocity strength around the circle behaves similar to a cosine function as shown in the right plot of Figure 3.18.

Other observations of the circulation cell measurements show that the radial location of the velocity peak appears to be fairly uniform around the cell. Also, the narrowness of the velocity profile appears to be proportional to the strength of the velocity; as the velocity in the circulation cell is stronger the profile becomes narrower.

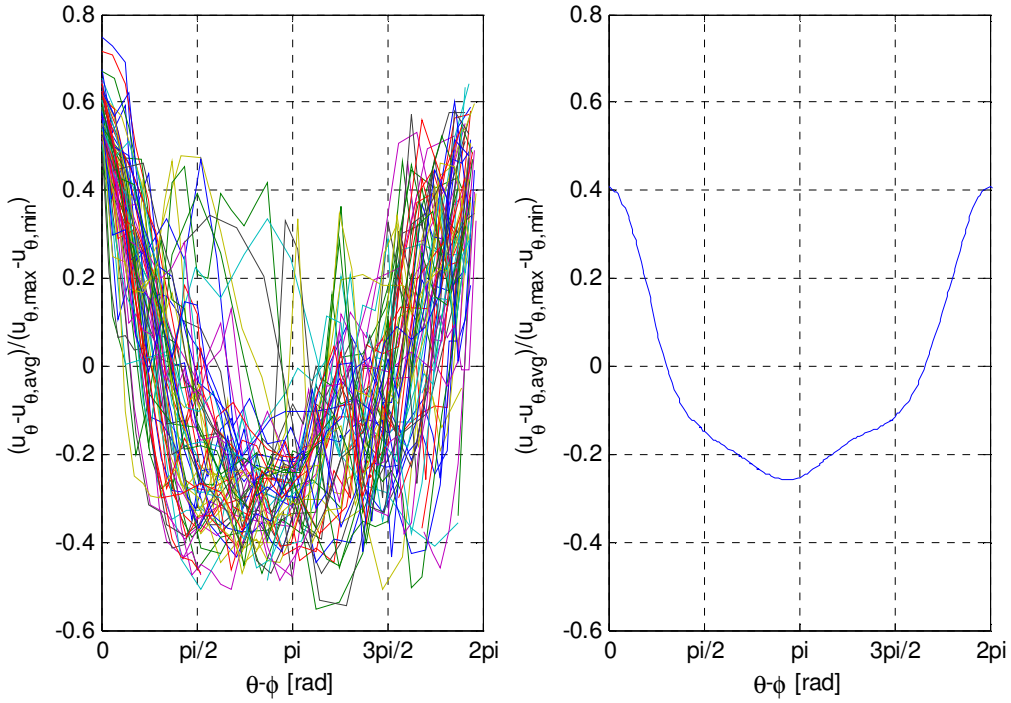

Figure 3.18: Non-dimensional circumferential velocity profiles around a radius of peak velocity showing the circumferential dependence of circulation cell for all tests (left) and smoothed average (right)

A cosine function with a phase shift is selected to model the general circumferential dependency of velocity in the circulation cells by the equations

$$a(\theta) = \frac{a_{\max} + a_{\min}}{2} + \frac{a_{\max} - a_{\min}}{2}\cos(\theta + \phi) \tag{3-12}$$

$$w(\theta) = \frac{A + B}{2} + \frac{A - B}{2}\cos(\theta + \phi), \tag{3-13}$$

where a is the velocity magnitude that varies from $a_{\min}$ to $a_{\max}$, θ is the circumferential angle around the cell, ϕ is the phase shift, and w is the width factor that varies from A to B. A should be less than B so that the cell is narrow at the velocity peak and wider in the lull.

The circulation cell model is fit to the data using two optimization parameters: the mean squared error of the circumferential velocity and the mean squared error of the circulation. Both of these factors are important to the quality of the model fit and are used to define an optimization parameter (E) given by

$$E = 0.5 \cdot \left(2\pi R_{core}\right) \cdot E_v + 0.5 \cdot E_\Gamma, \tag{3-14}$$

where E_v is the mean squared error of the velocity, E_Γ is the mean squared error of the circulation, and R_{core} is the radius of transition between the two functions of the model. The velocity (left) and circulation profiles (right) for the model fit are shown with the measured data in Figure 3.19. Notice that the model velocity does not reach the maximum velocity but fits the overall trend as shown in the circulation fit. Figure 3.20 shows the full modeled circulation cell for the left cell of I6 with a strong narrow current on one side and a weak and broad current on the other side.

3.5 Mean Rip Current System Properties under Various Wave Conditions

The wave amplitude, period, group period, and the amplitude ratio of the bi-chromatic group components are the four parameters varied in these experiments. The variation of these four parameters produces a wide variety of mean circulation patterns. The in situ and video measurements as well as a circulation cell model are used to characterize the variation of the rip current systems for the tests.

3.5.1 Localized Rip System Properties

This section discusses the effect of the wave height on the individual elements of the rip current system including setup, pressure gradients, and currents. For comparisons,

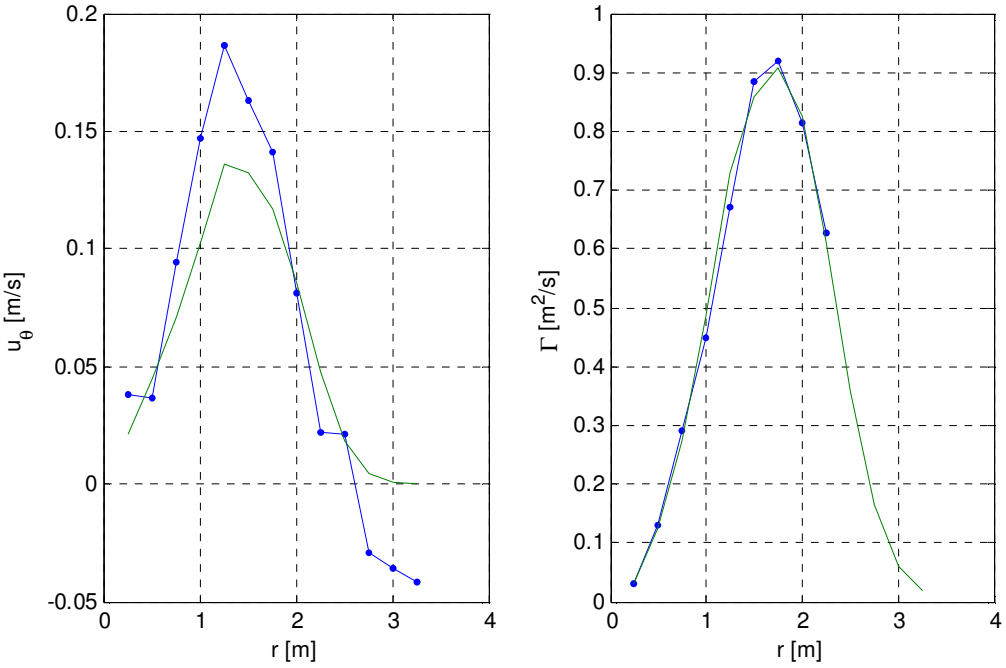

Figure 3.19: Model fit (green) of velocity profile through rip channel (left) and circulation profile (right) for the left circulation cell of I6 compared with measurements (blue)

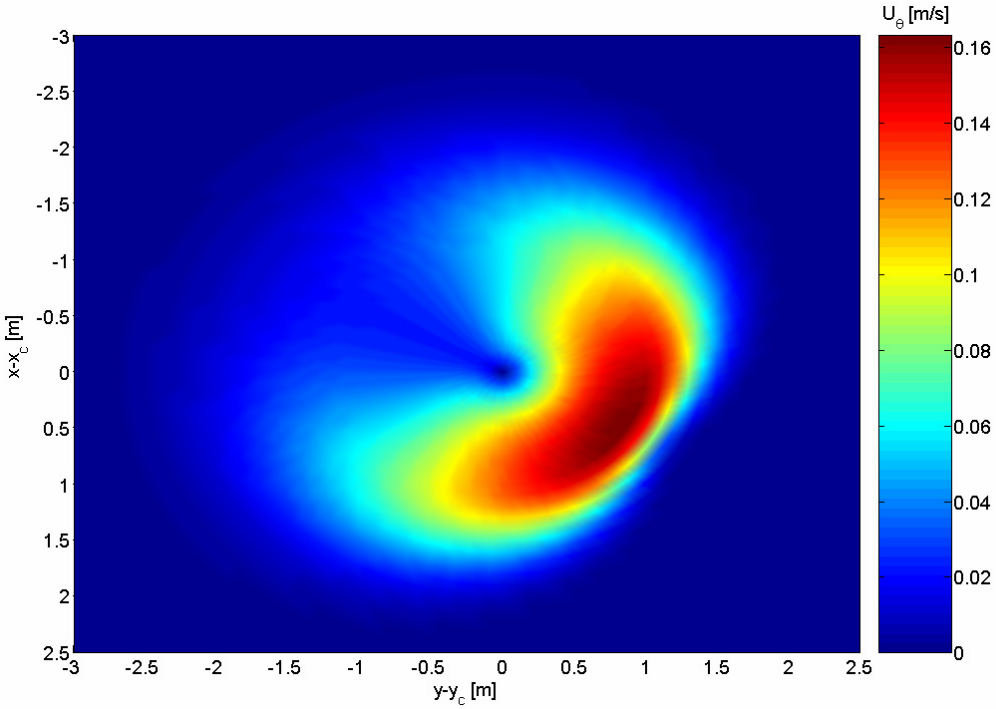

Figure 3.20: Circulation cell calibrated to fit left cell of I6 (offshore is up)

the offshore wave height is determined using a zero-up crossing method on the offshore wave gauge data.

The setup is measured from the wave gauges in the trough by time-averaging the water level data. Figure 3.21 shows the measured setup from the wave gauge approximately 2 m from the center of the channel plotted against the mean offshore wave height. The wave setup clearly increases with increasing wave height.

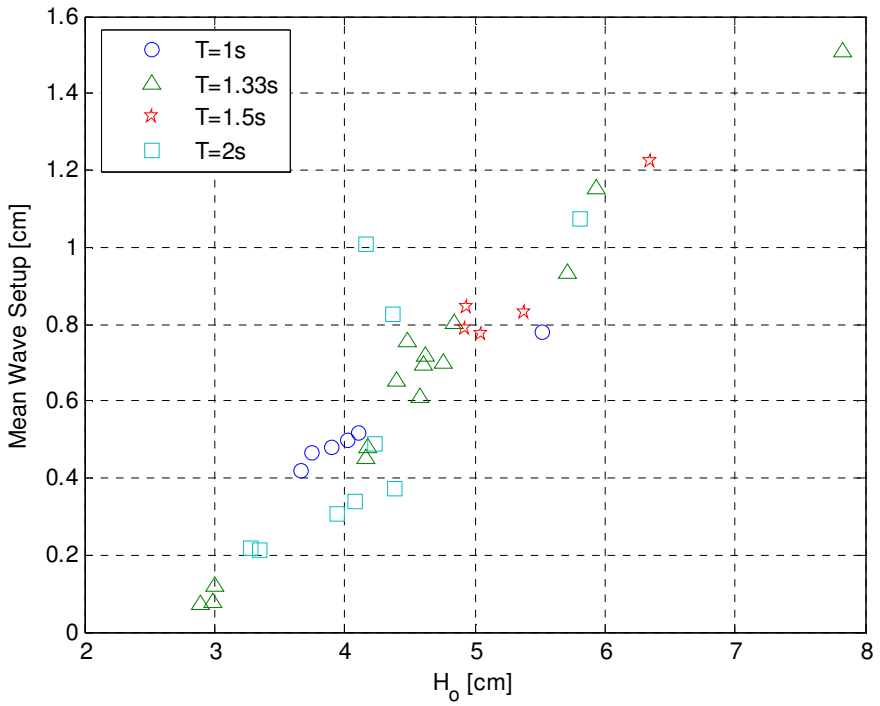

Figure 3.21: Effect of mean offshore wave height on the setup in the trough at $x = 12.33$ m and $y = 11.76$ m (series H) and $x = 12.30$ m and $y = 11.40$ m (series F)

Since the wave setup increases with increasing wave height, it is expected that the longshore pressure gradient would also increase for bigger waves. The mean longshore pressure gradient (*LPG*) is calculated from two wave gauges, one in the corner of the bar and the other 1 m away from the corner, with the equation given by

$$LPG = g\left(h + \frac{(\overline{\eta}_{i+1} + \overline{\eta}_i)}{2} \right)\left[\frac{\overline{\eta}_{i+1} - \overline{\eta}_i}{y_{i+1} - y_i} \right], \tag{3-15}$$

where g is the acceleration due to gravity, h is the still water depth at the center of the two gauges, and $\overline{\eta}$ is the local surface elevation at the two longshore positions given by y_i and y_{i+1}. The mean longshore pressure gradients on the dominant circulation side, grouped by wave period, are shown in the left side of Figure 3.22 as a function of the offshore mean wave height. There are only a few tests for comparison since the right feeder, which was often the dominant side, was not instrumented in the F tests. Unexpectedly, the longshore pressure gradients do not increase with increasing wave height and there is much variability. Notice that the 1-s waves generally have a much lower pressure gradient than the tests of other wave period. A test with a 2-s wave period, F19, is the exception that produces the lowest pressure gradient. The lack of increasing longshore pressure gradients for the dominant circulation side makes conclusions on the effect of increasing wave height difficult to make. The right plot of Figure 3.22 shows the mean longshore pressure gradients for the side of weak circulation. Like the dominant circulation side, there is much variability in the relationship between wave height and longshore pressure gradient, however the longshore pressure gradient does seem to decrease with increasing wave height. Notice that the tests with 2-s wave periods tend to have stronger pressure gradients than the other tests for both the dominant and weak sides of circulation.

The longshore pressure gradients drive feeder currents toward the rip channel. An increase in longshore pressure gradient should produce an increase in the feeder current, regardless if it is the side of dominant circulation. The feeder current is calculated by

averaging the longshore velocity of an ADV between the two wave gauges used in computing the pressure gradient. The mean feeder current is plotted against the longshore pressure gradient in Figure 3.23 for both dominant and weak circulation sides. The general trend is indeed that stronger pressure gradients produce an increase in feeder currents. Interestingly, the tests with 2-s waves have a larger variability in pressure gradients for similar feeder strengths, which is not seen in the other tests. Also, the 2-s waves generally produce the largest feeder currents with the exception of F9 which has the weakest feeder current.

Since the longshore pressure gradient does not appear to increase with wave height and the feeder currents increase with the pressure gradient, bigger waves may not produce strong feeder currents. The mean feeder current is plotted against the mean offshore wave height in the left plot of Figure 3.24 for the side of dominant circulation and the right plot of Figure 3.24 for the weak side. Notice feeder currents on the side of dominant circulation side, although with much variability, show an increasing trend for bigger waves, whereas the feeder currents tend to decrease for the weak side. This indicates growing asymmetry for bigger waves.

As the feeder currents converge, they turn offshore through the channel. The ADV's located at this turn of the rip are used to compute the average speed on each side of the channel center. Comparing the average speeds at the turn can indicate which side is the dominant circulation side of the rip system. The speed at the turn of the feeder currents is plotted for the dominant side as a function of the wave height in Figure 3.25. The grouping of tests according to wave period does not reveal any obvious trend; it appears

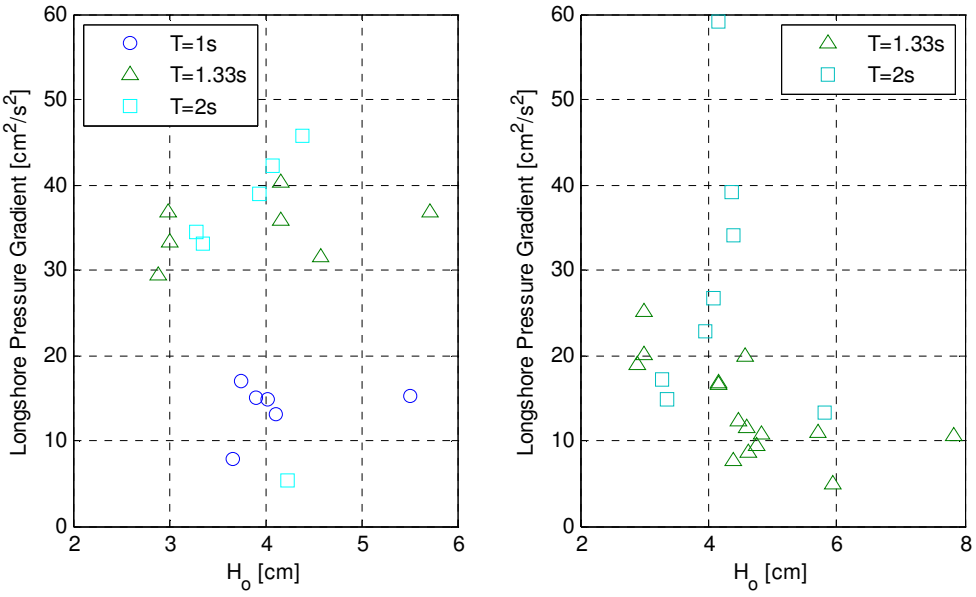

Figure 3.22: Effect of mean offshore wave height on the mean longshore pressure gradient for the side of dominant circulation (left) and weak circulation (right) (positive pressure gradient is toward channel)

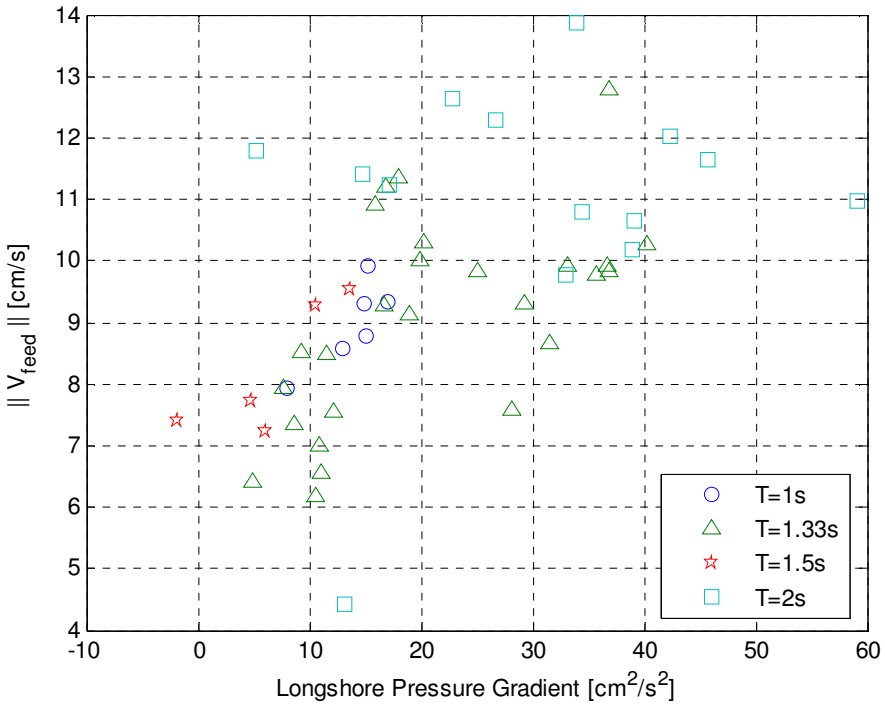

Figure 3.23: The mean feeder current speed versus the mean longshore pressure gradient (positive velocity and pressure gradient are toward the channel)

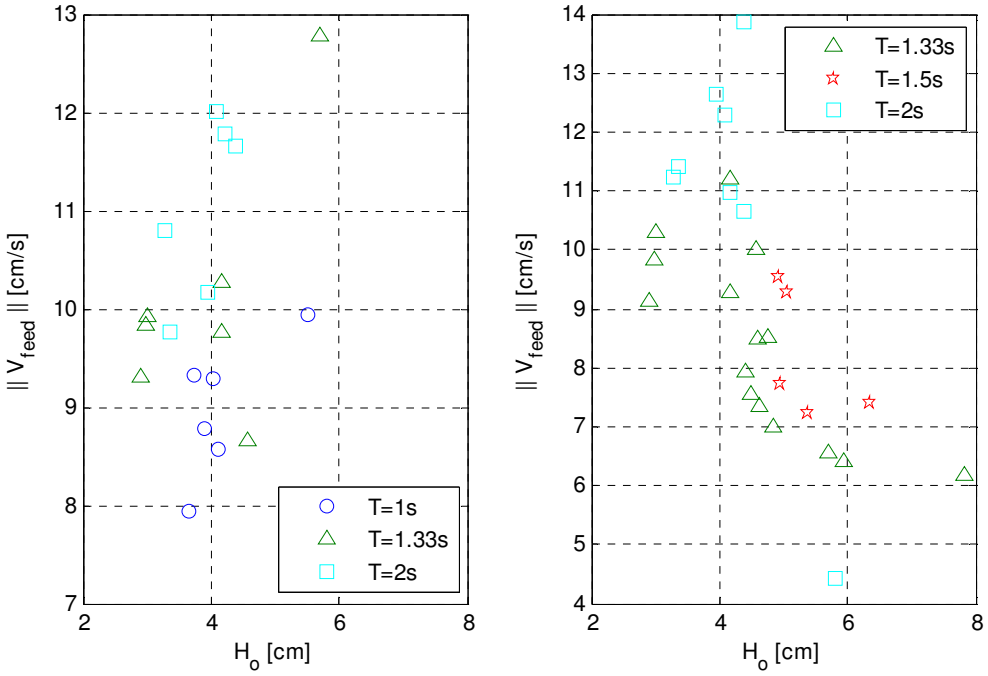

Figure 3.24: Effect of mean offshore wave height on the feeder current for the dominant side of circulation (left) and weak circulation (right)

that the wave height is the most important parameter for the flow speed at the turn of the feeders into the rip.

The convergence of currents and the wave setup in the channel entrance causes an increase in the water level relative to the offshore which creates a cross-shore pressure gradient. This cross-shore pressure gradient (*XPG*) is determined from two wave gauges, one in the channel entrance and another in the exit of the channel, using the equation given by

$$XPG = g\left(h + \frac{(\overline{\eta}_{i+1} + \overline{\eta}_i)}{2}\right)\left[\frac{\overline{\eta}_{i+1} - \overline{\eta}_i}{x_{i+1} - x_i}\right], \qquad (3\text{-}16)$$

where g is the acceleration due to gravity, h is the still water depth at the center of the two gauges, and $\overline{\eta}$ is the local surface elevation at the two cross-shore positions given by x_i

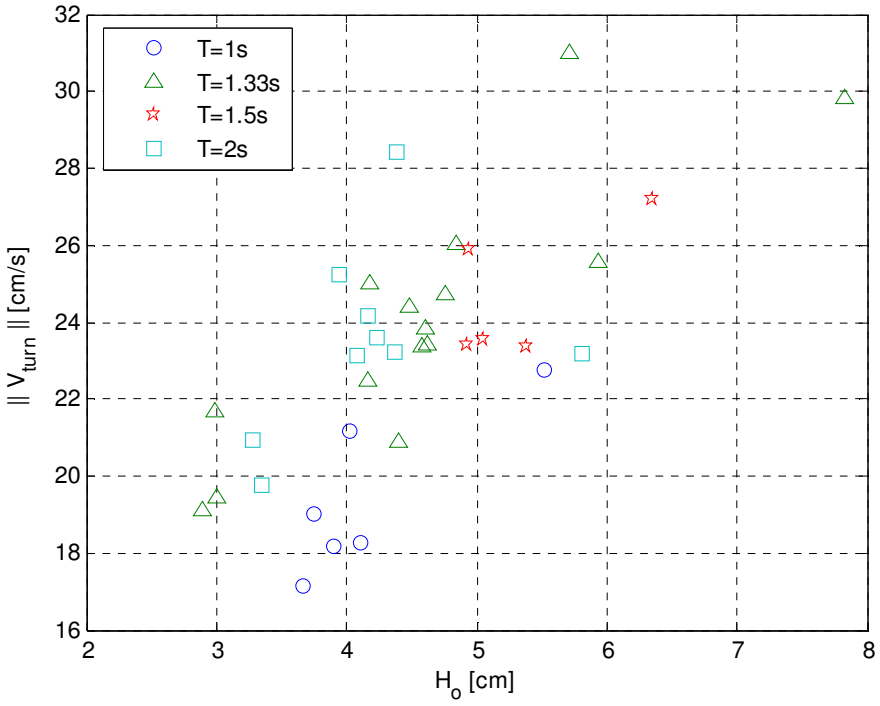

Figure 3.25: Effect of mean offshore wave height on the mean flow speed at the turn of the feeders into the rip

and x_{i+1} corresponding to the wave gauges at the channel entrance and exit, respectively. The cross-shore pressure gradient is plotted against wave height in Figure 3.26. An increase in wave height is clearly seen to increase the mean cross-shore pressure gradient, which is expected since this gradient is a function of the wave setup.

The pressure gradients in the channel drive the flow through the rip. The rip current is measured by bin-averaging the drifter speeds at the exit of the channel using a 1 m x 1 m square bin. Figure 3.27 shows the rip speed at the exit of the channel as a function of the offshore mean wave height. It is evident that the rip speed increases as wave height increases.

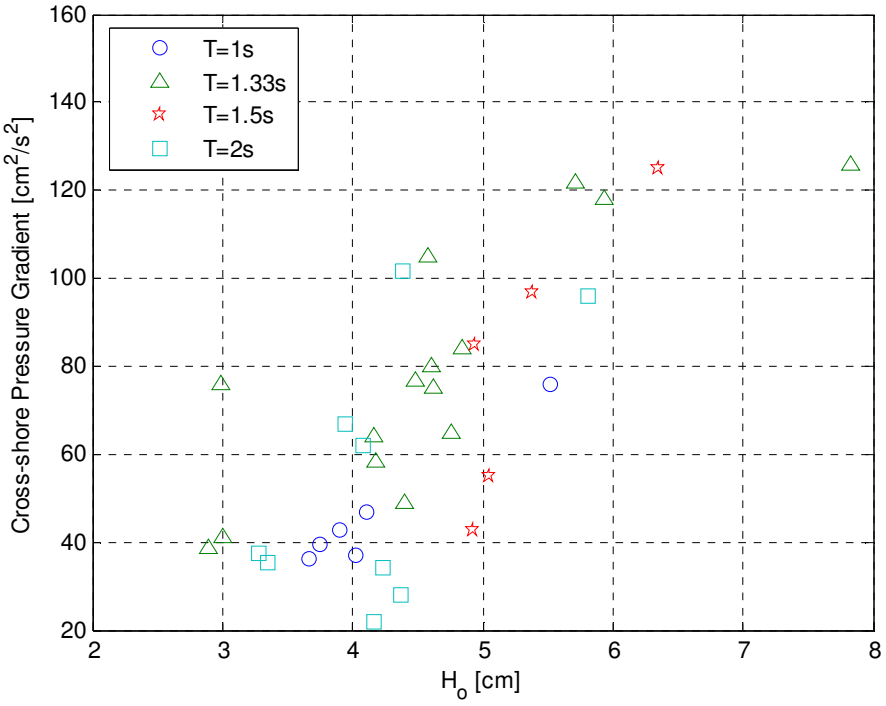

Figure 3.26: Effect of mean offshore wave height on the mean cross-shore pressure gradient in the channel (positive is directed offshore)

Overall, the wave height is shown to be the primary wave parameter controlling the rip current system mean properties. Increasing the mean wave height appears to increase the wave setup, the feeder current of the dominant side, the flow speed at the turn in the channel, the cross-shore pressure gradient, and the rip speed but surprisingly not the longshore pressure gradient.

3.5.2 Circulation Cell Properties

The video measurements of the rip current system provide a global description of the mean circulation cell. The measured circumferential velocity component of the flow in circulation cells is used as a measure of cell strengths. For each cell, velocities are spatially averaged within circular bins with a radius of 25 cm for 363 locations varying

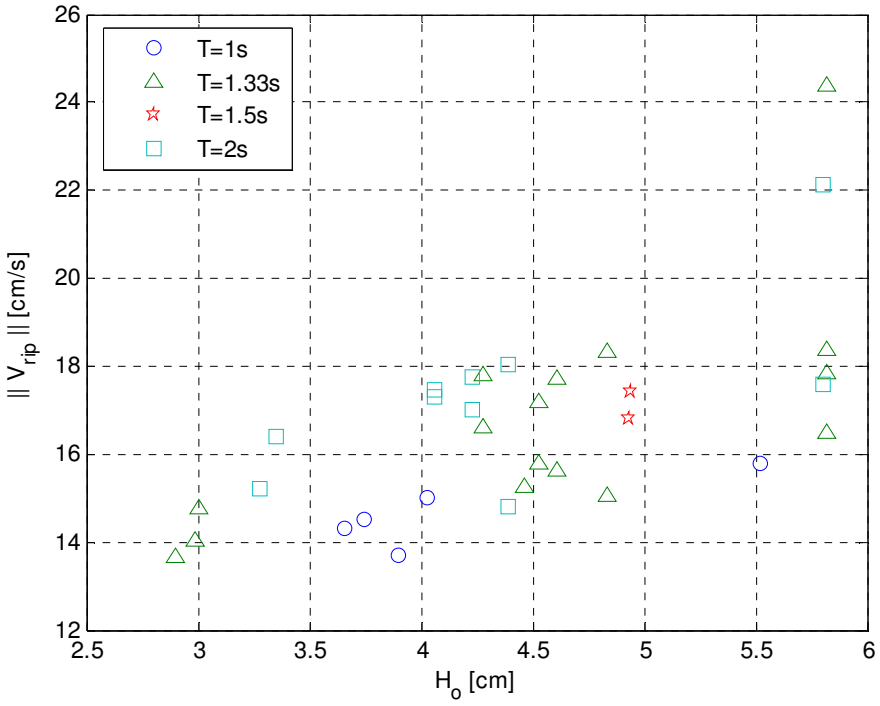

Figure 3.27: Mean rip speed from the video measurements versus the mean offshore wave height

from 0.25 m to 3.25 m from the center of circulation. The mean Cartesian velocity field is transformed to polar velocities about the center of circulation and is averaged for all bins. The average circumferential velocity is determined for both circulation cells in every test.

In Figure 3.28, the average circumferential cell velocity for each side is plotted to show the strength and symmetry of the rip system for each combination of the target wave amplitude and period. Points above the line, represent tests that are left dominant whereas points below the line are right dominant tests. The distance from the symmetry line indicates the asymmetry of the rip system. Notice from the figure that tests with the same target amplitude and period show similar strengths and symmetry. There are two tests that show a different behavior than others with the same amplitude and period, I1

and G19. I1 is the only 2.5-cm, 1-s test that is strongly left-biased, all others are symmetric or right-biased. Even more obvious is G19, the only 4-cm, 1.33-s test with the left-biased cell; all other tests with this amplitude and period were strongly dominant on the other side. However, it is clear that the incident wave amplitude and period affect the behavior of the circulation cells.

To characterize the total strength of both circulation cells in the rip system, an average of the left and right circumferential cell velocities is calculated. Figure 3.29 shows the average circulation speed as a function of the mean offshore wave height. It is clear that the speed of the circulation cell increases with increasing wave height. There is some grouping by wave period in the figure but with no obvious trend. In general, it appears that the middle wave periods of 1.33 and 1.5 s produce larger circulation speeds, for similar wave heights, than the 1- and 2-s waves.

To quantify the asymmetry of a rip system, the average circumferential cell velocity for the left ($U_{\theta,l}$) and right side ($U_{\theta,l}$) is used to define an asymmetry ratio (*AR*), with complete asymmetry being 1 and symmetry being 0 using the equation given by

$$AR = \sqrt{\frac{\left(U_{\theta,r} - U_{\theta,l}\right)^2}{\left(U_{\theta,r} + U_{\theta,l}\right)^2}} \,. \tag{3-17}$$

This asymmetry ratio as a function of the mean offshore wave height is shown in Figure 3.30, demonstrating that the asymmetry increases with increasing wave height. This agrees with the findings from the instruments; for larger wave heights, the dominant circulation side strengthens whereas the weak side weakens producing a more asymmetrical system.

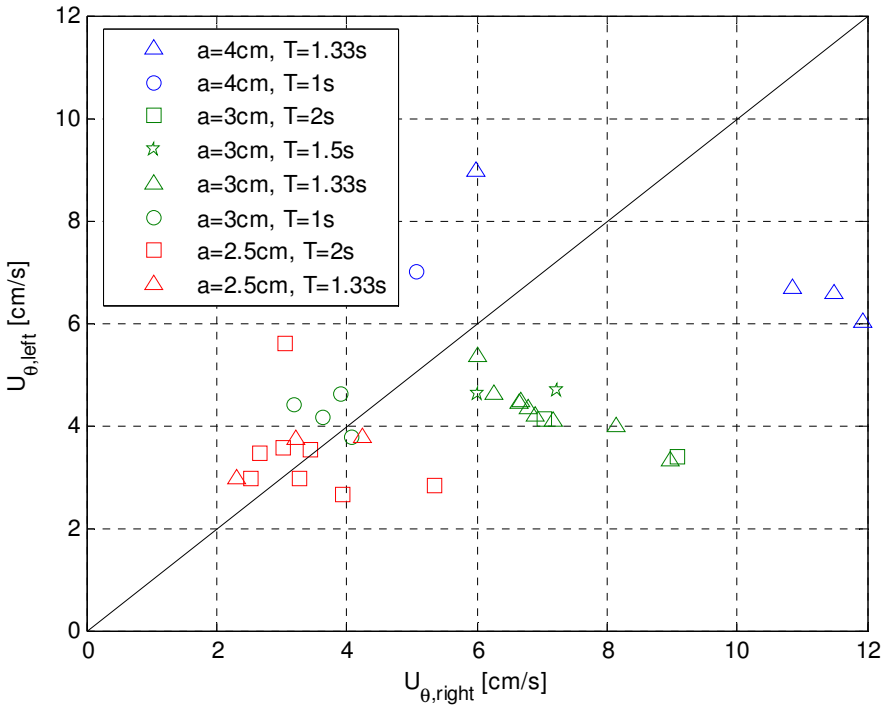

Figure 3.28: Average circulation cell speed for left and right cells for different incident wave amplitudes and periods with line of perfect agreement

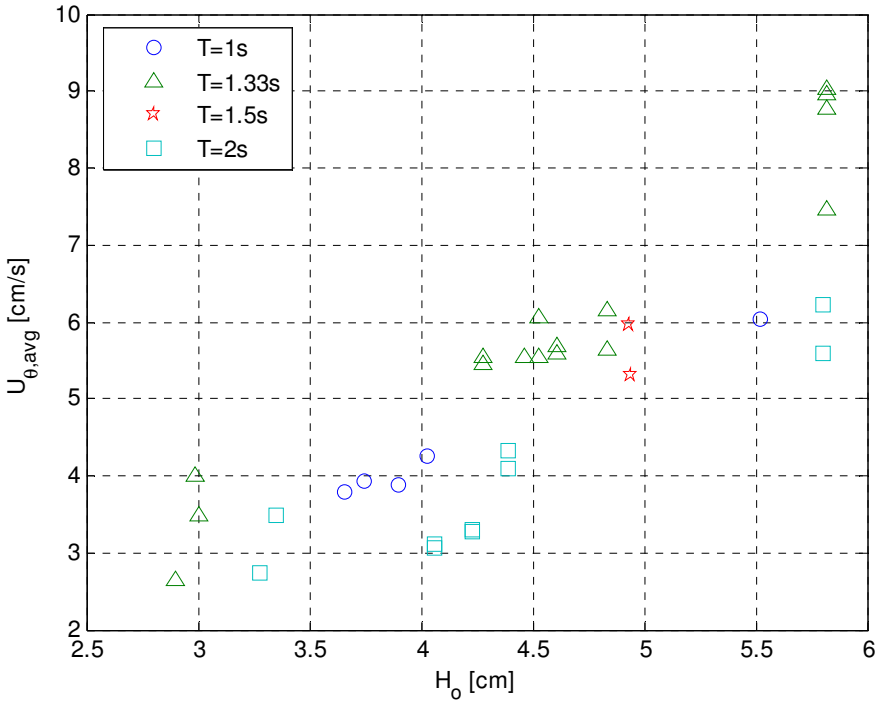

Figure 3.29: Average circulation cell speed versus average incident wave height for the different wave periods

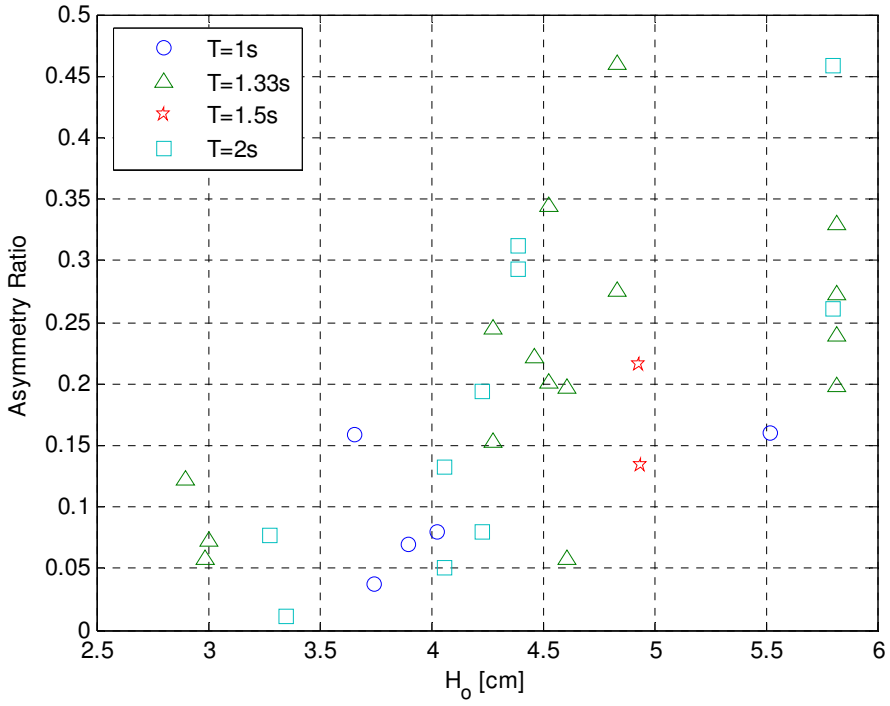

Figure 3.30: Asymmetry ratio versus average incident wave height

A meandering of the rip back and forth is observed in several of the videos. If the rip migrates from left to right making the side with the dominant circulation cell alternate, this produces a wide range in the direction of the rip. The rip direction time series is determined from the low-passed rip velocity components U and V from the group of ADV's in the exit of the rip channel by

$$\tan\theta = \frac{U}{V}, \tag{3-18}$$

where θ is the rip direction. A time series for the rip direction is shown in Figure 3.31, where positive indicates a rip turning left. Notice that the rip is meandering back and forth throughout the I6 experiment, which has one of the most symmetric mean velocity fields.

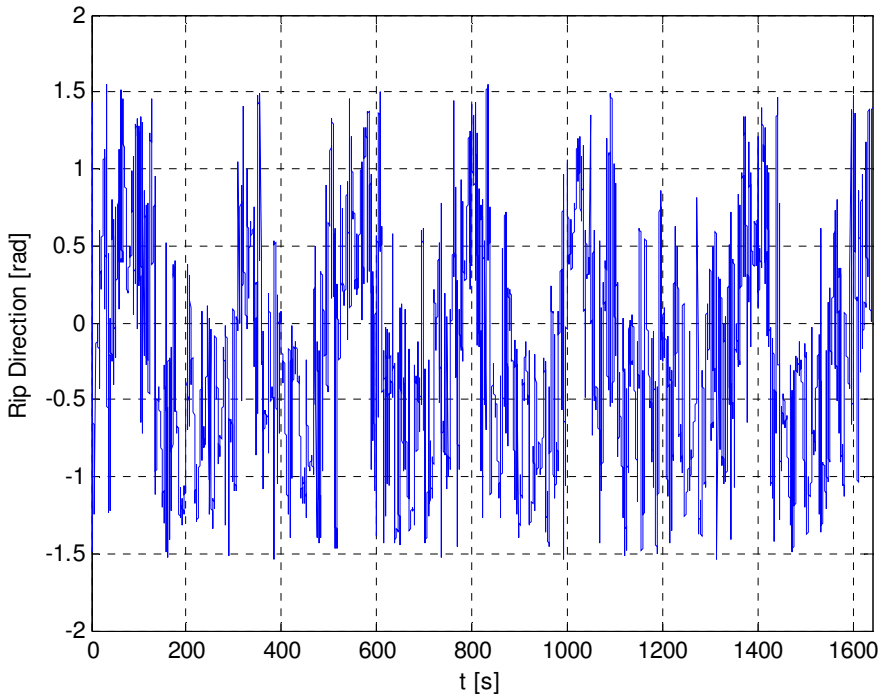

Figure 3.31: Rip direction time-series from the video (I6) showing the rip meandering back and forth (positive is left and negative is right directed)

The cross-shore locations of the circulation cell centers are plotted as a function of the mean wave height in Figure 3.32 where decreasing *X* is further offshore. It is evident that the center of circulation moves further offshore with the increasing mean wave height. With previous observations, this indicates that for larger wave heights, the circulation cells have larger velocities, are more asymmetric, and are centered further offshore.

It seems logical that as the circulation cell moves further offshore, that the width of the circulation cell would increase since the feeders are constrained at the bars. Using the circulation cell measurements, the radius of the maximum circulation gives a measure

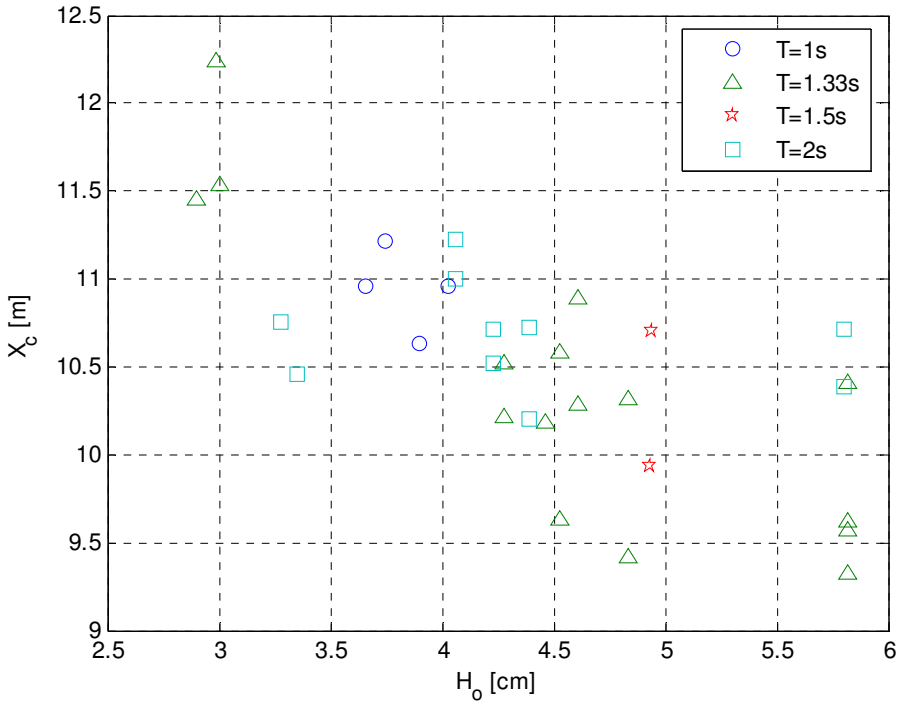

Figure 3.32: Cross-shore location of circulation cell centers versus average incident wave height (decreasing X is further offshore)

of the cell width. Figure 3.33 shows this measure of cell width versus the mean wave height. The general trend is that the radius of the cells increases for larger wave heights. Also from the circulation cell measurements, the maximum circulation can be determined. Figure 3.34 shows that the maximum circulation as a function of the mean wave height. It is clear that the maximum circulation increases with increasing wave height. This is consistent with previous observations from the measurements since both the cell speed and width are increasing for larger wave heights.

The circulation cells tend to have higher velocities, are further offshore, and produce stronger circulations with an increase in mean wave height. It has also been observed that the rip systems become more asymmetrical for larger wave heights; the tests with smaller waves were more symmetric. These symmetric tests have a wide

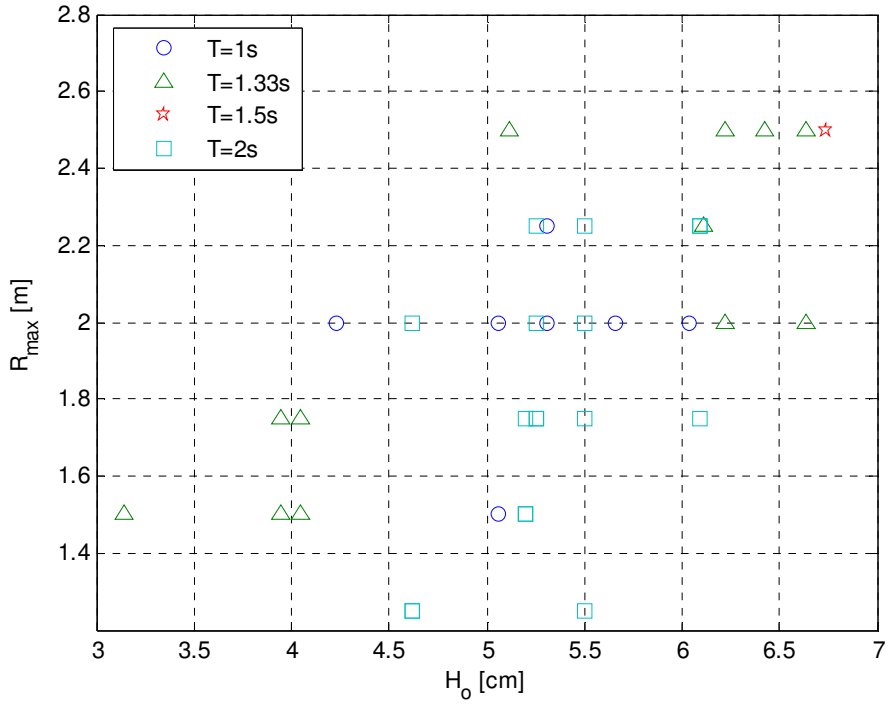

Figure 3.33: The radius of maximum circulation versus the mean offshore wave height

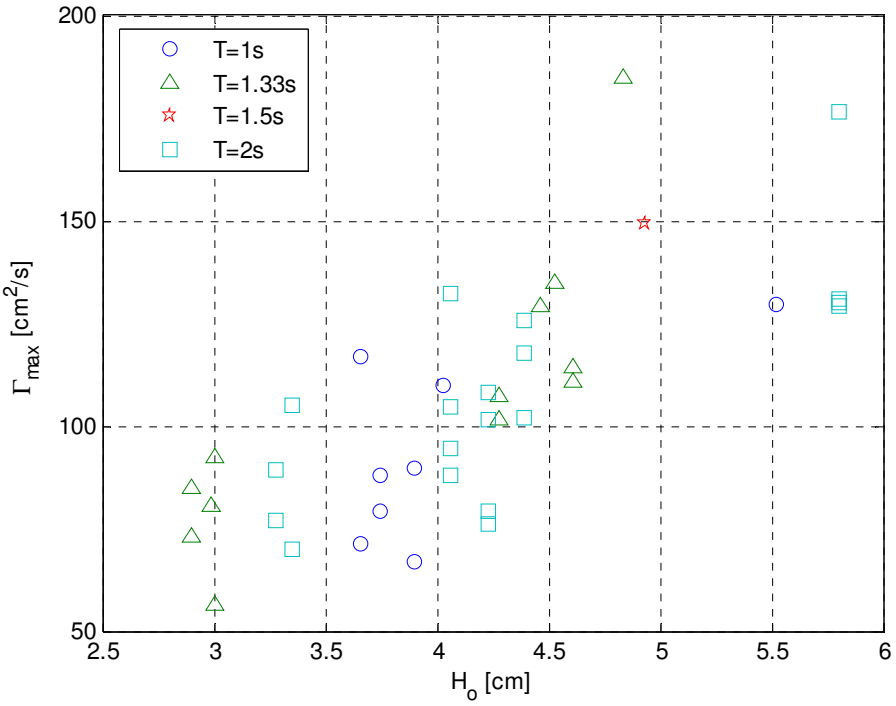

Figure 3.34: Maximum circulation versus average incident wave height

variation in the rip direction consistent with meandering back and forth. The characterization of this meandering and other observed pulsations in the rip system are explored in the next chapter.

CHAPTER 4

RIP CURRENT PULSATIONS

The flows in rip current systems have been observed to be non-steady, pulsating at a variety of time scales (Sonu (1972), Smith and Largier (1995) and MacMahan et al. (2004a)). These pulsations are usually attributed to the groupiness of the incoming waves but have also been linked to jet instabilities (Haller and Dalrymple (2001)). In the present experiments, simultaneous measurements of the waves, pressure gradients, feeder currents, and rip currents provide a means for understanding the mechanisms of a temporally varying rip current system. This chapter includes observations from spectral analyses of these time-varying rip systems and characteristics of the energetic pulsations.

4.1 Low-Frequency Energy in a Rip Current System

Since there are various forcing mechanisms at different time scales, spectral analysis can indicate important information about the dominant forcing in the system. For the bi-chromatic wave conditions, the wave height modulations occur at a set forced frequency. However, the rip system also exhibits significant energy at other unforced frequencies as well. For the monochromatic tests, the waves contain no low-frequency forcing since there are no forced wave height modulations. Bi-chromatic conditions, however, have both a wave height modulation and a bound long wave and therefore the rip system is expected to pulsate at the wave group frequency. The bound long wave is caused from the variation in wave setdown, which is proportional to the wave height squared, caused from the wave groups and propagates with the group at the group

velocity. This sub-section discusses the observations from the spectral analysis of test H13, an experiment with a short-wave period of 2 s and a wave group period of 32 s corresponding to video test I6. Unless noted otherwise, the spectra given are computed using Fast Fourier Transforms with a Hanning window and four degrees of freedom.

Figure 4.1 shows a spectrum of the offshore water level time-series for test H13. Notice the energy peak at 0.5 Hz corresponding to the short-wave forcing and the peak around 0.03 Hz corresponding to the wave groups. The wave frequency is approximately 90 times more energetic than the wave group frequency. In the trough, however, the wave group spectral energy is approximately 3 times larger than the energy at the short-wave frequency, as shown in Figure 4.2.

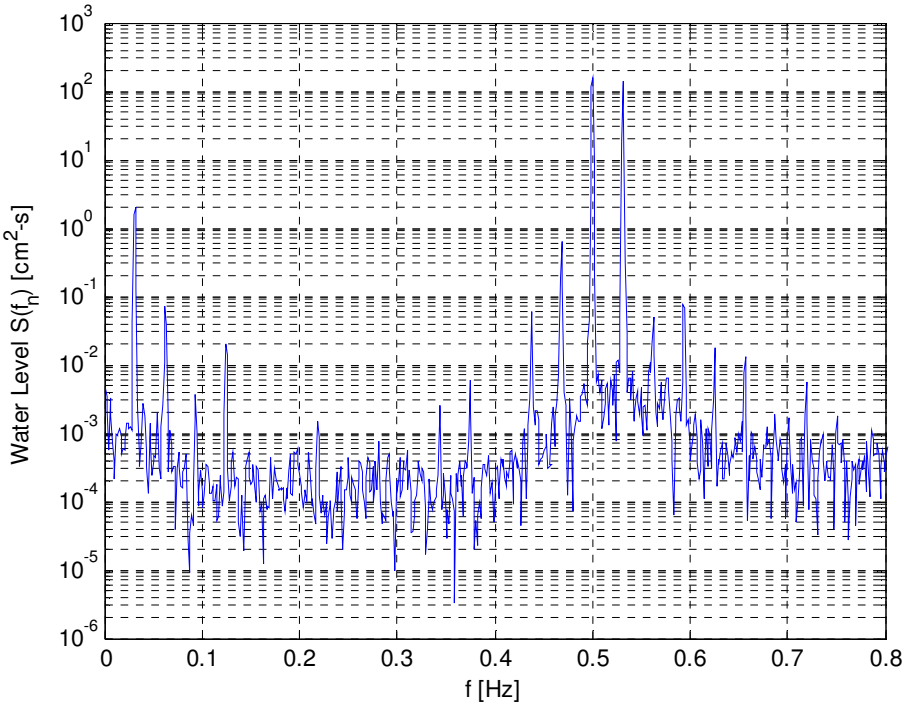

Figure 4.1: Frequency spectrum of offshore water level from experiment H13 with 2-s waves and 32-s wave groups ($x = 6$ m , $y = 14.2$ m)

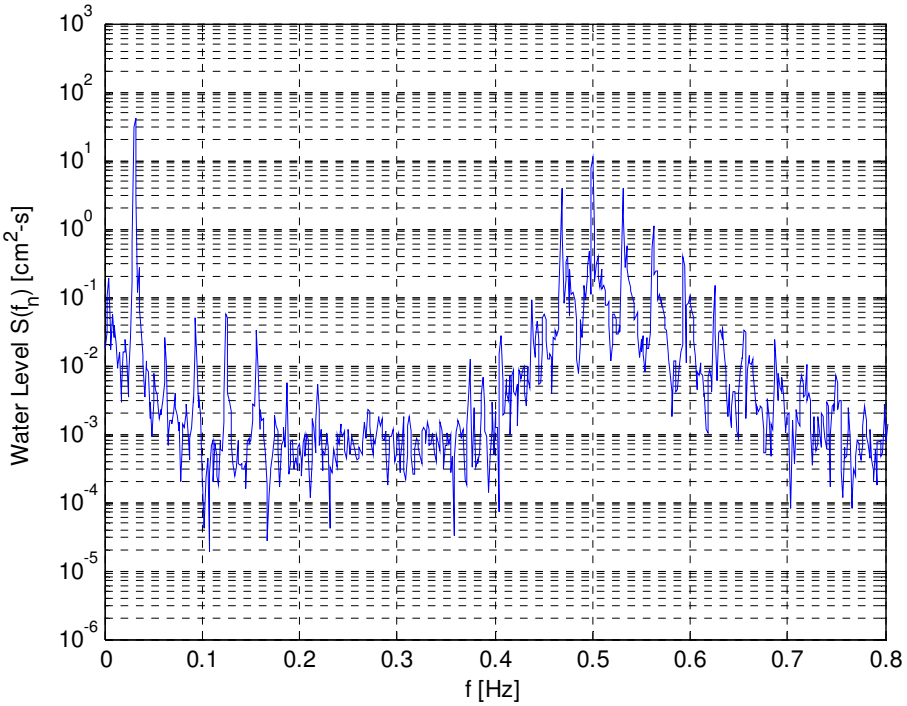

Figure 4.2: Frequency spectrum of trough water level from experiment H13 with 2-s waves and 32-s wave groups ($x = 12.33$ m , $y = 11.76$ m)

To investigate the low-frequency pulsations, frequencies lower than the incident wave band are investigated hereafter. Figure 4.3 shows the same spectrum as in Figure 4.2 for the 0 – 0.05 Hz frequency band. It is clear that the trough water level is the most energetic at the wave group frequency. Also note the small energy peak around 0.005 Hz.

Since it is evident that the water level responds to the wave groups, it is expected that the depth-integrated longshore pressure gradient that is calculated by the slope in the water level using Equation 3-15 also contains energy at the wave group frequency. A spectrum of the longshore pressure gradient, shown in Figure 4.4, is computed to show that most of the spectral energy, like the water level, is at the wave group frequency.

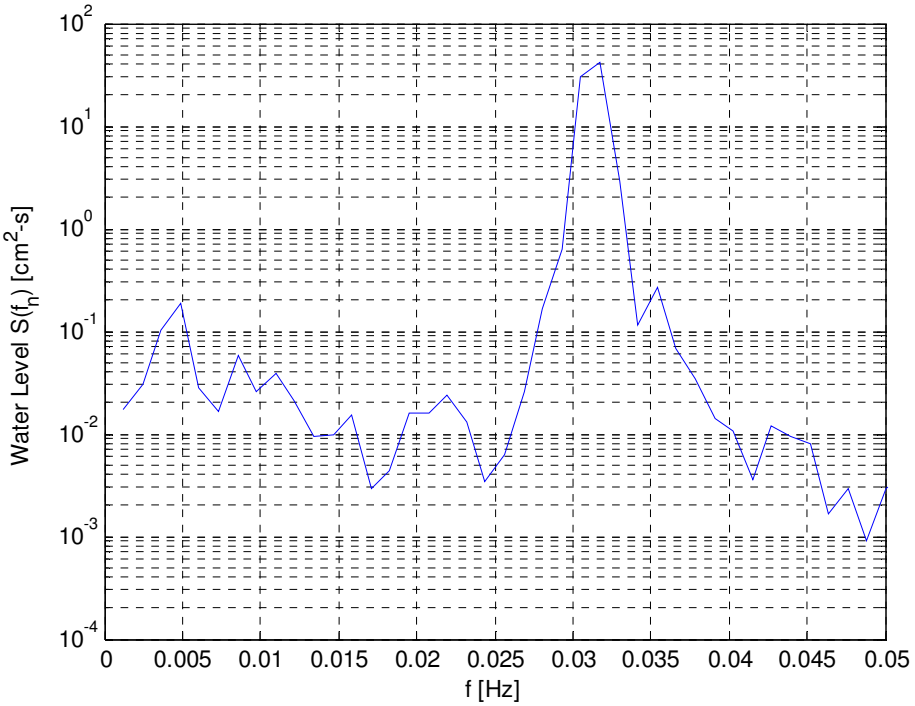

Figure 4.3: Frequency spectrum of water level from experiment H13 with 32-s wave groups ($x = 12.33$ m , $y = 11.76$ m)

Also notice an energetic peak at a frequency around 0.004 Hz, which is approximately 10 times less energetic than the wave group frequency.

Since the feeder current is driven by the longshore pressure gradient forcing, the feeder current should respond similarly. The frequency spectrum for the longshore current, shown in Figure 4.5, has most of the spectral energy at the wave group frequency. There is less low-frequency energy relative to the wave group energy in the feeder currents than in the longshore pressure gradient energy at the low frequency. The pressure gradient energy at the low frequency has 1/10th of the spectral energy at the wave group frequency and the feeder current energy at the low frequency has approximately 1/12th of the energy at the wave group frequency.

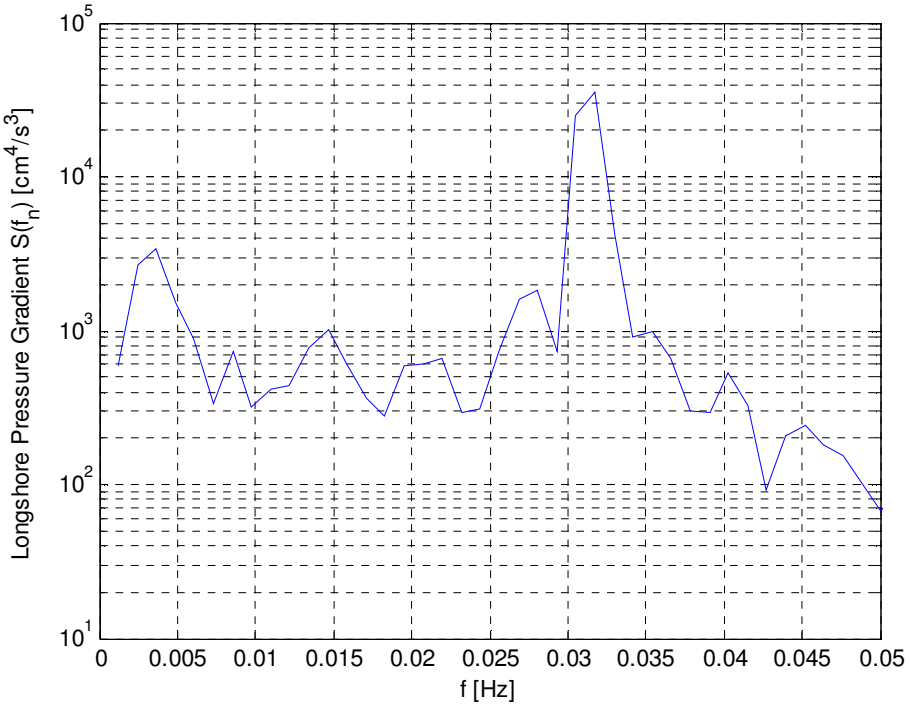

Figure 4.4: Frequency spectrum of longshore pressure gradient from experiment H13 with 32-s wave groups centered at ($x = 12.33$ m , $y = 11.60$ m)

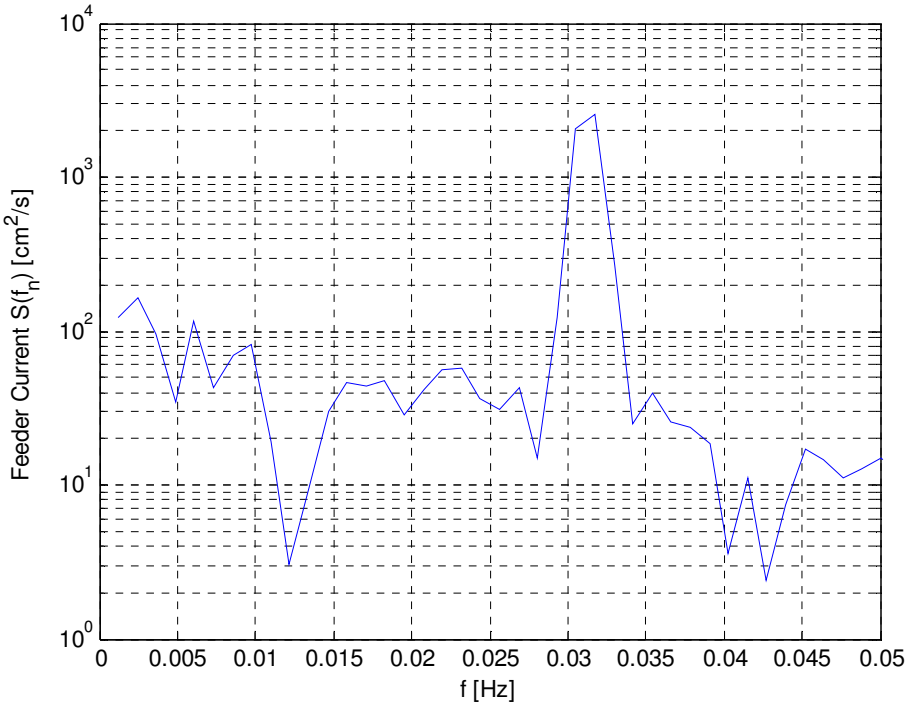

Figure 4.5: Frequency spectrum of a feeder current from experiment H13 with 32-s wave groups ($x = 12.13$ m , $y = 12.39$ m)

At the point in the channel where the feeders turn offshore, frequency spectra of both the longshore and cross-shore velocity components are computed. Notice that the spectrum of the cross-shore component of the turning current, shown in the top of Figure 4.6, has most of the spectral energy at the wave group frequency, similar to the longshore pressure gradient and feeder currents. However, the longshore turning currents, seen in the bottom of Figure 4.6, has more energy at the lower frequency of 0.04 Hz than at the wave group frequency. This longshore component of the turning current also has a third frequency, f = 0.035 Hz, with similar energy to the wave group frequency. This third frequency is related to the others, however, as a sum frequency of the lower-frequency and the wave group frequency. Since the source of the wave group frequency is known, one of the other energy peaks may result from the non-linear interaction with the group. Notice that the low-frequency has approximately 1.5 times more spectral energy than the wave group frequency in the longshore component of the turning current.

As the two feeder currents converge, they accumulate water in the channel causing an increase in water level. This increase in water level creates two pressure gradients: one in the cross-shore directed offshore and another directed away from the channel in the longshore direction. For the cross-shore pressure gradient, a spectrum is computed and shown in Figure 4.7. The low-frequency is not energetic in the spectrum of the cross-shore pressure gradient, which indicates that the wave groups are the primary forcing in the cross-shore. The spectrum of the outward-directed longshore gradient, shown in Figure 4.8, has minimal energy at the wave group frequency with most of the energy at this low-frequency around 0.04 Hz. Since the turning currents are in the middle of this outward-directed pressure gradient, it seems logical that the low-frequency

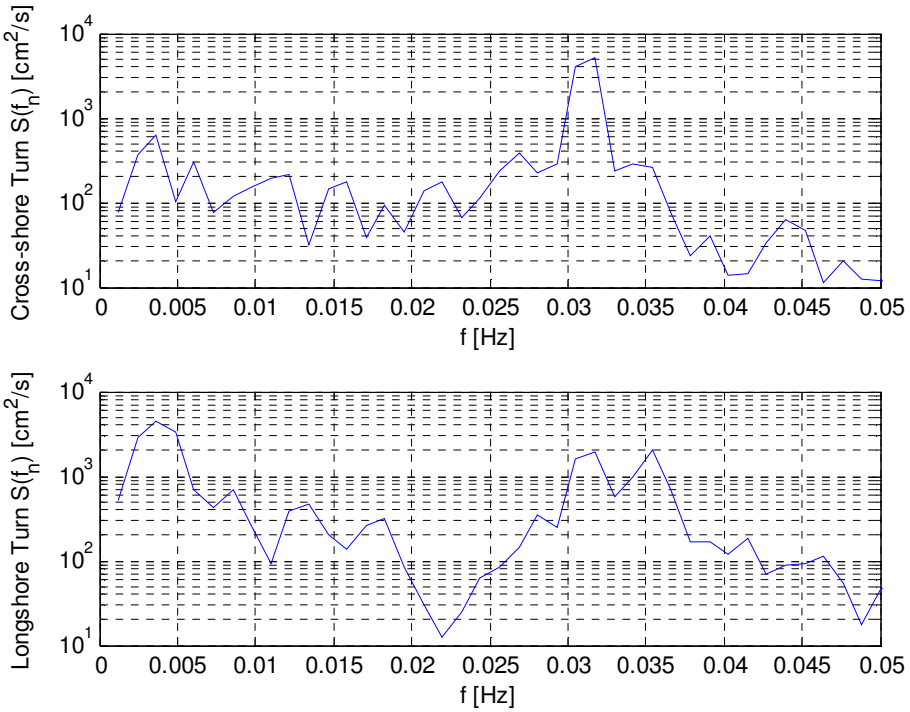

Figure 4.6: Frequency spectra of the cross-shore (top) and longshore (bottom) components of the turning current from experiment H13 with 32-s wave groups ($x = 13.3$ m , $y = 12.4$ m)

response seen in the longshore component of the turning currents is related to this pressure gradient.

To determine if the low-frequency in this outward-directed pressure gradient is evident in the two water levels making this gradient, spectra are computed for the two water levels. Figure 4.9 shows the spectrum of the water level in the center of the channel (top) and the water level at the corner of the bar (bottom). Notice that the energy at the wave group frequency dominates in both cases. The water level at the corner of the bar, however, has twice the spectral energy at the low-frequency than the water level in the center of the channel. The energy at the wave group frequency for the two water

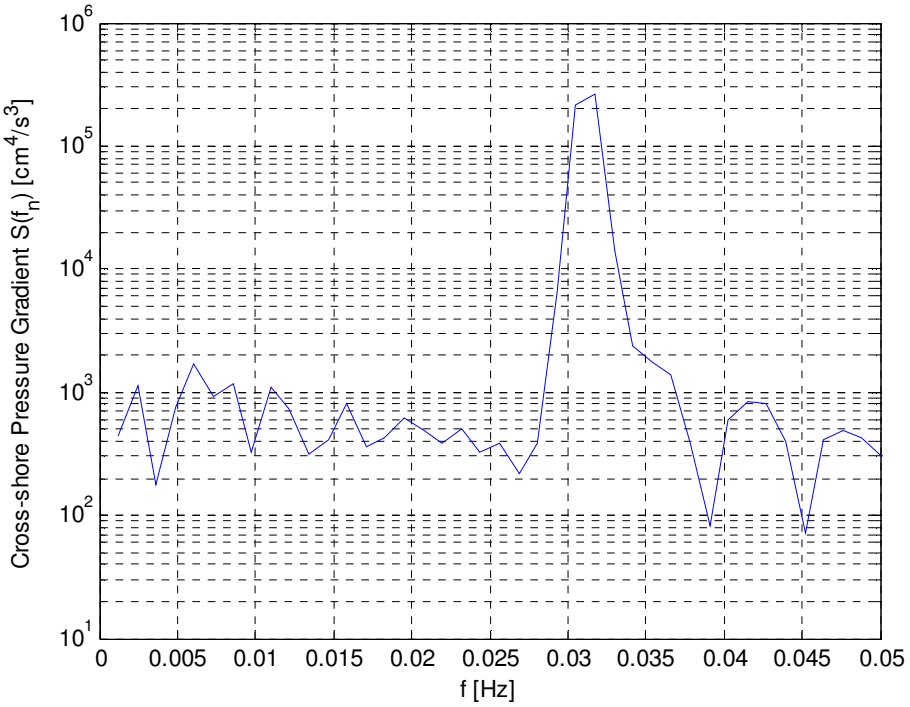

Figure 4.7: Frequency spectrum of cross-shore pressure gradient from experiment H13 with 32-s wave groups centered at ($x = 11.8$ m , $y = 13.69$ m)

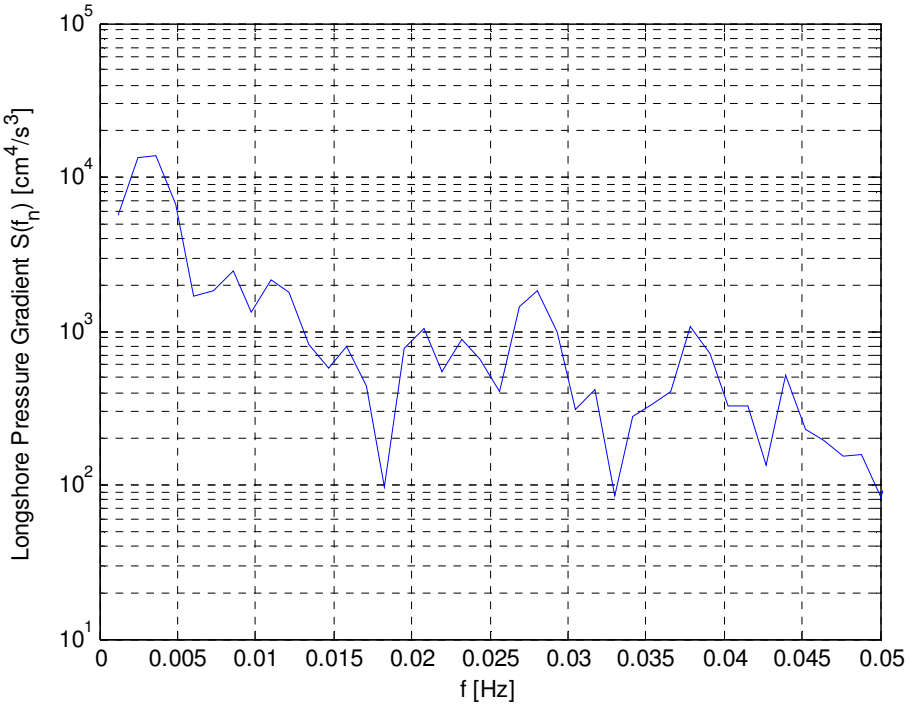

Figure 4.8: Frequency spectrum of long-shore pressure gradient from experiment H13 with 32-s wave groups centered at ($x = 12.32$ m , $y = 13.21$ m)

levels, however, is nearly equal. This indicates that the outward-directed pressure gradient does not respond at the wave group frequency since the relative responses in the water levels rises and falls in response to the group at the same time, but does respond at the lower-frequency since the water level near the bar has a low-frequency modulation not apparent in the center of the channel.

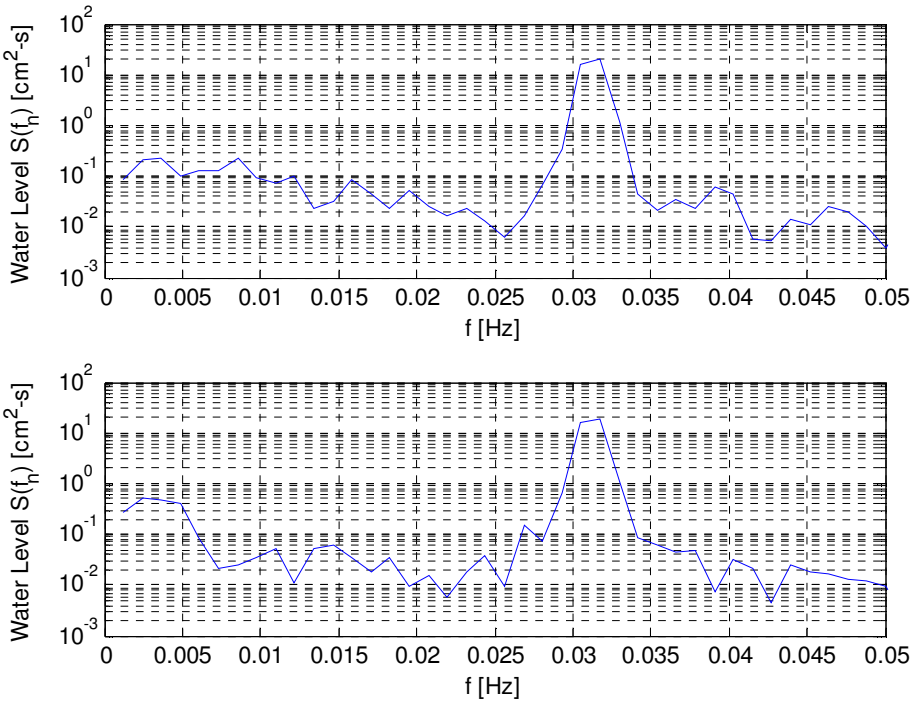

Figure 4.9: Frequency spectrum of the two water levels used in calculating the outward-directed longshore pressure gradient from experiment H13 with 32-s wave groups: top - ($x = 12.33$ m , $y = 11.76$ m), bottom - ($x = 12.32$ m , $y = 12.81$ m)

Since the rip current forcing of the cross-shore pressure gradient is responding primarily at the wave group frequency, the rip current should show a strong response at the wave group frequency. Spectra of the cross- and longshore components of the rip are computed and shown in Figure 4.10. The spectrum of the cross-shore rip, shown at the top of Figure 4.10, has a strong wave group response but also a significant amount of

energy at the low-frequency around 0.04 Hz. The wave group spectral energy is 6 times higher than this low-frequency energy. The longshore rip spectrum, shown in the bottom of Figure 4.10, has minimal energy at the wave group frequency and the majority of the spectral energy at the low-frequency. This indicates that this long-period mechanism observed in the longshore-directed pressure gradient and turning currents is also related to the longshore component of the rip velocity.

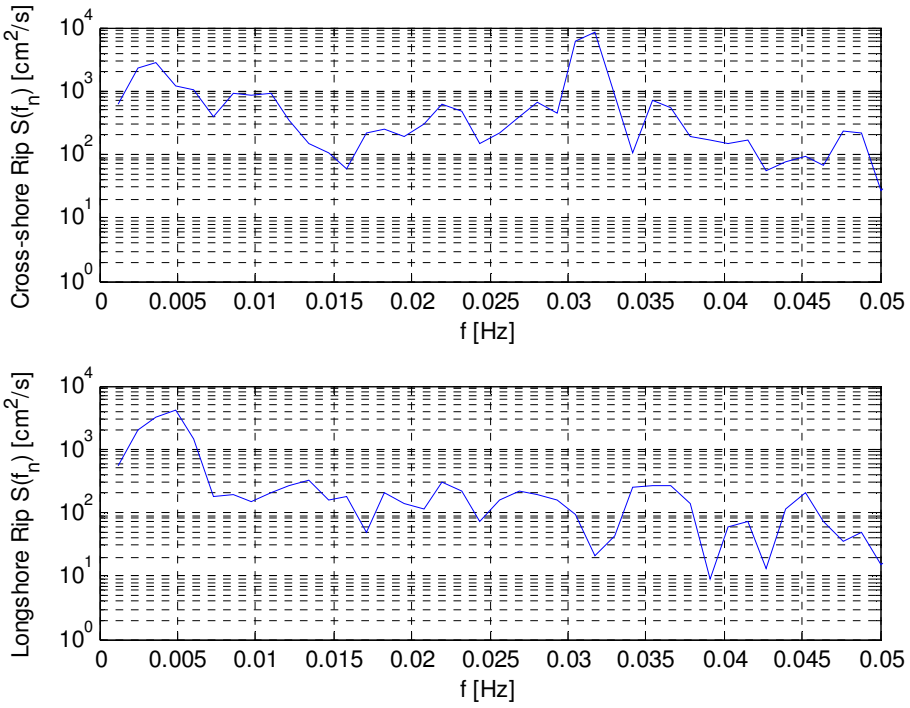

Figure 4.10: Frequency spectrum of cross-shore (top) and longshore (bottom) components of the rip current from experiment H13 with 32-s wave groups ($x = 13.48$ m , $y = 10.81$ m)

In this H13 test, three energetic frequencies are observed: the wave group frequency, a low-frequency between 0.004 and 0.005 Hz, and the interaction frequency of the wave group and low-frequency. Some tests have distinct energy peaks at three similar frequencies, whereas other tests have none of them. The occurrence of the low-

frequency peak seems to be independent of the wave group since some monochromatic tests have this energy. Shown in Figure 4.11, are spectra of the turning currents for a monochromatic case showing a low-frequency energy peak around 0.0125 Hz. Since there are no wave groups in the monochromatic tests, however, there is no interaction frequency between the two. Not all of the monochromatic cases have these low-frequency energy peaks. The spectra, shown in Figure 4.12, are for the turning currents of a monochromatic test showing no distinct low frequency energy peaks. All bi-chromatic tests have energy at the wave group frequency but some are not energetic in the low-frequencies. Figure 4.13 shows spectra of the turning currents from a test with a 16-s wave group. Notice that there is no distinct low frequency energy peak that approaches the spectral energy of the wave group frequency.

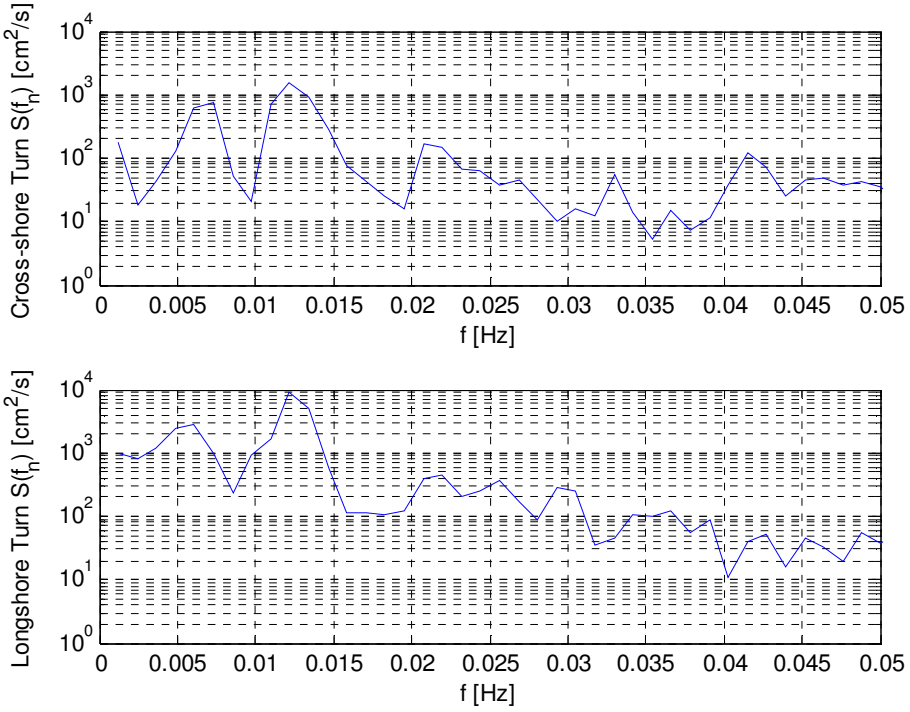

Figure 4.11: Frequency spectrum of turning current from experiment H8 with monochromatic waves ($x = 13.3$ m , $y = 12.4$ m)

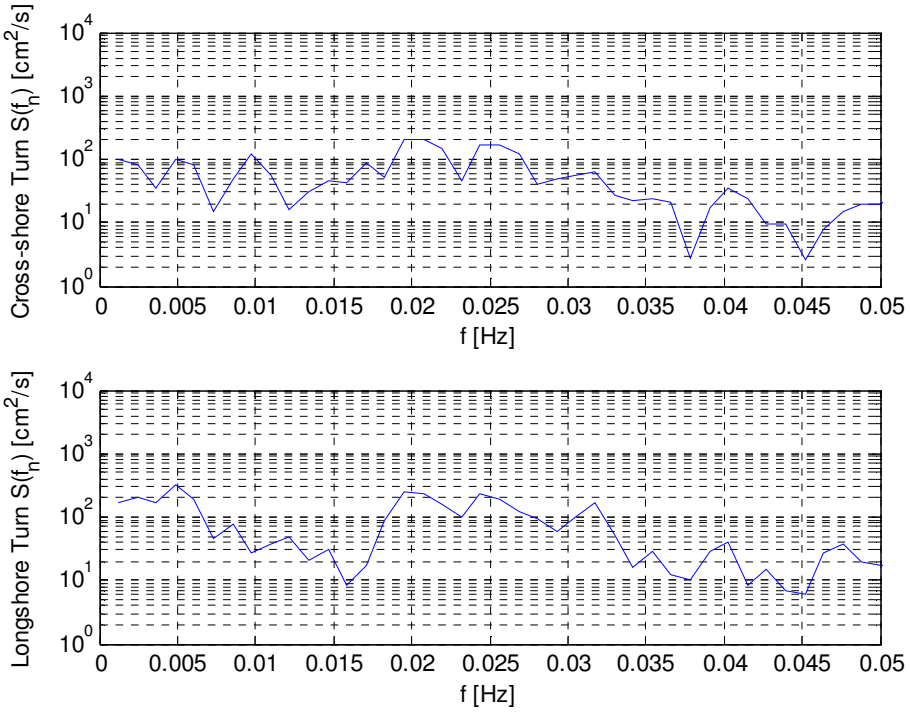

Figure 4.12: Frequency spectrum of turning current from experiment F8 with monochromatic waves ($x = 14.25$ m , $y = 12.45$ m)

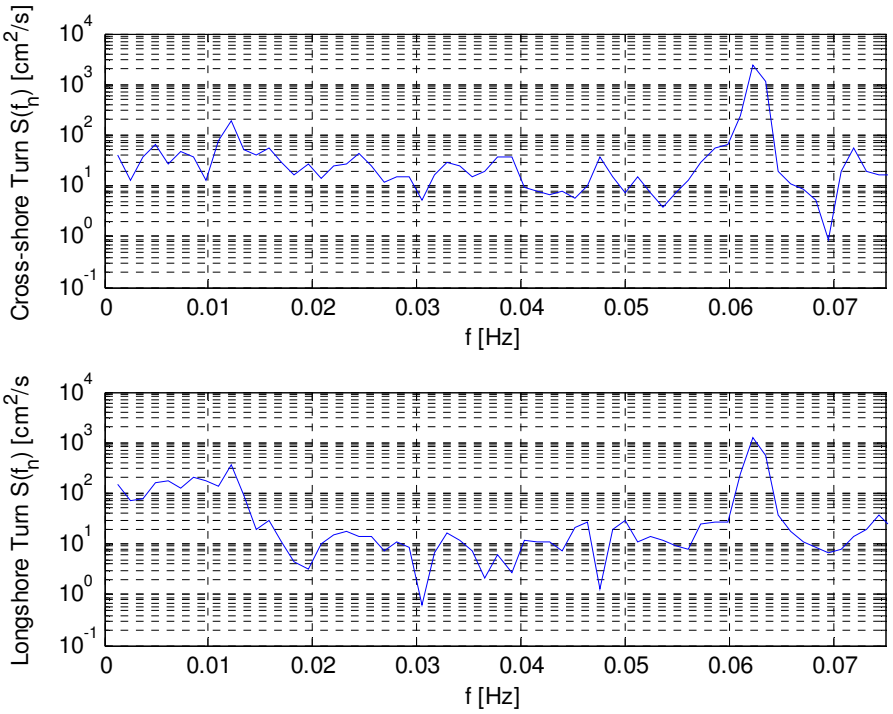

Figure 4.13: Frequency spectrum of turning current from experiment F19 with 16-s wave groups ($x = 14.25$ m , $y = 12.45$ m)

4.2 Characterization of Low-Frequency Motion

Of the observed pulsations in the spectra of the rip current system, the easiest to explain is the wave group response. Since the frequency for the modulations in wave height are specified, the forcing mechanism for those responses is known. Rip current features that have a strong response at the wave group frequency can indicate how the wave groups affect the system. Also, the time-lags between the wave group pulses of the different time-series can help to develop a sequence of the local processes in the rip current system.

4.2.1 Wave Group Frequency

Observations from the Section 4.1 indicate that the wave group frequency is the most energetic frequency in the spectra of water level, trough longshore pressure gradient, feeder current, cross-shore pressure gradient, and the cross-shore component of the rip current. It is apparent that these features are the primary elements of rip current generation and as they increase the whole system should strengthen.

The existence of the bound long wave is investigated by comparing the time lags at the wave group frequency between the offshore wave gauge and the gauges in the channel to the theoretical propagation time of a long wave at the group velocity. It is found that the calculated time lags are much longer than the theoretical bound long wave lag. Also, the wave group envelope, calculated using the Hilbert transform of the water level time series, is cross-correlated with the water level time-series. It is discovered that the offshore wave gauge is π radians out of phase with the wave group envelope, the signature of a bound long wave, but the nearshore wave gauges are in phase with the wave group. This indicates that a bound long wave does not play a role in the nearshore

and the wave group pulsations are due to the wave height modulations from the wave group. This suggests that the wave height modulations strengthen & weaken the rip current system.

The video measurements of the rip current are used to investigate the strengthening and weakening of the rip by calculating the acceleration of a drifter as it passes through the channel. The Lagrangian acceleration in the direction of the low-passed drifter velocity is a good measure for the rip strength since it is independent of rip direction. For angled rip systems, like the one shown in Figure 3.13, the cross-shore velocity component would appear weaker than a rip of the same strength directed offshore. An energy spectrum of the drifter acceleration is computed for I6 (video test of H13) using 4 degrees of freedom and a Hanning window. The spectrum, shown in Figure 4.14, shows an energy peak at the wave group frequency, which indicates that the rip system is strengthening and weakening at the wave group frequency.

To investigate how the spectral energy at the group varies over the different wave conditions, the spectral energy is plotted against the offshore significant wave height for different groupings of wave conditions. First, Figure 4.15 shows the spectral energy in the water levels at the wave group frequency for different wave periods. In general, the spectral energy at the wave group increases with increasing significant wave height. It is apparent, similar to the observations of Chapter 3, that the 1- and 2-s wave periods are the most similar and the 1.33- and 1.5-s wave period tests are also similar. Initially it seems illogical that the wave periods of the two extremes would be the most similar. However, since the 1- and 2-s wave periods are integer multiples, all the harmonics in a time-series with a 2-s period are in a time-series of the 1-s period. The only difference is that the 1-s

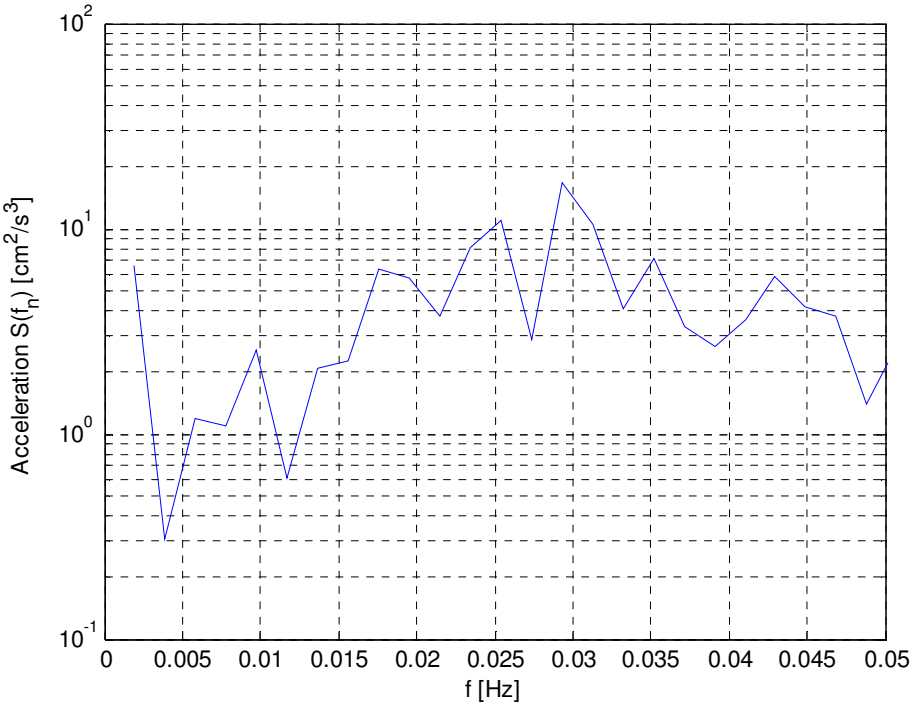

Figure 4.14: Frequency spectrum of circumferential acceleration of a drifter in the rip channel from experiment I6 centered at ($x = 10.5$ m , $y = 13.66$ m) with a 1 m x 1 m bin

wave period does not contain energy at 0.5 Hz. This provides a possible explanation of why these two wave periods appear to be the most similar.

The different groupings of the wave group period and the amplitude ratio, as shown in Figure 4.16, indicate that these parameters also have a significant role in the energy of the response. It appears that the 16-s wave groups are the least energetic wave group. The 32- and 64-s wave groups are more similar, but it is clear that the 32-s wave groups are more energetic at the group frequency. Also, it is clear from the groupings of the two amplitude ratios in Figure 4.16 (bottom) that an amplitude ratio of 1 produces a more energetic group than a ratio of 2.

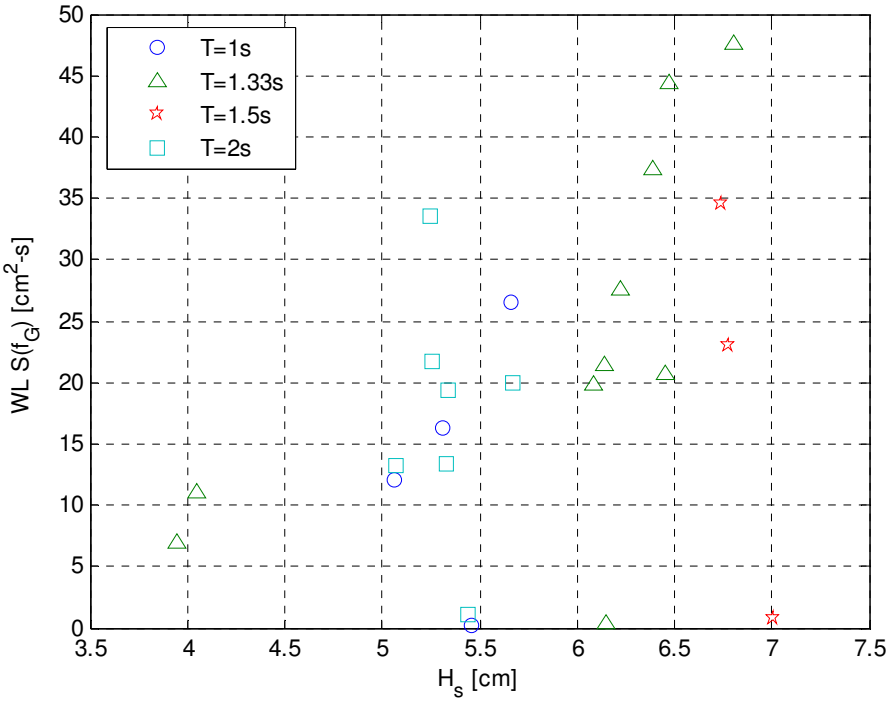

Figure 4.15: Spectral energy of the trough water levels (F series – ($x = 11.4$ m , $y = 12.3$ m) and H series – ($x = 11.76$ m , $y = 12.33$ m)) at the group frequency against the significant wave height for different groupings of wave period

A different trend is found in the spectral energy of the rip at the wave group frequency. Evident in the plot of rip energy of the group frequency versus H_s shown in Figure 4.17, the 16-s wave groups for the rip are comparable to the spectral energy of the other groups. Also, the 32-s wave groups are the most energetic in the water levels, but not necessarily the most energetic in the rip. Although the effect of wave height on the spectral energy for the rip current is similar to the water levels, the effect of the wave group period is quite different in that the 16-s wave group tests have energy similar in magnitude to the other wave group periods.

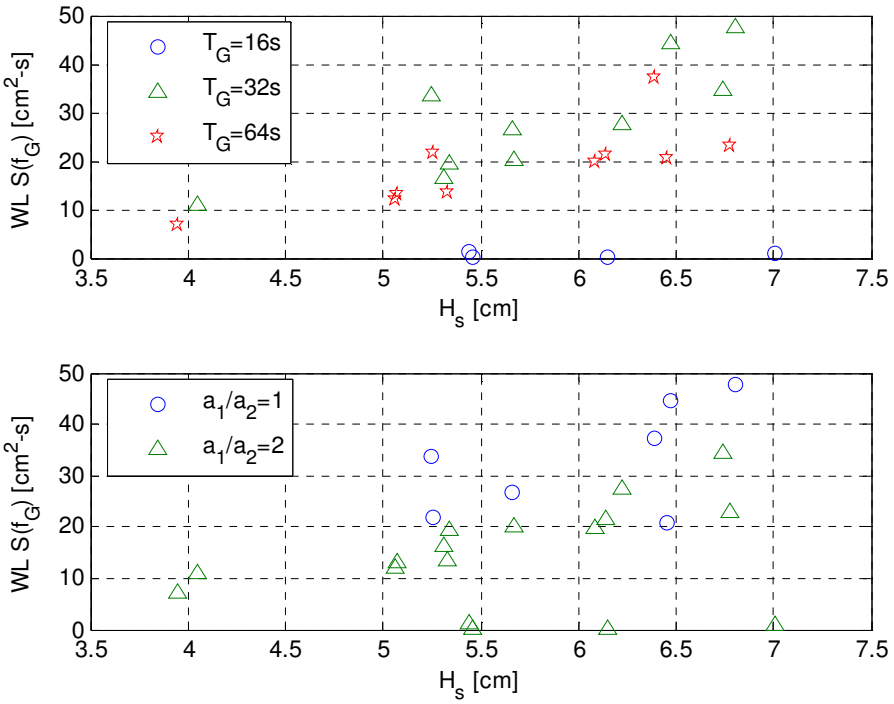

Figure 4.16: Spectral energy of the trough water levels (F series – ($x = 11.4$ m , $y = 12.3$ m) and H series – ($x = 11.76$ m , $y = 12.33$ m)) at the group frequency against the significant wave height for different groupings of wave group period (top) and amplitude ratio (bottom)

For the water levels, it is clear that the most energetic frequency is the wave group frequency, but the magnitude of that spectral energy may vary spatially. Figure 4.18 shows the spectral energy at the wave group frequency for the trough wave gauges as a function of their longshore position. Notice that the energy of the group frequency for the three gauges in the channel have less energy than the three gauges in the trough behind the bars. This indicates that the channel area is less responsive to the wave groups than the areas in the trough.

Since it is evident that the rip current system responds to the wave groups, cross-correlations between the wave group envelope and other features can indicate the temporal relationships between the different properties. To define a time-series of the

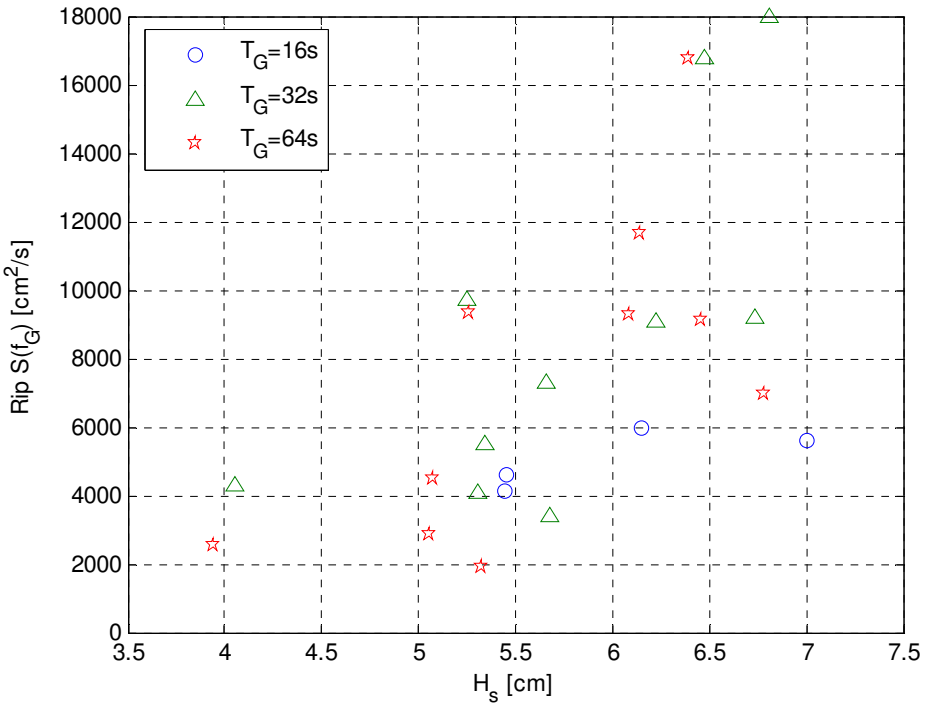

Figure 4.17: Spectral energy of the rip current at the group frequency against the significant wave height for different groupings of wave group period

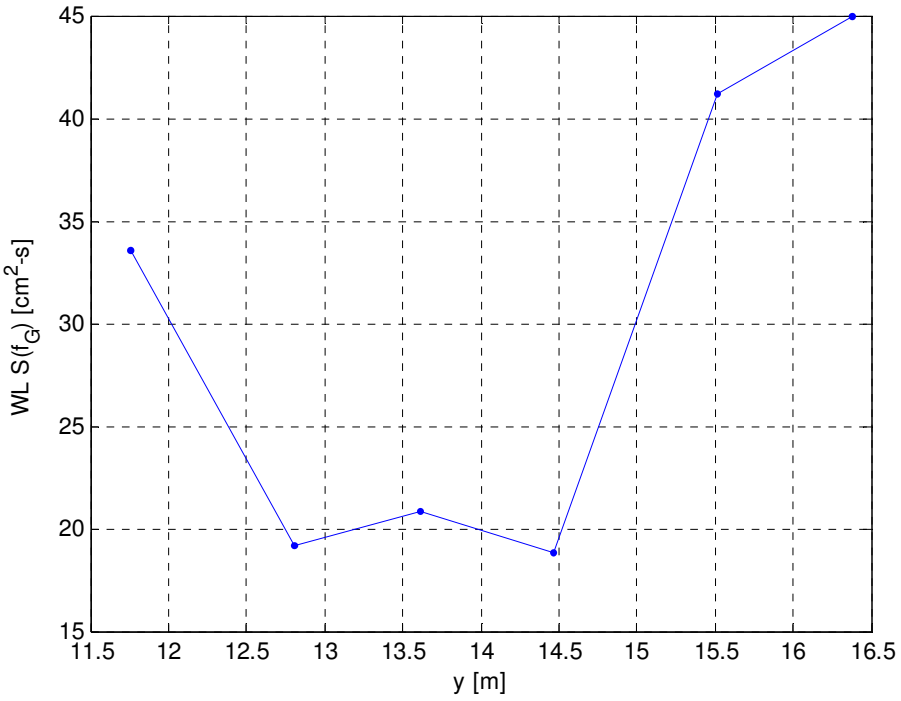

Figure 4.18: Energy of the water levels at the group frequency for a series of trough wave gauges located at different longshore positions (channel center-line at y = 13.66 m)

wave group envelope, a Hilbert-Transform is applied to the trough water level time-series. Cross-correlations between this envelope time-series and the other features of the rip current system produces phase lag information. The phase lags (ϕ) for a given frequency (f) are converted into time lags (Δt) by the equation given as

$$\Delta t = \frac{\left(\phi / 2\pi\right)}{f}. \tag{4-1}$$

The time lags corresponding to the wave group frequency are used to investigate the temporal relationships of the mechanisms in a rip current system. Each reported time lag relative to the peak of the wave group envelope is the time that is takes to reach a maximum.

The time lags for the side of dominant circulation are determined for 13 cases: two 16-s, six 32-s, and five 64-s wave group tests. These 13 tests are the experiments in which the water levels and velocities were measured for the dominant circulation side. The average and range of the time lags for each wave group is shown graphically in Figure 4.19 with the blue line (average) and red bar (range). In general, the pressure gradients form first and the currents respond later due to an inertial lag. The wave group period seems to have an effect on the lag of the pressure gradients; increasing the wave group period increases the longshore pressure gradient lag and decreases the cross-shore pressure gradient lag. The feeder and turning currents respond slower to the wave groups; they develop into a maximum around 5 s after the wave group for all wave groups. Interestingly the turning currents develop into a maximum before the feeder currents in both the 16- and 32-s wave groups. This might indicate that the rip first forms locally in the channel due to discontinuity in energy dissipation prior to the pressure

gradient driven flow as described by Kennedy (2003). Also, the rip lag for the 32-s wave group peaks at around 10 s from the wave group pulse, whereas both the 16- and 64-s wave groups lag the group at around 13 s.

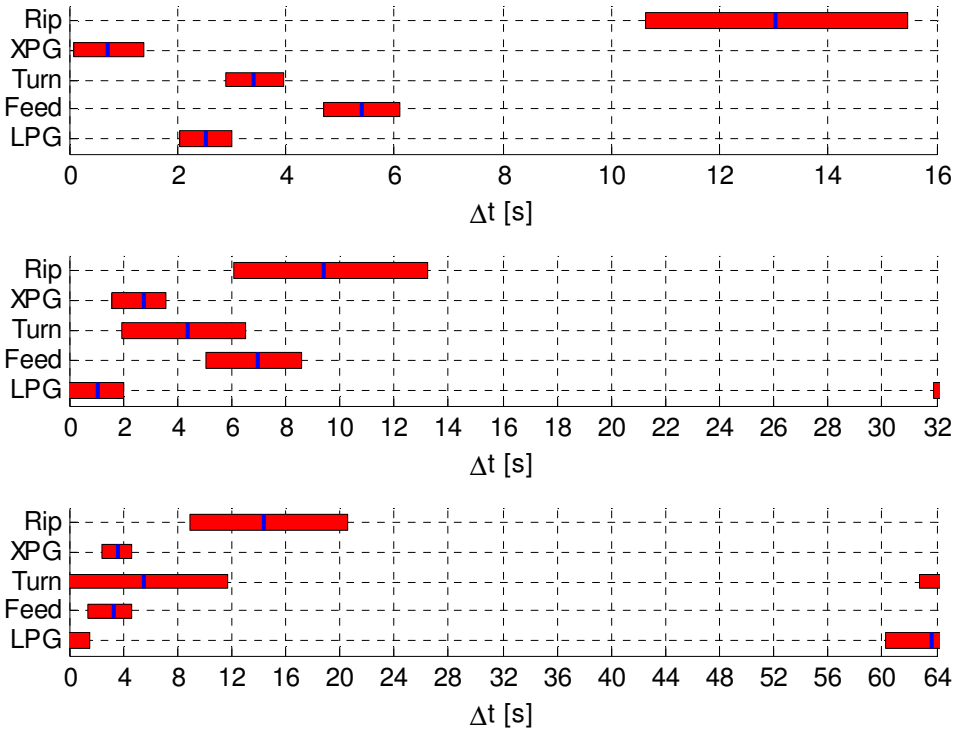

Figure 4.19: Average (blue line) and range (red bar) of time lags for 16-s (top), 32-s (middle), and 64-s (bottom) wave groups (LPG – longshore pressure gradient, Feed – feeder current, Turn – turning current, XPG – cross-shore pressure gradient, Rip – rip current)

4.2.2 Characterization of Low-Frequency Pulse

Of the three energetic frequencies, the low-frequency pulsation is the most interesting and the most difficult to understand. These low-frequency energy peaks in the spectra show up in both monochromatic and groupy condition. However in some tests, there is no evidence of low-frequency energy peaks. Table 4.1 lists the observed low frequencies evident in the in situ spectra.

Table 4.1: Energetic low-frequencies evident in spectra

In Situ Tests	T [s]	T_G [s]	Observed frequency [Hz]
F9	2	--	0.0085
F14 H2	1.33	32	0.005 0.006
F16	1.5	16	0.0055
F17	1.5	32	0.0043
F19	2	16	0.0122
F20 H5	2	32	0.0024 0.0024
F22	1	32	0.0024
F23 H11	1.33	32	0.01 0.011
H4	2	--	0.007
H6	2	64	0.004
H7	1.33	--	0.023
H8	1.33	--	0.01221
H9	1.33	32	0.005
H12	1.33	64	0.004
H13	2	32	0.004

By using 60-s time averages of the video data, as shown for test I6 in Figure 4.20, visual evidence of this low-frequency pulsation is seen as meandering of a rip current circulation cell. The top velocity field shows a right dominant circulation cell at $t = 0$ s. After 60 s, it appears the rip system is in transition with a detached eddy offshore. At the next time-average corresponding to $t = 120$ s, the circulation cell is now dominant on the left side. This meandering of the rip is visible throughout the video segment for I6 and goes back and forth for a complete cycle on the order of 200 – 250 s, which closely corresponds to the low-frequency energy peaks in the spectra.

The video experiments are used to compute the acceleration normal to the rip velocity. This acceleration is a measure of the turning of a drifter. The energy spectrum of this turning acceleration of a drifter is computed for I6 (video test of H13) using 4 degrees of freedom and a Hanning window. The spectrum, shown in Figure 4.21, shows

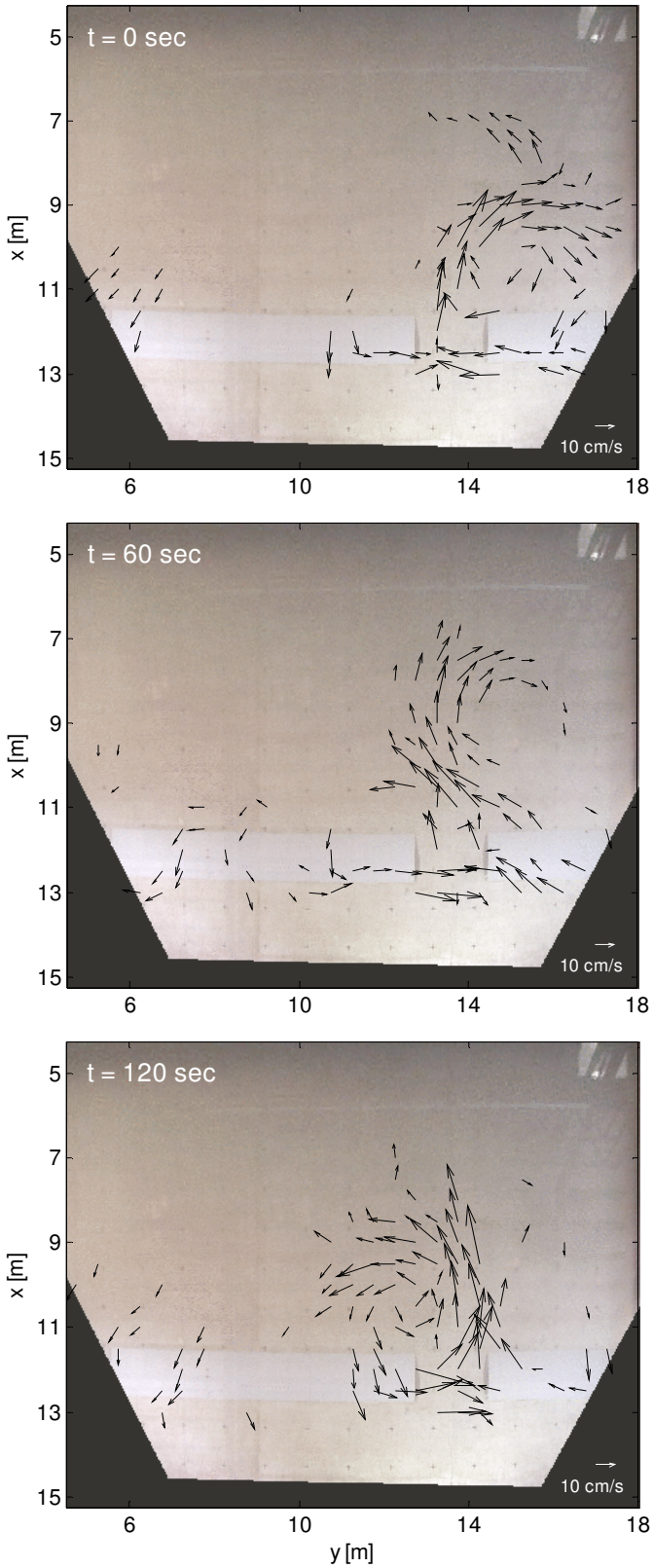

Figure 4.20: Velocity fields of 60-s time averages showing circulation cell meandering in experiment I6

most of the spectral energy at the low frequency corresponding to the 0.04 Hz seen in the instrument spectra. This indicates that this long-period pulsation is related to the turning of the rip current.

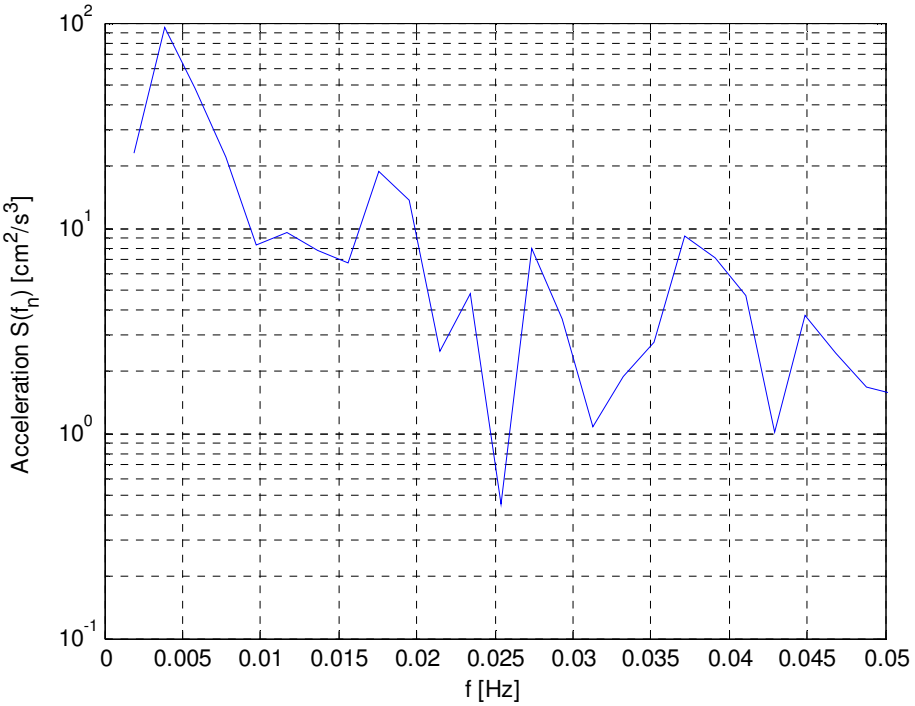

Figure 4.21: Frequency spectrum of radial acceleration of a drifter in the rip channel from experiment I6 centered at ($x = 10.5$ m , $y = 13.66$ m) with a 1 m x 1 m bin

It is logical that the meandering of the rip back and forth creates a response in the longshore direction of the channel as evident in the spectra of the turning and rip currents. It also seems viable that the rip strength may not be as sensitive to a change in circulation sides, which is why the low-frequency pulsations are not as dominant in the cross-shore component of the rip velocity. The outward-directed longshore pressure gradient also has a strong response at this low-frequency, which is also explained by the meandering. During a right dominant circulation, as shown in the top of Figure 4.20, the convergence

of the feeders is on the left side of the center-line. Alternatively for the left dominant circulation, as shown in the bottom of Figure 4.20, the convergence area is on the right side of the center-line. The moving of this convergence area as the rip meanders back and forth affects the water level around the bar corners since the water level increases near the convergence and decreases near the center of circulation. Since the water level in the center of the channel is more constant during this meandering, the oscillations in the water level near the bar create a low-frequency response in the outward-directed longshore pressure gradients. Therefore the low-frequency energy is related to the circulation direction of the rip through this meandering effect.

To obtain a better physical understanding of this low-frequency meandering, the in situ data is investigated to determine how the other features respond during a change in rip direction. Shown in Figure 4.22 is a sequence of snapshots with increments of 32 s of the low-passed (frequency cut-off 0.05 Hz) in situ measurements for test H13. The top subfigure in each snapshot demonstrates the cross-shore water level difference in the channel by the lengths of the upper and lower sides of the quadrilateral with the vector representing the cross-shore pressure gradient. The mid subfigure gives the velocity field as vectors at each ADV location. The bottom subfigure shows a longshore cross-section of the water level with vectors for the longshore pressure gradients driving the feeders. Since the increment between each snapshot is 32 s (wave group frequency), the snapshots show the flow conditions at the peak of each wave group. Notice that the turning currents change from being stronger on the left at 122 s to stronger on the right at 250 s and back to left at 346 s. This corresponds to the low-frequency pulsation observed in the spectra. Also note that the water surface near the channel seems to be sloshing back

and forth. The water surface goes from a positive slope to a zero slope to a negative slope from 122 to 218 s and then continually more positive until 346 s. This sloshing changes the longshore pressure gradient dramatically, as seen by the left dominant gradient at 122 s and the right dominant gradient at 218 s. It is also apparent that the cross-shore pressure gradient is less affected by this sloshing motion as it is more constant. Also, consistent with previous observations, the feeder currents look more constant than the turning currents indicating the lack of low-frequency response in the feeders. The magnitudes of the velocities in the rip also appear less affected by the low-frequency but there is evidence in the longshore component of the rip by the direction change.

4.3 Possible Sources of Low-Frequency Pulsation

After viewing the physical characteristics of the low-frequency pulsations, possible mechanisms are explored. The characteristics of the low-frequency pulsation indicate that it is associated with the direction of the rip as meandering. This meandering back and forth of the rip in a long-period cycle could be caused from basin seiching, circulation cell instabilities, wave-current interaction, or some combination of these.

4.3.1 Wave Basin Seiching

Basin seiching is the oscillation of a body of water at its natural frequency when excited by some external forcing. Both wave reflection and wave groupiness can excite seiche modes during wave generation in an enclosed basin, which transfers energy to lower frequencies.

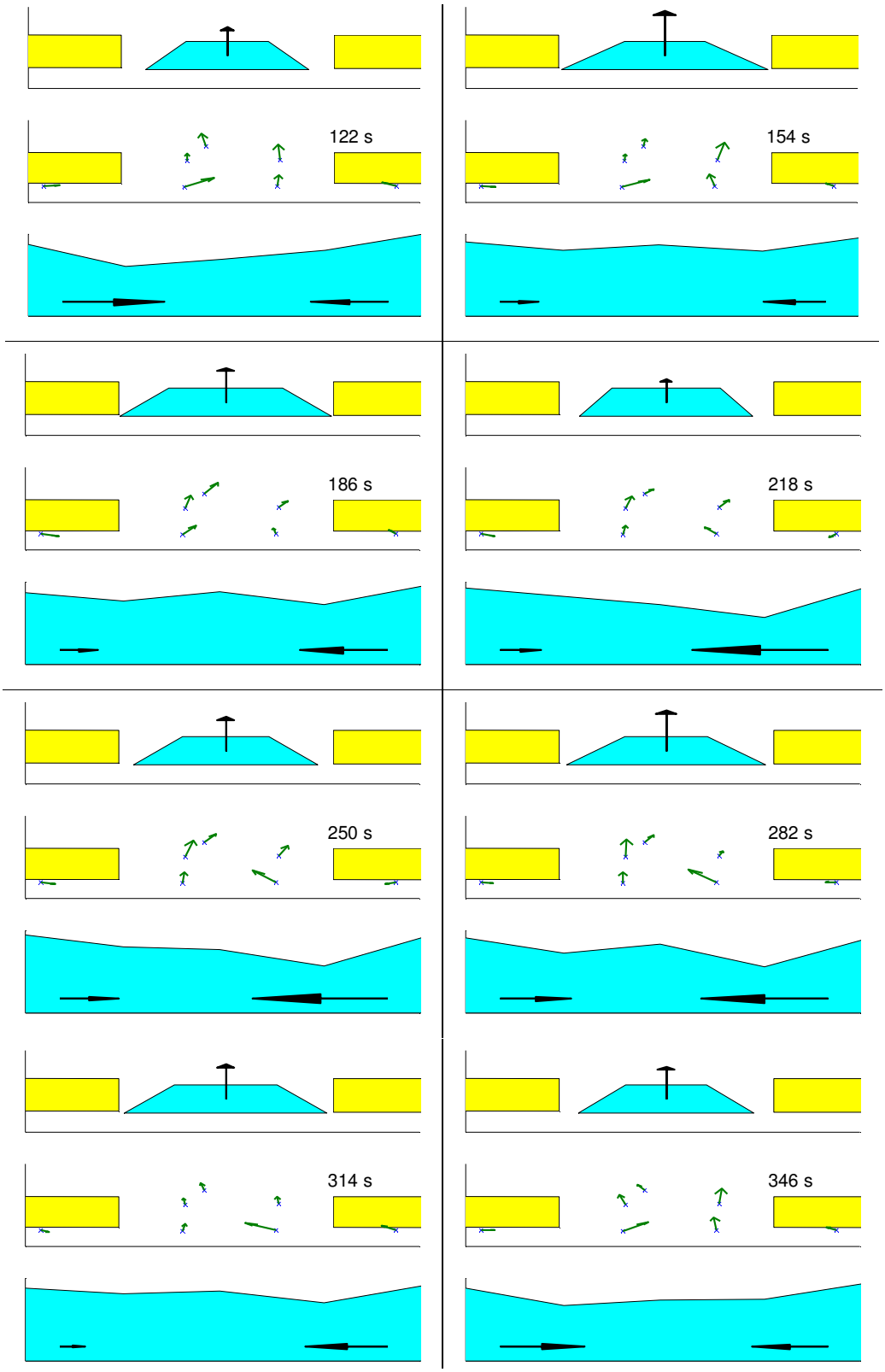

Figure 4.22: Snapshots of the in situ measurements for experiment H13 with increments of 32 s (wave group frequency) with each snapshot giving the cross-shore pressure gradient (top), velocity vectors (middle) and longshore pressure gradients (bottom)

Haller and Dalrymple (1999) calculated seiching periods for several modes of the University of Delaware wave basin with the same water depth as these tests. Listed in Table 4.2 are the seiching periods for the 5 largest-period modes, where n and m are the number of zero-crossings in the longshore and cross-shore standing waves, respectively. The seiche mode with the largest period is of interest since an energy peak corresponding to a period of 28 s does exist in the spectra of the turning currents in the channel. It could be that the seiching period is interacting with the group frequency to produce the low-frequency pulsation, which is the difference frequency between the seiching and the group frequency. However, evidence of seiching in the basin would be found as energy in the water levels. The spectra for the water levels do not show any significant energy peaks around 28 s, as is seen in Figures 4.3 and 4.9. Also, the fact that the low frequency peaks in the spectra occur for monochromatic test cases rule out the interaction of the seiching frequency with the group frequency as a source since there is no wave group. It is believed that the cause of this low-frequency pulsation is not related to seiching.

Table 4.2: Seiching periods and frequencies calculated in Haller and Dalrymple (1999) for 70.36 cm offshore water depth

T (s)	T^{-1} [Hz]	n,m
27.8	0.036	1,0
22.9	0.044	0,1
19.7	0.051	2,0
16.4	0.061	1,1
16	0.063	4,0

4.3.2 Circulation Cell Instability

The instability of rotating flows, such as these circulation cells, was considered by Rayleigh (1880, 1916) in which he developed Rayleigh's circulation criterion. The criterion states that for hydrodynamic stability of a circulating flow to axisymmetric disturbances, the circulation must radially increase. However, if the circulation radially decreases anywhere in the flow, the inward-directed pressure gradient is unable to stabilize the outward-directed centrifugal force.

The circulation cell velocities measured from the drifter tracks are used to calculate the circulation as a function of the radius from the cell center. The measured circulation (blue) from I6 is shown in Figure 4.23 along with the circulations from the model fits (red). Both the measurements and model show a radial decrease in circulation, which indicates possible instability. For circulation cells in other tests, most show a radial decrease in circulation, but a few cells have insufficient drifter coverage to conclude if a decrease exists or not. It is expected that all of the cells have a radial decrease in circulation, but more research is needed to explain if the 15 cases that have low-frequency energy evident in the spectra are related to possible instabilities and why other cells are stable if the circulation is decreasing radially.

4.3.3 Other Mechanisms

Other mechanisms for possible sources of this low-frequency pulsation are rip jet instabilities and wave-current interaction. Haller and Dalrymple (2001) investigate rip jet instabilities as an explanation of rip current oscillations. The mechanism of wave-current interaction in a rip current system causing pulsations is discussed in Haas et al. (2003).

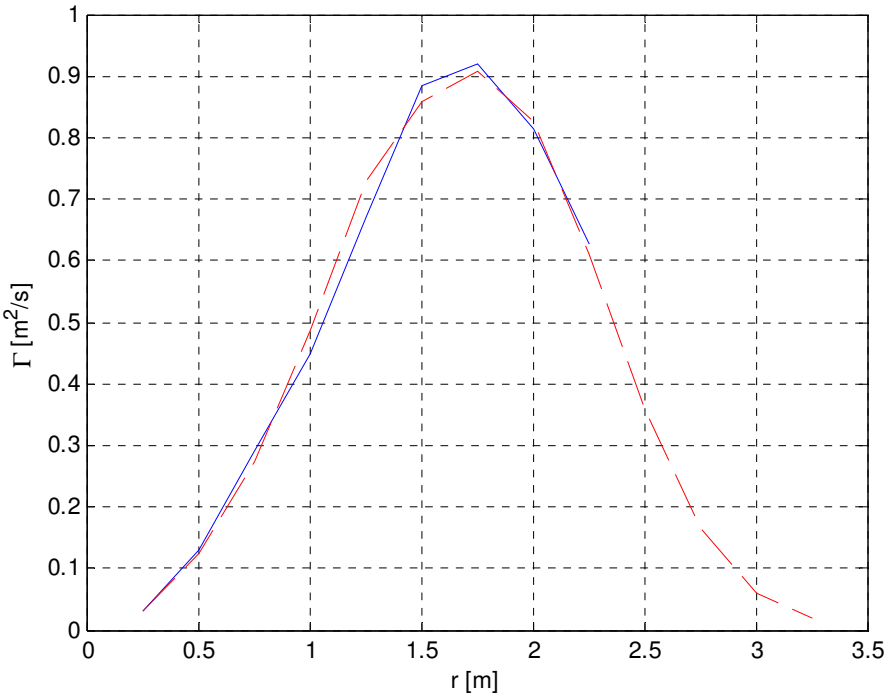

Figure 4.23: Measured (solid) and modeled (dashed) circulation of a circulation cell in experiment I6

Haller and Dalrymple (2001) estimate the frequencies of the fastest growing mode from the stability analysis of a Bickley-jet model calibrated by laboratory measurements. The most unstable frequency ranged from 0.010 – 0.032 Hz for their deeper water experiments. Using the same analysis, video measurements of I6 are used to calibrate the Bickley-jet model for the linear stability analysis, which gave 0.014 Hz as the frequency of the fastest growing mode. This frequency is not on the same order as the low frequency pulse around 0.004 – 0.005 Hz or the interaction frequency of 0.036 Hz for this case. If this rip jet instability mechanism produces a change in rip direction, it would produce a spectral energy peak at half of the most unstable frequency in the longshore velocity in order to complete the cycle from right to left then back to right. In this case, a spectral energy peak of around 0.007 Hz would be evident in the longshore velocity.

However, the low-frequency pulsation is primarily observed in the area of feeder convergence. For rip jet instability, the pulsations should be more energetic at the exit of the channel than in the convergence area. The rip instability mechanism does not explain the low-frequency pulsations observed in these experiments.

A description of wave-current interaction causing rip current pulsations is given in Haas et al. (2003). As the rip current exits the channel, the offshore currents increase the wave height as seen by red color at the rip exit in the mean wave height field shown in Figure 4.24. This increase in wave height both strengthens the opposing force against the rip current and weakens the rip current forcing, hence weakening the rip. As the rip weakens, the wave height at the exit of the channel decreases which allows the rip current to strengthen again.

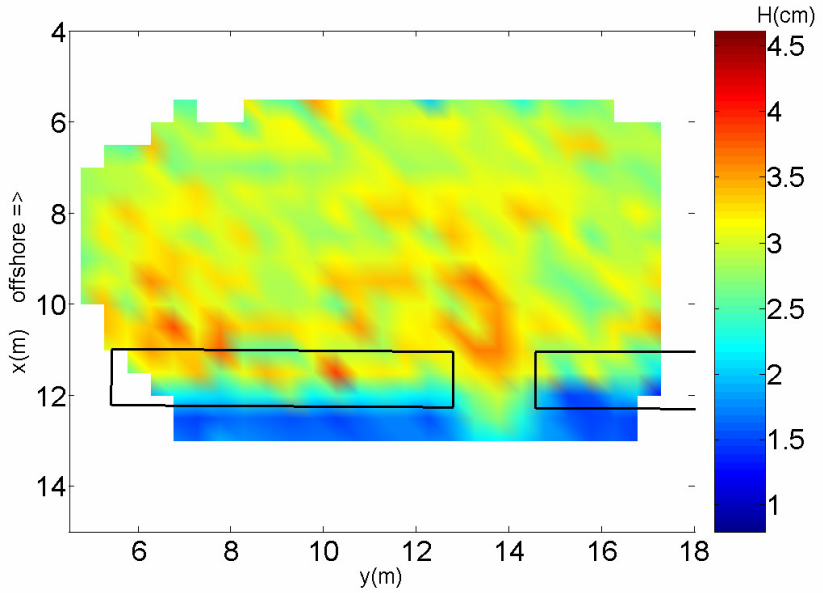

Figure 4.24: Mean wave-height field for experiment I6 showing increase in wave height at rip exit

This cycle of rip current strengthening and weakening due to the wave-current interaction may be a source of the low-frequency pulsations observed in the measurements. One issue of concern is that the long-period oscillations in the measurements are characterized as a meandering of the rip back and forth, whereas wave-current interaction is a strengthening and weakening effect. However, observations from Chapter 3 show that weaker rips are more likely to meander. Therefore, it is possible that by weakening the rip current it changes direction and during strengthening it is more stable. To justify the wave-current interaction as the cause of this low-frequency motion, time-varying cross-shore momentum balances are required. These experiments, although providing extensive spatial coverage, lack sufficient time-varying coverage to investigate this effect further as a possible source for the low-frequency pulsations.

CHAPTER 5
CONCLUSIONS

From the first observation of rip currents to recent studies, the understanding of rip currents is continually improving. Although much remains unknown, the acquired knowledge has increased the public awareness of rip currents and aided in a better understanding of the nearshore sediment transport budget. This thesis compliments the past studies by analyzing both mean and time-varying properties in a rip current system in a laboratory setting for a variety of wave conditions.

The Ocean Engineering Laboratory at the University of Delaware has been the site for rip current experiments for several years. This set of experiments adds to the other laboratory studies by providing a spatially large and time-varying perspective of the rip current system as a whole. Both in situ and optical measurements using Lagrangian drifters are used to measure the rip current system.

The optical drifter tracking involves three steps: identifying the particles in an image, transforming the image coordinates into a real-world coordinate system, and linking the individual coordinates into tracks. The particle identification algorithm is automated using MATLAB code and is based on the contrast-intensity and size of a drifter. Transformation of the coordinates into a real-world coordinate system is completed using the Direct Linear Transformation (DLT) technique of Holland et al. (1997). For linking the drifters into tracks, a strict nearest-neighbor approach was used. Possible sources of error in the tracking method are investigated and found to be primarily high-frequency in nature, which are shown to be greatly reduced with low-pass

filters. Corrections for other errors, such as lens distortion and the apparent horizontal motion from the vertical motion of a drifter, are applied.

Both Lagrangian velocities and wave heights are calculated from the drifter tracks. Lagrangian velocities are calculated from the low-pass drifter tracks and wave heights are calculated using Linear Wave Theory and the orbital motion of the drifters isolated with a band-pass filter. The accuracy of the velocity and wave height measurements of the drifters is analyzed using simultaneous optical/in situ measurements in a flume and found to be 2% for mean velocity and 3.0 – 17.3% for wave height measurements. Although not simultaneous, the mean measurements of drifters are compared to the in situ measurements from basin tests of the same wave conditions. The RMS velocity errors from these comparisons range from 1.3 – 5.7 cm/s depending on the drifter coverage and spatial variability of the area. The wave height calculations gave a RMS error of 8.2 mm and the errors are less dependent on location.

Using drifter and in situ measurements, the effect of the various wave conditions on the mean rip system properties are investigated. It is found that increasing the mean wave height increases the wave setup, the feeder current of the dominant side, the flow speed at the turn in the channel, the cross-shore pressure gradient, and the rip speed.

Using the drifter measurements, the circulation cells of the rip current system are compared for different wave conditions. Circulation cells are observed to vary in size and strength for different wave conditions. A circulation cell model of the mean velocity field is developed that describes the general trend of the cells. It is found that the cell has a strong, narrow current on the rip side and is broad and weaker on the opposite side of the cell. It is found that the circulation in a cell increases radially and then decreases

exponentially. For increasing wave height, the circulation cells have higher velocites, are further offshore, and produce stronger overall circulations. Also, it is found that the large waves produce asymmetric rip systems, whereas the smaller waves gave the more symmetric systems. It is observed that the most symmetric mean systems are the cases in which the rip meanders back and forth throughout the video segment.

To investigate the pulsation behavior of rip current systems, spectral techniques are used to determine the frequencies of high spectral energy. Three different types of frequency peaks are found to be energetic in the frequency band below the incident wave frequency: the wave group frequency, a low-frequency, and the interaction frequency of the wave group and the low-frequency. The wave group pulse is evident in the bi-chromatic test cases to strengthen and weaken the rip current system. The low-frequency pulse is related to the direction of the rip as it meanders back and forth. The low-frequency pulse is evident in the area where the feeder currents converge and turning offshore for both monochromatic and bi-chromatic cases. The interaction frequency was evident when both the wave group and low-frequency peaks are energetic. Possible sources of the low-frequency meandering of the rip are investigated including wave basin seiching, circulation cell instabilities, rip jet instabilities, and wave-current interaction. Seiching and rip jet instabilities were discounted as possible sources but further research is needed to determine if circulation cell instability or wave-current interaction is producing this low-frequency meandering.

The wave conditions used for these experiments scale to normal field conditions with a 1:10 geometry scale and a $1:\sqrt{10}$ time scale. The experimental range of wave heights, 5 – 10 cm, scale to 0.5 – 1 m waves in the field. Experimental wave periods of 1

– 2 s scale to more realistic periods of 3.2 to 6.3 s in the field. Wave group periods of 16, 32, and 64 s used in the laboratory experiments scale to typical field condition wave groups of 45 s, 1.7 min, and 3.3 min. The average rip speeds measured in the laboratory range from 5 – 35 cm/s, which scales from a weak 15 cm/s current to a stronger 1.1 m/s current in the field. The observed laboratory low-frequency pulsations ranging from 80 – 500 s scale to a 4 – 26 minute range pulsation for real-world rip current systems. Some field observations by Callaghan et al. (2004) from Moreton Island, Australia report pulsations of 10 – 20 minutes. It is possible that these field-observed pulsations are generated by a similar mechanism as these laboratory observations.

Although this study on rip currents analyzes several aspects of these laboratory measurements, there is much to discover within this data set. One recommendation for future studies is to use a wavelet analysis instead of the Fast Fourier Transform (FFT) for analyzing energetic frequencies. A wavelet analysis would resolve pulsations with frequencies that are time-varying. Another recommendation is to perform a linear stability analysis on the circulation cell model developed in this thesis to determine if this provides further support for this to be the cause of the low-frequency motion. To investigate the wave-current interaction as a possible source of the low-frequency energy, detailed momentum balances should be calculated to determine the force responsible for the turning of the rip current.

REFERENCES

Aagaard, T., Greenwood, B., and Nielsen, J. (1997). Mean currents and sediment transport in a rip channel. *Journal of Marine Geology*, **140**, 25-45.

Adamczyk, A.A. and Rimai, L. (1988). 2-Dimensional particle tracking velocimetry (PTV): technique and image processing algorithms. *Experiments in Fluids*, **6**(6), 373-380.

Adrian, R.J. (1991). Particle-imaging techniques for experimental fluid mechanics. *Annual Review of Fluid Mechanics*, **23**, 261-304.

Allen, J.R., and Psuty, N.P. (1987). Morphodynamics of a single-barred beach with a rip channel, Fire Island, New York. In *Proc. Coastal Sediments '87*, 1964-1975.

Arthur, R.S. (1962). A note on the dynamics of rip currents. *Journal of Geophysical Research*, **67**, 2777-2779.

Bowen, A.J. (1969). Rip currents. 1. Theoretical investigations. *Journal of Geophysical Research*, **74**, 5467-5478.

Bowen, A.J. and Inman, D.L. (1969). Rip currents. 2. Laboratory and field observations. *Journal of Geophysical Research*, **74**, 5479-5490.

Bowman, D., Arad, D., Rosen, S., Kit, E., Goldbery, R., and Slavicz, A. (1988a). Flow characteristics along the rip current system under low-energy conditions. *Journal of Marine Geology*, **82**, 149-167.

Bowman, D., Rosen, S., Kit, E., Arad, D., and Slavicz, A. (1988b). Flow characteristics at the rip current neck under low energy conditions. *Journal of Marine Geology*, **79**, 41-54.

Bowman, D., Birkenfeld, H., and Rosen, D.S. (1992). The longshore flow component in low-energy rip channels: The Mediterranean, Israel. *Journal of Marine Geology*, **108**, 259-274.

Brander, R.W. (1999a). Field observations on the morphodynamic evolution of a low-energy rip current system. *Journal of Marine Geology*, **157**, 199-217.

Brander, R.W. (1999b). Sediment transport in low-energy rip current systems. *Journal of Coastal Research*, **15**(3), 839-849.

Brander, R.W. (2000). Measurements of flow velocity and sediment transport in a rip current. In *Proc. 27th Coastal Engeering Conference*, 3395-3408.

Brander, R.W. and Short, A.D. (2000). Morphodynamics of a large-scale rip current system at Muriwai Beach, New Zealand. *Journal of Marine Geology*, **165**, 27-39.

Brander, R.W. and Short, A.D. (2001). Flow kinematics of low-energy rip current systems. *Journal of Coastal Research*, **17**(2), 468-481.

Brocchini, M., Kennedy, A.B., Soldini, L., and Mancinelli, A. (2003). Topographically-controlled, breaking-wave induced macrovortices. 1: Widely separated breakwaters. *Journal of Geophysical Research*, **507**, 289-307.

Bühler, O. and Jacobson, T.E. (2001). Wave-driven currents and vortex dynamics on barred beaches. *Journal of Fluid Mechanics*, **449**, 313-339.

Callaghan, D., Baldock, T., Nielson, P., Hanes, D., Haas K., and MacMahan, J. (2004). Pulsing and circulation in rip current system. In *Proc. 29th Coastal Engineering Conference*, 1493-1505.

Caruthers, J.W., Stanic, S.J., Elmore, P.A., and Goodman, R.R. (1999). Acoustic attenuation in very shallow water due to the presence of bubbles in rip currents. *The Journal of the Acoustical Society of America*, **106**(2), 617-625.

Chandramohan, P., Kumar, V.S., and Jena, B.K. (1997). Rip current zones along beaches in Goa, west coast of India. *Journal of Waterway, Port, Coastal and Ocean Engineering*, **123**, 322-328.

Chen, Q., Dalrymple, R.A., Kirby, J.T., Kennedy, A.B., and Haller, M.C. (1999). Boussinesq modeling of a rip current system. *Journal of Geophysical Research*, **104**, 20617-20637.

Cook, D.O. (1970). The occurrence and geological work of rip currents off Southern California. *Journal of Marine Geology*, **9**, 173-186.

Cowen, E.A. and Monismith, S.G. (1997). A hybrid digital particle tracking velocimetry technique. *Experiments in Fluids*, **22**(3), 199-211.

Craig, W., Brant, I., Hite, M.P., and Davis, W.M. (1925). The "Undertow". *Science*, **62**, 30-33.

Dalrymple, R.A. (1975). A mechanism for rip current generation on an open coast. *Journal of Geophysical Research*, **80**, 3485-3487.

Dalrymple, R.A. (1979). Rip currents and their causes. In *Proc. 16th Coastal Engineering Conference*, 1414-1427.

Dalrymple, R. (1989). Directional wavemaker theory with sidewall reflection. *Journal of Hydraulic Research,* **27**, 23-34.

Dalrymple, R.A. and Lozano, C.J. (1978). Wave-current interaction models for rip currents. *Journal of Geophysical Research*, **83**, 6063-6071.

Davis, R.E. (1985). Drifter observations of coastal surface currents during CODE: the method and descriptive view. *Journal of Geophysical Research*, **90**, 4741-4755.

Davis, W.M. (1925a). The undertow myth. *Science*, **61**, 206-208.

Davis, W.M. (1925b). Undertow and rip tides. *Science*, **73**, 526-527.

De Vriend, H.J. and Stive, M.J.F. (1987). Quasi-3D modelling of nearshore currents. *Coastal Engineering*, **11**, 565-601.

Deguchi, I., and Araki, S. (2004). Rip current measured at Uradome Beach Tottori, Japan. In *Proc. 29th Coastal Engineering Conference*, 1519-1531.

Deigaard, R. (1990). The formation of rip channels on a barred coast. Technical Report 72, Technical University of Denmark.

Dette, H.-H., Peters, K., and Spignant, F. (1995). About rip currents at a mesotidal coast. In *Proc. Coastal Dynamics '95*, 477-488.

Drønen, N., Karunarathna, H., Fredsøe, J., Sumer, B.M. and Deigaard, R. (1999). The circulation of a longshore bar with rip channels. In *Proc. Coastal Sediments '99*, 576-587.

Drønen, N., Karunarathna, H., Fredsøe, J., Sumer, B.M. and Deigaard, R. (2002). An experimental study of rip channel flow. *Coastal Engineering*, **45**, 223-238.

Engle, J., MacMahan, J., Thieke, R.J., Hanes, D.M., and Dean, R.G. (2002). Formulation of a rip current predictive index using rescue data. In *Proc. National Conference on Beach Preservation Technology*, Florida Shore and Beach Preservation Association, Biloxi.

Etoh, T. and Takehara, K. (1992). An algorithm for tracking particles. In *Proc. 6th International Symposium on Stochastic Hydraulics*.

Fage, A. and Townend, H.C.H. (1932). Turbulent motion near a wall. In *Proc. Royal Society of London*, Series A, 135, 656-677.

Falqués, A. and Montoto, A., and Vila, D. (1999). A note on hydrodynamic instabilities and horizontal circulation in the surf zone. *Journal of Geophysical Research*, **104**, 20605-20615.

Feddersen, F. and Guza, R.T. (2003). Observations of nearshore circulation: Alongshore uniformity. *Journal of Geophysical Research*, **108**(C3).

Frieden, B.R. and Zoltani, C.K. (1989). Fast tracking algorithm for multiframe particle image velocimetry data. *Applied Optics*, **28**, 652-655.

Haas, K.A., and Svendsen, I.A. (2000). Three-dimensional modeling of rip current systems. Research Report CACR-00-06. Center for Applied Coastal Research, University of Delaware.

Haas, K.A., and Svendsen, I.A. (2002). Laboratory measurements of the vertical structure of rip currents. *Journal of Geophysical Research*, **107**(C5).

Haas, K.A. Svendsen, I.A., Brander, R.W. and Nielson, P. (2002). Modeling of a rip currents system on Moreton Island, Australia. In *Proc. 28th Coastal Engineering Conference*.

Haas, K.A., Svendson, I.A., Haller, M.C., and Zhao, Q. (2003). Quasi-three-dimensional modeling of rip current systems. *Journal of Geophysical Research*, **108**(C7).

Haller, M.C. (1998). Spectral analysis of wave and current measurements in a rip current system. CIEG 681.

Haller, M. and Dalrymple, R.A. (1999). Rip current dynamics and nearshore circulation. Research Report CACR-99-05, Center for Applied Coastal Research, University of Delaware.

Haller, M.C. and Dalrymple, R.A. (2001). Rip current instabilities. *Journal of Fluid Mechanics*, **433**, 161-192.

Haller, M., Dalrymple, R., and Svendsen, I.A. (1997a). Rip channels and nearshore circulation. In *Proc. Coastal Dynamics '97*, 594-603.

Haller, M., Dalrymple, R., and Svendsen, I.A. (1997b). Experimental modeling of a rip current system. In *Proc. Of the Third International Symposium on Ocean Wave Measurement and Analysis*.

Haller, M.C., Dalrymple, R.A., and Svendsen, I.A. (2000). Experiments on rip currents and nearshore circulation: Data report. Technical Report CACR-00-04, Center for Applied Coastal Research, University of Delaware.

Haller, M.C., Dalrymple, R.A., and Svendsen, I.A. (2002). Experimental study of nearshore dynamics on a barred beach with rip channels. *Journal of Geophysical Research*, **107**(C6).

Haller, M.C. and Özkan-Haller, H.T. (2002). Wave breaking and rip current circulation. In *Proc. 28th Coastal Engineering Conference*, 705-717.

Hering, F., Leue, C., Wierzimok, D., and Jähne, B. (1997a). Particle tracking velocimetry beneath water waves. Part I: visualization and tracking algorithms. *Experiments in Fluids*, **23**(6), 472-482.

Hering, F., Merle, M., Wierzimok, D., and Jähne, B. (1997b). A robust technique for tracking particles over long image sequences. In *Proc. of ISPRS Intercommission Workshop 'From Pixels to Sequences'*.

Hesselink, L. (1988). Digital image processing in flow visualization. *Annual Review of Fluid Mechanics*, **20**, 421-485.

Hino, M. (1974). Theory and formation of rip-current and cuspidal coast. In *Proc. 12th Coastal Engeering Conference*, 901-919.

Holland, K.T., Holman, R.A., Lippmann, T.C., Stanley, J., and Plant, N. (1997). Practical use of video imagery in nearshore oceanographic field studies. *IEEE Journal of Oceanic Engineering*, **22**(1).

Huntley, D.A. and Short, A.D. (1992). On the spacing between observed rip currents. *Coastal Engineering*, **17**, 211-225.

Huntley, D.A., Hendry, M.D., Haines, J., and Greenridge, B. (1988). Waves and rip currents on a Caribbean pocket beach, Jamaica. *Journal of Coastal Research*, **4**, 69-79.

Iwata, N. (1976). Rip current spacing. *Journal of Oceanographic Society of Japan*, **32**, 1-10.

Johnson, D. and Pattiaratchi, C. (2004). Transient rip currents and nearshore circulation on a swell-dominated beach. *Journal of Geophysical Research*, **109**.

Kennedy, A.B. (2003). A circulation description of a rip current neck. *Journal of Fluid Mechanics*, **497**, 225-234.

Kennedy, A.B. and Kirby, J.T. (2003). An unsteady wave driver for narrowbanded waves: modeling nearshore circulation driven by wave groups. *Coastal Engineering*, **48**, 257-275.

Kennedy, A.B. and Thomas, D. (2003). Drifter measurements in a laboratory rip current. *Journal of Geophysical Research*, **109**.

Lascody, R.L. (1998). East Central Florida rip current program. *National Weather Digest*, **22**(2), 25-30.

Lauterborn, W. and Vogel, A. (1984). Modern optical techniques in fluid mechanics. Annual Review of Fluid Mechanics, **16**, 223-244.

Lushine, J.B. (1991). A study of rip current drownings and related weather factors. *National Weather Digest*, **16**, 13-19.

MacMahan, J., Stanton, T., Thornton, E.B., and Reniers, A.J.H.M. (2005). RIPEX - Observations of a rip current system. *Journal of Marine Geology*, **218**, 113-134.

MacMahan, J., Reniers, A.J.H.M., Thornton, E.B., and Stanton, T. (2004a). Infragravity rip current pulsations. *Journal of Geophysical Research*, **109**.

MacMahan, J.H. Reniers, A.J.H.M., Thornton, E.B., and Stanton, T.P. (2004b). Surf zone eddies coupled with rip current morphology. *Journal of Geophysical Research*, **109**.

McKenzie, P. (1958). Rip current systems. *Journal of Geology*, **66**, 103-113.

Merzkirch, W. (1974). Flow visualization. Academic Press, Inc.

Miller, C. and Barcilon, A. (1978). Hydrodynamic instability in the surf zone as a mechanism for the formation of horizontal gyres. *Journal of Geophysical Research*, **83**(C8), 4107-4116.

Mizuguchi, M. (1976). Eigenvalue problems for rip current spacing. *Transactions of the American Society of Civil Engineers*, **148**, 83-88.

Murray, A.B. (2002). Rip channel development on non-barred beaches: the importance of a lag in suspended sediment transport. *Journal of Geophysical Research*, **109**.

Murray, A.B. and Reydellet, G. (2001). A rip-current model based on a hypothesized wave/current interaction. *Journal of Coastal Research*, **17**, 517-530.

Murray, A.B., LeBars, M., and Guillon, C. (2003). Tests of a new hyptothesis for nonbathymetrically driven rip currents. *Journal of Coastal Research*, **19**(2), 269-277.

Nielson, P., Brander, R.W., and Hughes, M.G. (2001). Rip currents: observations of hydraulic gradients, friction factors and wave pump efficiency. In Proc. *Coastal Dynamics '01*, 483-492.

Noda, E.K. (1974). Wave-induced nearshore circulation. *Journal of Geophysical Research*, **79**, 4098-4106.

Peregrine, D.H. (1998). Large-scale vorticity generation by breakers in shallow and deep water. *IUTAM Symposium on Three-dimensional Air-Sea Interactions*.

Peregrine, D.H. (1999). Surf zone currents. *Theoretical and Computational Fluid Dynamics*, **10**, 295-309.

Peregrine, D.H. and Bokhove, O. (1998). Vorticity and surf zone currents. In *Proc. 26th Coastal Engineering Conference*.

Perkins, R.J. and Hunt, J.C.R. (1989). Particle tracking in turbulent flows. In *Advances in Turbulence*, **2**, 286-291.

Rayleigh, L. (1880). On the stability, or instability, of certain fluid motions. In *Proc. London Mathematical Society*, **11**, 57-70.

Rayleigh, L. (1880). On the dynamics of revolving fluids. In *Proc. Royal Society of London*, A, **93**, 148-154.

Reniers, A., Thonton, E.B., Stanton, T.P., and MacMahan, J. (2002). RIPEX: Rip-current pulsation modeling. In *Proc. 28th Coastal Engineering Conference*

Sasaki, M. (1985). Velocity profiles in nearshore circulation current. *Coastal Engineering in Japan*, **28**, 125-136.

Schmidt, W.E., Woodward, B.T., Millikan, K.S., and Guza, R.T. (2003). A GPS-tracked surf zone drifter. *Journal of Atmospheric Science and Oceanic Technology*, **20**, 1069-1075.

Shepard, F.P. (1936). Undertow, rip tide or rip current. *Science*, **84**, 181-182.

Shepard, F.P. and Inman, D.L. (1950). Nearshore water circulation related to bottom topography and wave refraction. *Transactions, American Geophysical Union*, **31**, 196-212.

Shepard, F.P. and Inman, D.L. (1951). Nearshore circulation. In *Proc. 1st Coastal Engineering Conference*, 50-59.

Shepard, F.P., Emery, K.O., and LaFond, E. (1941). Rip currents: a process of geological importance. *Journal of Geology*, **49**, 337-369.

Short, A.D. (1985). Rip-current type, spacing and persistence, Narrabeen Beach, Australia. *Journal of Marine Geology*, **65**, 47-71.

Short, A.D. and Brander, R.W. (1999). Regional variations in rip density. *Journal of Coastal Research*, **15**(3), 813-822.

Smith, J.A. and Largier, J.L. (1995). Observations of nearshore circulations: Rip currents. *Journal of Geophysical Research*, **100**(C6), 10967-10975.

Sonu, C.J. (1972). Field observations of nearshore circulation and meandering currents. *Journal of Geophysical Research*, **77**, 3232-3247.

Sørensen, O.R., Schäffer, H.A. and Madsen, P.A. (1998). Surf zone dynamics simulated by a Boussinesq type model. Part III. Wave-induced horizontal nearshore circulation. *Coastal Engineering*, **33**, 155-176.

Symonds, G., Homan, R.A., and Bruno, B. (1997). Rip currents. In *Proc. Coastal Dynamics '97*, 584-593.

Thomas, D.A. (2003). Laboratory rip current circulation using video-tracked Lagrangian drifters (M.S. Dissertation). Univ. of Florida

Uemura, T., Yamamoto, F., and Ohmi, K. (1989). A high speed algorithm of image analysis for real time measurement of two-dimensional velocity distribution. In *Flow Visualization*, ed. B. Khalighi, M. Braun, C. Freitas, FED-85: 129-134. New York: ASME. 149 pp.

Vagle, S., Farmer, D.M., and Deane, G.B. (2001). Bubble transport in rip currents. *Journal of Geophysical Research*, **106**(C6), 11677-11689.

Van Dyke, M. (1982). An album of fluid motion. Stanford, Calif: Parabolic Press. 176 pp.

Vos, R.G. (1976). Observation on the formation and location of transient rip currents. *Sediment Geology*, **16**, 15-19.

Wind, H.G. and Vreugdenhil, C.B. (1986). Rip-current generation near structures. *Journal of Fluid Mechanics*, **171**, 459-476.

Willert, C.E. and Gharib, M. (1991). Digital particle image velocimety. *Experiments in Fluids*, **10**(4), 181-193.

Yu, J. and Slinn, D.N. (2003). Effects of wave-current interaction on rip currents. *Journal of Geophysical Research*, **108**(C3).